A Study of Neutral Kaons and Charged Particles in Photoproduced Jets at HERA

Allan Stephen Wilson

Department of Physics and Astronomy
The University of Glasgow
Glasgow, Scotland

Thesis submitted for the degree of Doctor of Philosophy

11th June 1997

Abstract

Multiplicities for K^0 and charged particles in hard photoproduction events with $0.2 \leq y \leq 0.85$, containing a jet with $E_T^{JET} \geq 8$ GeV and $|\eta| \leq 0.5$, have been measured at HERA using the ZEUS detector. The K^0 and charged particle multiplicities as a function of transverse momentum are generally well described by the PYTHIA Monte Carlo with default hadronisation parameters, however, PYTHIA underestimates the K^0 and charged particle multiplicities at large pseudorapidity.

The mean K^0 and charged particle multiplicities per jet are measured as, $< n_{K^0/JET} > = 0.40 \pm 0.01 \,^{+0.03}_{-0.02}$, and $< n_{h^\pm/JET} > = 3.11 \pm 0.06 \,^{+0.11}_{-0.10}$. The PYTHIA generator with default hadronisation parameters predicts $< n_{K^0/JET} > = 0.52 \pm 0.01$, and $< n_{h^\pm/JET} > = 3.32 \pm 0.04$. Jet profiles show that PYTHIA predicts narrower jets than is observed in the data, and that the particle multiplicity excess is located in the jet cores. The mean K^0 and charged particle multiplicities per jet predicted by PYTHIA with a lower strangeness suppression factor, and PYTHIA with multiple interactions are also in excess of the data.

The K^0 and charged particle fragmentation functions are compared with PYTHIA and the results of a leading and next-to-leading order calculation. Despite the excess in particle multiplicities PYTHIA describes both K^0 and charged particle fragmentation functions well. The leading and next-to-leading order calculation describes the K^0 and charged particle fragmentation functions well.

Preface

Since the ZEUS and H1 detectors came online in 1992 much work has been carried out in the field of high energy photoproduction. Direct photoproduction events, where the photon interacts as a fundamental particle, and resolved photoproduction events, where the photon acts as a source of partons which interact with the proton, have been observed. Measurements of high transverse energy jet cross sections in photoproduction interactions have tested perturbative QCD and Monte Carlo predictions, increasing our understanding of photoproduction interactions and the structure of the resolved photon. However, a fuller understanding of photon structure and photoproduction events will inevitably require the study of many further aspects. This thesis presents the first measurements of single particle distributions in hard photoproduction events and aims to test their description by the PYTHIA Monte Carlo, and QCD calculations.

In comparison to high transverse energy jet production, the process of particle production is less well understood. This is due to the 'running' of the strong interaction coupling strength, α_s, preventing perturbative QCD calculations at the low energy scales associated with particle production. Phenomenological approaches are used instead to describe the relative production rates of different particle species. Single particle fragmentation functions enable, for example, the momenta and pseudorapidity spectra of a given species of particle to be calculated, given the cross sections for all parton level processes contributing to an interaction, and ignoring all other particles in an event. Fragmentation functions have been measured at e^+ e^- experiments taking advantage of the clean environment and well defined centre-of-momentum energy. Taking into account

differences between the fragmentation functions of different parton flavours, hadron production is however expected to be process independent. Therefore, fragmentation functions determined from $e^+ e^-$ data should not only be applicable to calculations of particle cross sections in photoproduction events, but when measured in photoproduction events should be consistent with the $e^+ e^-$ measurements. One aim of this thesis is to compare fragmentation functions calculated from $e^+ e^-$ data to fragmentation functions measured in hard photoproduction events at ZEUS. This provides a limited test of the universality of fragmentation since the flavour of the scattered partons is unknown. An alternative to the single particle fragmentation function method of parametrising hadronisation is provided by Monte Carlo techniques. Monte Carlos can provide more detailed simulation than single particle fragmentation functions. In addition, they are used in this thesis to compare the measured fragmentation function to the prediction averaged over all parton flavours.

Chapter 1 begins with a review of the current knowledge of fundamental particles and their interactions, the historical development of this understanding, with emphasis on the physics of the strong interaction and QCD. As an introduction to the physics at HERA, an account of proton structure measurements by deep inelastic lepton-proton scattering and the explanation of proton structure measurements by QCD is given. The chapter concludes with a description of photoproduction processes at HERA, and a review of photon structure models.

The methods used to describe perturbative and non-perturbative aspects of strong interactions in high energy physics are discussed in Chapter 2. The use of single particle fragmentation functions to describe the non-perturbative phase of hadron production is outlined. A summary of a calculation of fragmentation functions for charged particles and neutral kaons by Binnewies et al. [1, 2] is given. The simulation of hard photoproduction events in Monte Carlos is then discussed, in particular, the simulation of perturbative QCD interactions by PYTHIA, and the non-perturbative hadronisation phase by JETSET.

The components of the ZEUS detector are described in chapter 3, concentrat-

ing on the components relevant to this thesis. Work carried out by the author on a global CTD calibration method is reported in chapter 4, which is incidental to the main thrust of the thesis.

The methods and criteria for selection of hard photoproduction events are discussed in chapter 5. The online trigger criteria used during the 1994 data taking period, and the offline cuts developed by the author, are described. The selected events are shown to constitute a highly pure sample of hard photoproduction events.

The analysis of kaons in hard photodoproduction events carried out by the author is presented in chapter 6. The K_s^0 finder developed by the author is described and shown to provide accurate K_s^0 reconstruction. The inclusive neutral kaon multiplicities, $\frac{1}{N_{JETS}}\frac{dN(K^0)}{dp_T^2}$ and $\frac{1}{N_{JETS}}\frac{dN(K^0)}{d\eta}$ in hard photoproduction events are presented. To study the production of kaons more closely related with the outgoing partons from the hard interaction, the mean K^0 multiplicity per jet, and K^0 fragmentation function were measured. A similar analysis of charged particles by the author is presented in chapter 7.

Acknowledgments

I would first of all like to thank David Saxon for giving me the opportunity to join the Glasgow University PPE group and the ZEUS Collaboration. This PhD was funded by The Particle Physics and Astronomy Research Council to whom I am grateful.

I would like to thank my supervisor, Peter Bussey, for the advice and encouragement he has given me during my research and for proof-reading this thesis. Several other past and present members of ZEUS Glasgow have provided me with advice on my work, thesis and computers, all of which has proved useful. Thank you Tony, Nick, Ivor and Laurel. I am sincerely grateful to Catherine MacIntyre for her support with all my travel arrangements and claims, and David Martin, Alan Flavell and Mary Shearer for providing the UNIX cluster maintenance and support.

Many people in the ZEUS Collaboration have provided assistance, advice and encouragement throughout my research, but, I am most grateful to Juan Pablo Fernandez for collaborating with me on this project, and bringing it to a fruitful conclusion. Someday we'll get together and talk about something other than Kaons !

The advice from members of the ZEUS High Et and Jets Working Group has been extremely helpful and I would especially like to thank Costas Foudas, Jon Butterworth, Jutta Hartmann and Luis Labarga, for their support and advice, Mohsen Khakzad for his help in processing my Monte Carlo events, and Rob Saunders and Lutz Feld for the PYTHIA MI events. Greg Field, Yuji Yamazaki, Juan Terron and Claudia Glasman also provided me with advice and answered

my questions, no matter how stupid they were. John Lane, Norman Mccubbin, Ken Long and Julian Shulman from ZEUS UK all gave me useful advice during my work on the CTD. There are so many cogs to the ZEUS machine that I probably still don't appreciate just how much other people have contributed to my thesis. To all those that I haven't mentioned, but who toiled on my behalf, on the trigger, detector simulation, ZARAH, anything, thank you.

I am grateful to Janko Binnewies, who made his fragmentation function calculations available to me in an extremely easy-to-use form and provided clear answers to my questions.

My time at Glasgow would not have been the same without my colleagues. To those ZEUS students with whom I shared an office, Martin, Val, Jane and Esther, I hope you enjoyed my company as much as I did yours. Being on other experiments, Stephen Gowdy, Stephen Thorn, Fiona, Simon, Richard, Lee, Evelyn and Matt must have all felt safe from the excesses of my company. Not so. Luckily for those on ALEPH, there'll no more 'elevator' music in room 456. I cannot fail to mention Stan, as all my knowledge of the world outside of my PhD has been gleaned from reading his copies of 'The Guardian'.

My time in Hamburg would not have been the same had it not been for my friends there. I would like to thank them all, unfortunately most of my memories of the time I spent with them are a bit on the hazy side, so I'm not exactly sure what I'm thanking them for. Anyway to my friends Paul Sutton, L'il' Dave(Wwaarrgh, Kaons, man. Kaons) Milstead, John Lomas, Pete Bispham and Mark Burton, thanks for the discussion on voter inertia, to Phil Kaziewicz thanks for the videos, whisky and late night chat, especially as you couldn't handle it, and thanks to Dave Kant, Paul Newman, Andy Mehta, and all those at Bleicherstrasse for putting me up on occasions.

I've remained sane throughout my thesis by playing in The Kirkintilloch Band. I'd like to thank Peter Fraser and Les Wood for still allowing me to play Repiano cornet even after not practising for months on end.

Finally, I'd like to thank Mum, Dad, Susan and Fraser, for the love, support

and encouragement throughout all of my education. I dedicate this thesis to them.

Contents

List of Figures

List of Tables

Chapter 1

Theoretical Background

Listen, buddy, if I could tell you in a minute what I did, it wouldn't be worth the Nobel Prize.

R. P. Feynman

1.1 Fundamental Particles and Interactions

Our current understanding of the universe is that matter is made from two classes of fundamental fermions, quarks and leptons, which interact via the exchange of bosons. The known quarks, leptons and bosons are listed in table 1.1

Within the group or 'family' of 6 quarks there are three 'generations'. Each generation contains two types or 'flavours' of quarks; one quark of charge $\frac{2}{3}$ and

Charge	Quarks		
$-\frac{1}{3}$	d	s	b
$\frac{2}{3}$	u	c	t
	Leptons		
-1	e^-	μ^-	τ^-
0	ν_e	ν_μ	ν_τ

Interaction	Boson	Mass(GeV)	Charge
Weak	Z^0, $W^\pm$	91, 80.2	0,$\pm$ 1
Strong	g	0	0
Electromagnetism	γ	0	0

Table 1.1: The known quarks, leptons and bosons.

one of charge $-\frac{1}{3}$ in units of the proton charge. The main difference between each family is mass ranging from, ~ 5 MeV for u and d, ~ 200 MeV and ~ 1.3 GeV for s and c, to ~ 4.5 and 169 GeV for b and t. Unlike the quarks, leptons are either neutral or have charge -1. However, a similar structure is observed in the lepton family, where there are also three known generations apparently identical except for mass, though it is currently unclear whether the ν's are massless. The reason why quarks and leptons are distinct will be clarified in the following sections.

There are 4 forces by which particles interact. Most obvious to humans is gravitation. However, in particle physics gravitation is negligible since its 'coupling' strength is extremely weak. The reason it appears so manifest is that mass is cumulative and there does not appear to be antimass. Gravitation is hypothesised to be transmitted by exchange of massless gravitons. This leads to an inverse square law form for the gravitational force between two massive objects, enabling gravity to act over large distances.

The next weakest force is known as the weak force. It is responsible for flavour changing processes, such as nuclear β decay and radioactivity. The strength of the weak force is apparently small because it is mediated by massive vector bosons, Z^0 and $W^{\pm}$. According to the Uncertainty Principle, the interval of time in which a weak interaction can occur is inversely proportional to the amount of energy required to form the Z^0 or $W^{\pm}$. The weak force therefore has a range of only a few fermi for Z^0 and $W^{\pm}$ which have masses of 91 and 80.2 GeV respectively.

The second strongest force is electromagnetism. Probably the most important property of electromagnetism is that it binds electrons in atoms and is thus responsible for the whole of chemistry. Since electromagnetism is mediated by massless photons it has an inverse square law dependence on distance and is therefore a long range force like gravity. However, electric charge can be either positive or negative. It is therefore possible to combine equal amounts of positive and negative charges on an object, rendering it electrically neutral, so that it does not interact electromagnetically.

Electromagnetic interactions were the first to be understood in terms of a

quantum theory, known as Quantum Electrodynamics (QED). Dirac's relativistic quantum theory predicted the existence of antiparticles and particles with intrinsic angular momentum, $S = \frac{1}{2}\hbar$, where $\hbar = \frac{h}{2\pi}$, and h is Planck's constant. The antiparticles of electrons, positrons, and the spin $\frac{1}{2}$ nature of electrons were both experimentally confirmed. The Dirac theory did not however explain how interactions between electrons and positrons arose. Interactions between electrons arise in QED because it is a gauge theory. Conservation of energy and charge require that physics is unchanged if the electromagnetic potentials are changed by a constant. This is reflected in quantum theory where the phase of a wavefunction is not observable and can also be changed by a constant. QED becomes an interacting theory of electrons and photons when the electron wavefunctions are subjected to local phase transformations. This requires the addition of extra terms to the QED Lagrangian corresponding to a field with which electrons and positrons interact. The field is massless and thus represents photons. The strength of electromagnetism is quantified by the fine structure constant, $\alpha_{em} \sim \frac{1}{137}$. The small value of α_{em} means QED calculations can be approximated by a series of ever more complex interactions using perturbation theory.

Finally, the strong force, as its name suggests, is the strongest. The strong force is responsible for binding protons and neutrons in atomic nuclei, overcoming the force of electromagnetic repulsion that protons exert on each other. It is an interaction between 'colour' (and/or anticolour) charges, of which there are three types, red, green and blue (antired, antigreen and antiblue). The strong force is propagated by electrically neutral, massless gluons, which carry colour. The fact that gluons carry colour means gluons couple directly with each other, unlike photons in QED. This leads to an important difference between the large distance behaviour of the strong and electromagnetic interactions as will be discussed in section 1.3. Quarks and leptons form distinct families because quarks carry colour but leptons do not. Leptons therefore do not interact via the strong force. Strong interactions are described by the quantum field theory, Quantum

Chromodynamics (QCD), which is now discussed.

1.2 Origin of Quantum Chromodynamics

The concepts of quarks and colour, and thus QCD, arose from the study of baryon and meson spectroscopy [3]. In 1961 Gell-Mann and Ne'eman independently suggested a model to explain hadron spectroscopy known as the eightfold way. They observed that classifying the known mesons and baryons according to their angular momentum gave groups of eight particles which showed a similar structure when plotted in terms of isospin and strangeness. Following the discoveries of the Σ^* and Ξ^* particles in 1963, Gell-Mann and Ne'eman used this model to predict that the Δ, Σ^* and Ξ^* particles belonged to a group of ten particles which contained an as yet undiscovered particle, the Ω^-. The Ω^- was discovered in 1964.

The success of the eightfold way led Gell-Mann and Zweig to explain hadron spectroscopy with the $SU(3)_{flavour}$ model. They postulated that hadrons were composed of three types of spin 1/2 particles called quarks possessing flavour quantum numbers, up(u), down(d) and strangeness(s). $SU(3)_{flavour}$ assumed that baryons were formed from three particles, and mesons from quark-antiquark pairs. While this model succesfully accounted for the meson and baryon spectra, there were several problems.

In terms of the quark model the Ω^- was a composite sss state which belonged to the lightest baryon states with $J = \frac{3}{2}$. It therefore had an $L = 0$, $S = \frac{3}{2}$ spatially and spin symmetric wavefunction. Also contained in this group of $J = \frac{3}{2}$ baryons were the Δ^{++} and Δ^-, composite uuu and ddd states respectively. The Δ^{++}, Δ^- and Ω^- are fermionic states which, according to the Exclusion Principle (EP), should have antisymmetric wavefunctions under spatial, spin and flavour rotations. The $SU(3)_{flavour}$ description of the Δ^{++}, Δ^- and Ω^- therefore violated the EP. A new degree of freedom in hadronic wavefunctions was proposed to preserve the EP; this was called colour.

However, postulating the existence of quarks and colour led to the problem that neither quarks nor colour had been observed. To explain the non-observation of colour, it was proposed that hadrons could only be formed in neutral colour states; baryons were composed of three different coloured quarks and mesons from a coloured quark and its anticoloured antiquark. This explained why baryon and meson states consisted of three quarks or a quark and an antiquark, an assumption of the $SU(3)_{flavour}$ model. Colour was then proposed to be the charge of the strong interaction, and as discussed in section 1.3 was shown to confine quarks within hadrons, thus preventing free quarks and colour from being observed. In this way, the quark description of hadron spectroscopy changed from $SU(3)_{flavour}$ to $SU(3)_{colour}$.

Though quarks and colour have not been observed directly, their existence as real physical phenomena has support from many experiments. The number of colours has been determined to be 3 from measurements of the total e^+e^- annihilation cross section at high energies, consistent with QCD. The existence of quarks as hadronic constituents is supported by lepton-nucleon scattering experiments as discussed in section 1.4.

1.3 Running Coupling Strengths

The discussion of coupling strengths in section 1.1 was somewhat oversimplified since the coupling strength of each force is in fact not constant, but depends on the energy scale of an interaction, or equivalently, the distance scale at which particles interact. Coupling constants are said to 'run' with energy.

The energy dependence of coupling constants is different in QED and QCD. In each force an electrical or colour charge is surrounded by virtual particles. Polarisation of the virtual particles occurs so that the electrical or colour charge observed depends on the distance scale at which a particle is probed. In QED a charge attracts opposite charges so that the surrounding virtual particles screen the 'bare' charge. The observed charge of a particle is therefore lower at

large distances than at small distances. By the Uncertainty Principle a particle scattered or probed at a large energy scale is observed to have a larger electrical charge than at a lower energy scale. The electromagnetic coupling strength is very small at low energies, $\alpha_{em} = \frac{1}{137}$. This allows the use of perturbation theory in QED calculations. By taking into account higher order terms in calculations of electromagnetic interactions, QED predicts α_{em} increases with energy scale Q according to

$$\alpha_{em}(Q^2) = \frac{\alpha_{em}(\mu^2)}{1 - (\frac{\alpha_{em}(\mu^2)}{3\pi}) \ln (Q^2/\mu^2)} \tag{1.1}$$

where $\alpha_{em}(\mu^2)$ is the value of α_{em} at a reference energy scale, μ. If QED calculations are performed to all orders then their result is actually independent of μ.

In QCD the strong coupling strength decreases with energy. This effect occurs because gluons can interact with gluons, which introduces an extra term into the QCD analogue of equation 1.1.

$$\alpha_s(Q^2) = \frac{\alpha_s(\mu^2)}{1 + \frac{\alpha_s(\mu^2)}{12\pi}(33 - 2N_f) \ln (Q^2/\mu^2)} \tag{1.2}$$

where N_f is the number of quark flavours. So the strong coupling strength, α_s, decreases as the energy scale of an interaction increases provided that $N_f < 17$.

The running of α_s is important for several reasons. The large value of α_s at low energies explains why free quarks and gluons are not observed. By the Uncertainty Principle equation 1.2 could be rewritten in terms of the distance scale at which the colour charge of a particle is measured; α_s would then have a large value at 'large' distance scales, $\sim$ 1 fm. This can be expressed in terms of the potential energy of the colour field between two coloured objects.

$$V(r) = -\frac{4}{3}\frac{\alpha_s}{r} + \kappa r \tag{1.3}$$

where α_s is the high energy limit of equation 1.2, r denotes the interquark or gluon separation and κ is a constant defining the energy density of the QCD field. The first term is analogous to the electromagnetic potential and arises from the fact that gluons are massless. The second term represents the effect of gluon-gluon

self interactions. As the interquark separation increases, more and more energy is contained in the colour field until it becomes energetically more favourable for the colour field to break, converting some of the stored field energy into the mass of a quark antiquark pair. In this way, quarks produced in high energy particle physics experiments are not observed as isolated free particles, and colour is also not observed. Instead quarks are confined within hadrons by their colour charge.

The running of α_s also enables theorists to perform calculations using perturbation theory. Perturbative QCD (pQCD) calculations are accurate for interactions at an energy scale above $\sim \mathcal{O}(1\text{ GeV})$. This has led to a fuller understanding of hadron structure beyond the simple $SU(3)_{colour}$ model.

1.4 Lepton Nucleon Scattering

A schematic diagram of deep inelastic e^+p scattering (DIS) is shown in figure 1.1. In the quark-parton model (QPM), the e^+ interacts with a charged parton in the proton via exchange of a γ, Z^0 or $W^\pm$. When the first measurements of proton structure were made it was not known if the proton constituents were the quarks and gluons of QCD, and the term parton was used to reflect this ignorance. The partons were assumed to be free and non-interacting within the proton. This assumption was based on the fact that the rate of interactions between partons would be slowed down because of time dilation when the proton was 'viewed' from a frame where it had extremely high energy. The time scale of the hard scattering interaction is then much shorter than the time between parton interactions, allowing partons to be treated as free.

1.4.1 Kinematics

If $k = (E_e, 0, 0, -E_e)$ and $P = (E_p, 0, 0, E_p)$ are the initial e^+ and p 4-momenta, q the photon 4-momentum, $k' = (E'_e, 0, E'_e \sin\theta_e, E'_e \cos\theta_e)$ the scattered e^+ 4-momentum, then the interaction can be described by the Lorentz invariants,

$$Q^2 = -(k - k')^2 = 2E_e E'_e(1 + \cos\theta_e) \tag{1.4}$$

$$x = \frac{Q^2}{2P.q} = \frac{E_e}{E_p}\frac{E'_e(1+\cos\theta_e)}{2E_e - E'_e(1-\cos\theta_e)} \tag{1.5}$$

$$y = \frac{P.q}{P.k} = 1 - \frac{E'_e}{2E_e}(1-\cos\theta_e)) \tag{1.6}$$

$$s = (k+P)^2 = 4E_eE_p \tag{1.7}$$

$$W^2 = (q+P)^2 = Q^2\frac{(1-x)}{x} \tag{1.8}$$

where all mass terms have been neglected. Q^2 is the mass of the virtual photon interacting with the parton in the proton and x is the momentum fraction of the proton carried by the struck parton. In the proton rest frame, y is the energy fraction of the e^+ transmitted to the virtual photon. In the hadronic centre-of-momentum frame, where $E'_e = E_e$ and the e^+ is scattered through an angle θ^*, $y = \frac{1}{2}(1-\cos\theta^*)$. s and W are the e^+p and γp centre-of-momentum energies respectively. Only two variables from Q^2, x and y need to be measured to specify the scattering completely since $Q^2 = xys$.

Expressions for Q^2, x and y need not be written in terms of the scattered e^+ energy and angle. For example, in the Jacquet-Blondel method [4], y is calculated as,

$$y_{JB} = \frac{\sum_i E_i(1-\cos\theta_i)}{2E_e} \tag{1.9}$$

where the sum runs over all final state hadrons. To distinguish between using the scattered e^+ variables and the Jacquet-Blondel method, y_e will be used to denote y calculated from the scattered e^+ variables, and y_{JB} will be used to denote y calculated using the Jacquet-Blondel method.

1.4.2 The Quark Parton Model

In the QPM the cross-section for e^+p scattering is calculated from the sum of e^+q scattering matrix elements for each quark flavour, weighted by the parton distribution function of the respective quark flavour in the proton

$$\frac{d\sigma}{dxdQ^2}(ep \to eX) = \sum_i f_i(x)\frac{d\sigma_i}{dxdQ^2}(eq_i \to eq_i) \tag{1.10}$$

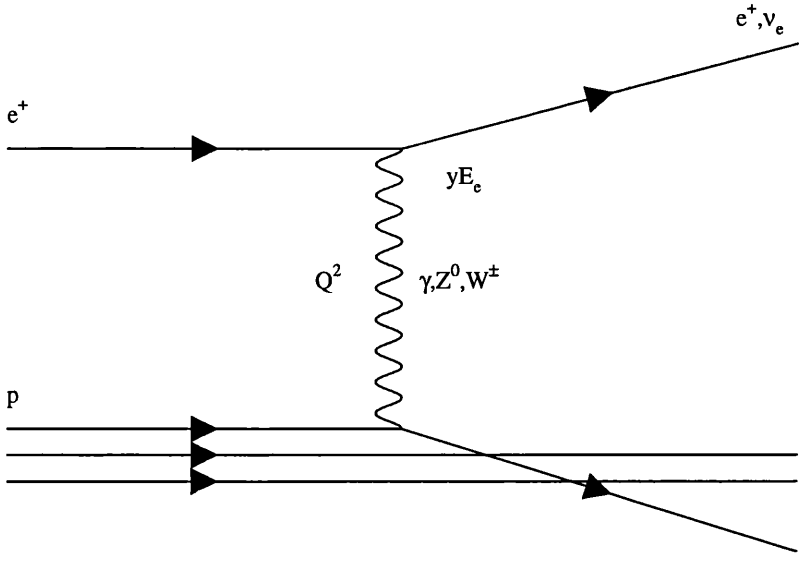

Figure 1.1: Feynman diagram of leading order deep inelastic scattering process

The factorisation of the ep cross sections into two terms is possible because of the difference in time scale between the hard scatter and interactions between the proton's constituents, as remarked earlier. The parton distribution function, $f_i(x)$, is defined such that $f_i(x)dx$ is the probablility of a parton of flavour i having momentum fraction of the proton between $x, x + dx$.

The above cross section can be rewritten as

$$\frac{d\sigma}{dxdQ^2}(ep \to eX) = \frac{4\pi\alpha_{em}^2}{xQ^4}(y^2 x F_1^p(x) + (1-y)F_2^p(x)) \tag{1.11}$$

where $F_1^p(x)$, $F_2^p(x)$ are dimensionless structure functions. The contribution from Z^0 exchange is neglected in equation 1.11 as it only affects the cross section at large Q^2.

According to QCD the charged partonic consituents of the proton are quarks. The spin 1/2 property of quarks then leads to the predictions,

$$F_2^p(x) = x\sum_i e_i^2 f_i(x) \tag{1.12}$$

where e_i denotes the charge on a quark of flavour i in units of the proton charge,

and,

$$F_2^p(x) = 2xF_1^p(x) \tag{1.13}$$

The relationship in equation 1.13 is known as the Callan-Gross relation and was confirmed experimentally [5], suggesting that the charged partons in the proton are indeed quarks. Using equation 1.13, equation 1.11 can be rewritten as

$$\frac{d\sigma}{dxdQ^2}(ep \to eX) = \frac{4\pi\alpha^2}{xQ^4}(\frac{y^2}{2} + (1-y))F_2^p(x) \tag{1.14}$$

Further evidence that the proton contains quarks, and that the quarks had fractional charges $2/3$ and $-1/3$, came from measurements of F_2 in νp and νn scattering, where it was observed that $F_2^{ep+en} = \frac{5}{18}F_2^{\nu p+\nu n}$, in agreement with prediction.

1.4.3 QCD Corrections to the QPM

The assumptions of the QPM led to several predictions. The first was that at very large Q^2, F_2 depends only on x, i.e. it does not depend on the Q^2 of the scattering. This is known as scale invariance. Although initially observed at SLAC [6], subsequent analysis [7] showed a logarithmic dependence of proton structure on Q^2; thus $F_2^p = F_2^p(x, Q^2)$. Logarithmic dependence of F_2^p on Q^2 at a fixed value of x arises in pQCD. Quarks within the proton can radiate gluons and similarly gluons radiate quarks. As Q^2 increases the spatial resolution of the probing photon improves so that separate quarks and gluons can be resolved. Therefore, as Q^2 increases more and more quark-gluon branchings are resolved. This has the effect of increasing(decreasing) F_2^p at low(high) x as Q^2 increases.

The dependence of $F_2^p(x, Q^2)$ on Q^2 in pQCD is calculated using the GLAP equations [8],

$$\frac{df_i(x,Q^2)}{d\log Q^2} = \frac{\alpha_s}{2\pi}\int_x^1 \frac{d\xi}{\xi}(f_i(\xi,Q^2)P_{qq}(\frac{x}{\xi}) + g(\xi,Q^2)P_{gq}(\frac{x}{\xi})) \tag{1.15}$$

$$\frac{dg(x,Q^2)}{d\log Q^2} = \frac{\alpha_s}{2\pi}\int_x^1 \frac{d\xi}{\xi}(f_i(\xi,Q^2)P_{qg}(\frac{x}{\xi}) + g(\xi,Q^2)P_{gg}(\frac{x}{\xi})) \tag{1.16}$$

The 'splitting' functions $P_{qq}(z)$, $P_{qg}(z)$, $P_{gq}(z)$ and $P_{gg}(z)$ give the probability that a quark or gluon will emit another quark or gluon carrying a momentum

fraction z of its parent. The observed dependence of $F_2^p(x,Q^2)$ on Q^2 in [7] was consistent with pQCD, which suggested the protons contain gluons as well as quarks.

The QPM assumption that the proton is entirely composed of charged particles leads to the momentum sum rule,

$$\sum_i \int_0^1 x f_i(x,Q^2) dx = 1 \tag{1.17}$$

Measurements show that approximately half the proton's momentum is carried by charged constituents, providing further evidence for a gluon contribution to proton structure.

1.4.4 Parametrisations of Proton Structure

Proton structure functions are parametrised by fitting physically motivated gluon and quark momentum distributions to several sets of lepton- nucleon and hadron-hadron collider data. The general approach is to choose the input parton distributions at a high enough initial energy scale Q_0^2 so that pQCD can be applied. It is usual to separate the quark distribution functions into valence and sea components, so that the total u quark distribution at the input scale is given by their sum, $u(x,Q_0^2) = u_v(x,Q_0^2) + u_s(x,Q_0^2)$, with a corresponding expression for d quarks. Sea quarks arise from $g \rightarrow q\bar{q}$ splitting, so the total sea distribution can be written as

$$\begin{aligned} S(x,Q_0^2) &= u_s(x,Q_0^2) + \bar{u}_s(x,Q_0^2) + d_s(x,Q_0^2) + \bar{d}_s(x,Q_0^2) + \\ &\quad s_s(x,Q_0^2) + \bar{s}_s(x,Q_0^2) \qquad (1.18) \\ &= 2(\bar{u}(x,Q_0^2) + \bar{d}(x,Q_0^2) + \bar{s}(x,Q_0^2)) \qquad (1.19) \end{aligned}$$

where only 3 flavours have been considered. The relative contributions of different flavour quarks to $S(x)$ is dependent on the assumed values of quark masses. The parton distributions are then evolved using the GLAP equations and fitted to the data sets. Scaling violations and sum rules constrain the normalisations of the gluon distribution of each quark flavour component.

Before HERA, F_2 was well determined above $x \sim 0.01$, and there was much speculation on the behaviour of F_2 at low x. Physically motivated gluon distributions were used to determine parametrisations for F_2 which gave $F_2 \sim x^0$ and $x^{-0.5}$ [9]. Measurements at HERA [10] have shown $F_2 \sim x^{-0.3}$ at low x and $Q^2 \sim 10$ GeV^2. Other important recent results include measurements of the Drell-Yan asymmetry in proton-proton and proton-deuteron reactions by NA51 [11] and the charged lepton asymmetry from W^+W^- Drell-Yan production in $p\bar{p}$ collisions at CDF [12]. Both these measurements show that in the sea, $\bar{u} - \bar{d} < 0$. These features are incorporated in the MRSA [13] parton distribution functions used for the generation of Monte Carlo events in this analysis.

1.5 Photoproduction Processes

From the $1/Q^4$ dependence of the cross section in equation 1.14 it is apparent that low Q^2 e^+p scattering events occur at the highest rate. These reactions involve photons whose properties appear very similar to those of real photons, and are referred to generically as 'photoproduction'. At leading order the photon either reacts as a whole with a parton in the proton, which is known as direct photoproduction, or it may act as a source of partons which subsequently interact with the proton. The latter process is known as resolved photoproduction, and in this class of processes HERA acts as a hadron-hadron collider rather than an e^+p collider.

In the resolved process the photon fluctuates into a $q\bar{q}$ pair. The quark-antiquark pair then interact giving the photon some partonic structure. The resolved process can be further broken down into contributions depending on the transverse momentum, k_T, of the $\gamma \rightarrow q\bar{q}$ splitting. If the k_T is small the resolved photon's partonic structure and interactions are modelled as a vector meson's with the same quantum numbers as the photon, $J^{PC} = 1^{--}$, e.g. ρ, ω or ϕ. This is known as the vector meson dominance model (VMD). When the $\gamma \rightarrow q\bar{q}$ splitting has a large k_T the process is known as anomalous photoproduction.

In this scenario the parton structure of the photon can be calculated within the framework of pQCD [14]. The value of k_T at which the resolved process is separated into the VMD and anomalous contributions is of course arbitrary, as the above description is a simplification of physics expected to exhibit a continuous transition in the k_T of the $\gamma \rightarrow q\bar{q}$ splitting.

Examples of leading order Feynman diagrams for direct and resolved hard photoproduction are shown in figures 1.2(a) and 1.2(b) respectively. The classification of figure 1.2(c) as direct or resolved is ambiguous as it depends on the momentum transfer with which the gluon is emitted from the propagator.

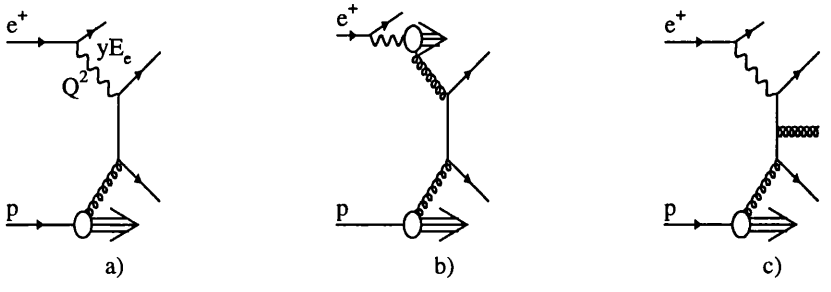

Figure 1.2: Feynman diagrams of leading order direct (a) leading order resolved (b) and next-to-leading order (c) photoproduction processes.

Analogously to x in DIS, a quantity x_γ, representing the momentum fraction of the photon entering the hard interaction can be defined.

$$x_\gamma = \frac{s'}{W} \tag{1.20}$$

where s' is the centre-of-momentum energy of the hard interaction between the photon or parton in the photon and the parton in the proton. Thus, at leading order, $x_\gamma = 1$ in direct events, while for resolved events $x_\gamma < 1$.

Photoproduction events can be classified according to the momentum transfer of the scattering process. The events studied in this thesis are defined as 'hard'

photoproduction, meaning there is a large momentum transfer scattering between the photon or parton in the photon and parton in the proton. The outgoing partons are observed as high transverse energy jets. In hard photoproduction events the momentum fraction of the photon, x_γ, entering the interaction can then be estimated from

$$x_\gamma^{OBS} = \frac{\sum_i E_i(1-\cos\theta_i)}{2yE_e} = \frac{\sum_i E_{T_i} e^{-\eta_i}}{2yE_e} \tag{1.21}$$

where the sum is over particles within the two highest transverse energy jets and E_{T_i} and η_i are the transverse energy and pseudorapidity of particles within the jets. If all interactions proceeded at leading order and there were no hadronisation effects then $x_\gamma^{OBS} = x_\gamma$. This is not the case, but the definition of x_γ^{OBS} enables experiment and theory to be meaningfully compared even though x_γ^{OBS} and x_γ are no longer identical. Similarly,

$$x_p^{OBS} = \frac{\sum_i E_i(1+\cos\theta_i)}{2E_p} = \frac{\sum_i E_{T_i} e^{\eta_i}}{2E_p} \tag{1.22}$$

gives an estimation of the momentum fraction of the proton carried by its interacting parton.

Some important distinctions exist between direct and resolved event topologies. In direct events the final state is characterised by two outgoing partons and a p remnant. In resolved events there is also a γ remnant produced close to the incident photon direction. Since the hard subprocess in direct photoproduction events generally has a larger centre-of-momentum energy than resolved events the jet E_T spectrum is harder in direct than in resolved photoproduction events. Similarly, the jet η spectrum is peaked towards the photon direction in direct events, whereas resolved events have a jet η spectrum peaked in the proton direction.

1.6 Photon Structure

Much of the formalism used to describe proton structure can be applied to describe photon structure. Just as proton structure has been measured in DIS e^+p

scattering experiments, photon structure has been measured in DIS $e\gamma$ scattering.

This process occurs at e^+e^- colliders as depicted in figure 1.3. The e^+ emits a low Q^2 photon which is then probed by a higher Q^2 photon emitted by the e^-. The scattered e^- is observed in the detector while the e^+ carries on down the beampipe. Of course, the rôle of the e^+ and e^- are interchangeable in this process.

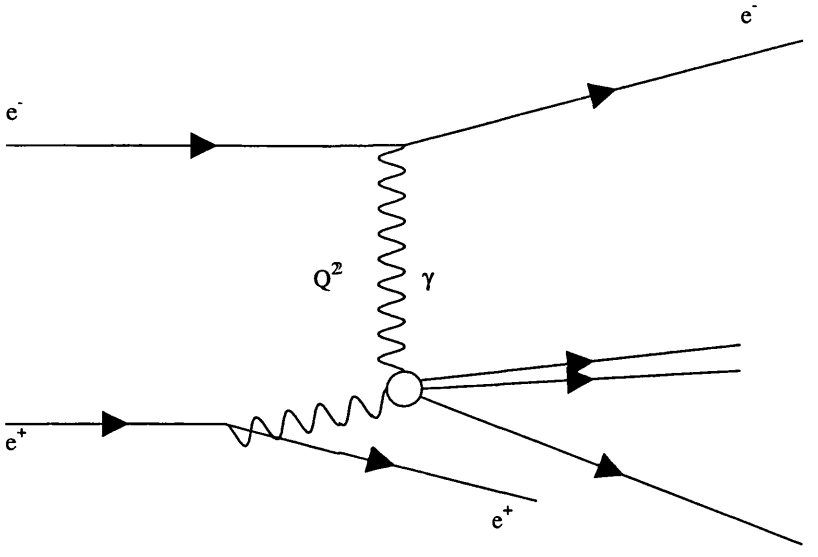

Figure 1.3: Schematic diagram of a deep inelastic $e\gamma$ scattering process.

Analogously to DIS e^+p scattering, the cross section for this process can be thought of as depending on quark densities within the photon parametrised by a function F_2^γ. Several effects make the determination of F_2^γ more demanding than

F_2^p in e^+p scattering.

Firstly, an additional $\mathcal{O}(\alpha_{em})$ appears in the $e\gamma$ scattering cross section, because the probed photon has to be emitted. The magnitude of F_2^γ is also $\mathcal{O}(\alpha_{em})$ [14]. The cross section for $e\gamma$ scattering is therefore $\mathcal{O}(\alpha_{em}^4)$ two orders of magnitude down on e^+p scattering. This must be compensated for by higher e^+e^- luminosity.

Secondly, the probed photons are not monoenergetic. Their energy spectrum has been approximated by Weizsäcker-Williams [15]. The photon energy is not usually measured as the low angle scattered $e^\pm$ is not detected, so the fraction of the photon energy entering the interaction is determined only from the mass of the hadronic state, as in equation 1.8. Finite angular coverage of detectors means that some of the hadronic final state is not completely measured. Monte Carlo models are used to correct for the missing hadrons, however this leads to differences in F_2^γ at low x depending on the model used to unfold the data, and thus large systematic uncertainties.

Finally, the photon structure function does not obey a momentum sum rule. There is no fixed probability for the photon fluctuating into a hadronic state, so the momentum carried by the quarks and gluons cannot be known without measuring it. It is therefore not possible to use the fraction of the photon's momentum carried by quarks to constrain the gluon content of the photon, G^γ; the total momentum in the the hadronic component of the photon and therefore the momentum carried by the gluon component is not determinable. Information on G^γ could be obtained from scaling violations of F_2^γ, however, due to the reasons stated above, the current measurements of F_2^γ are not sufficiently accurate for G^γ to be determined by this method.

1.7 Parametrisation of Photon Structure

The above effects allow much more freedom in the parametrisations of the quark densities in the photon compared to those in the proton. As with proton parton

distributions the approach used is to parametrise the photon structure function at a low energy scale, Q_0^2, then fit the parametrisation to higher Q^2 measurements by evolving the structure function with the GLAP equations. Currently available sets of photon parton distribution functions use several different input forms.

One approach is provided by the vector meson dominance model (VMD) where the resolved photon is assumed to have a parton distribution similar to a vector meson, such as the ρ [16]. The ρ structure function has however not been measured, and is instead approximated by the average of the π^+ and π^- structure functions. The VMD contribution to F_2^γ is then

$$F_2^{VMD}(x,Q_0^2) = \kappa \frac{4\pi\alpha_{em}}{f_\rho^2} \frac{(F_2^{\pi^+}(x,Q_0^2) + F_2^{\pi^-}(x,Q_0^2))}{2} \tag{1.23}$$

where κ is a constant which allows for $\gamma \to \phi$ or ω fluctuations in addition to the ρ. As in the treatment of proton structure functions the VMD contribution to the photon structure provides a parametrisation at a low energy scale Q_0^2 from which the photon structure function can then be evolved by application of the GLAP equations. The models of GRV [17] and AGCFP [18] only use the VMD component, but evolve it from $Q_0^2 = 0.25 - 0.30$ GeV^2. This value of Q_0^2 is arguably too low for the application of pQCD, but the parametrisations provide an adequate description of current data, and so cannot be rejected on this basis.

In the model of LAC [19], the photon is parametrised as the sum of a term representing perturbative $\gamma \to q\bar{q}$ splitting and a term motivated by counting rules of hadronic structure. The poor constraint provided by F_2^γ measurements on the gluon content of the photon was exploited in the LAC distributions by assuming extreme forms of the gluon distributions at Q_0. Of these distributions, LAC1 appears to be the only candidate which is in agreement with measurements of the total photoproduction cross section [20] and inclusive jet production at HERA [21]. The LAC1 gluon distribution is soft, but steeply rising at low x.

The GS [22] photon structure function uses a mixture of the above methods. It assumes a form containing a VMD component and a contribution from perturbative $\gamma \to q\bar{q}$ splitting. The input energy scale is $Q_0^2 = 5.3$ GeV^2 which avoids

doubts over the applicability of pQCD. Two parametrisations are provided, GS1, in which the gluon content arises from the VMD and perturbative components, and GS2, where the gluon content only arises from the VMD component of the photon.

Chapter 2

Models of the Hadronic Final State

While pQCD has been very successful in describing strong interaction processes involving large momentum transfers, a theory which allows calculations to be made at low momentum transfers where quarks and gluons form hadrons does not currently exist. Rather than a complete theory of strong interactions, phenomenology is used to parametrise or model hadronisation.

After a brief introduction to the phenomenology of fragmentation functions, the details of a leading and next-to-leading order calculation of $\pi^{\pm}$, $K^{\pm}$ and $K^0 + \bar{K}^0$ fragmentation functions, with which results will be compared, are given in section 2.3. An alternative approach to modelling hadronisation is provided by Monte Carlo techniques, and is described in section 2.4.

2.1 Fragmentation Functions

Fragmentation functions, $D_f^h(z, Q^2)$ are defined such that $D_f^h(z, Q^2)dz$ is the probability of a gluon or quark of flavour f producing a hadron h with momentum fraction of the parent in z, $z + dz$ within a distance $\mathcal{O}\ (1/Q)$. Fragmentation functions treat the production of each particle as though it was independent of the rest of the event and therefore can provide predictions of single particle

distributions. Neglecting masses, the momentum fraction, z, is defined as

$$z = \frac{\boldsymbol{p_h} \cdot \boldsymbol{p_{JET}}}{E_{JET}^2} \approx \frac{p_{hL}}{E_{JET}} \tag{2.1}$$

where p_{hL} denotes the momentum of a particle along the axis of the jet to which it is assigned, and jets are composed of massless particles [1]. Alternatively,

$$z = \frac{E_h}{E_f} \tag{2.2}$$

Both these definitions are used in this thesis. The definition in equation 2.1 is more suited to hadron-hadron colliders and is similar to that used by UA1 [23, 24] and CDF [25] in studies of jet fragmentation in $p\bar{p}$ collisions. The definition of equation 2.2 is used at e^+ e^- experiments, where it is equivalent to,

$$z = \frac{2E_h}{\sqrt{s}} \tag{2.3}$$

s being the centre-of-momentum energy. The fragmentation functions to which data will be compared are fits to measurements at e^+e^- experiments, and therefore used the definition in equation 2.2

Analogies exist between hadron structure functions and fragmentation functions; once a fragmentation function has been measured at a particular energy scale, Q_0, pQCD can be used to predict it at a different scale by use of the GLAP equations. Perturbative QCD predicts that fragmentation functions undergo logarithmic scaling violations with energy. The effects of logarithmic scaling are that a hadron is more likely to be produced at lower z from a high energy parton than from an identical lower energy parton. Constraints on fragmentation functions are placed by sum rules. For example, conservation of momentum gives the momentum sum rule.

$$\sum_h \int_0^1 z D_f^h dz = 1 \tag{2.4}$$

In addition, fragmentation functions are also believed to obey isospin and flavour relations, for example,

$$D_d^{\pi^+} = D_u^{\pi^-} = D_{\bar{u}}^{\pi^-} = D_{\bar{d}}^{\pi^+} \tag{2.5}$$

[1] The discussion of particle assignment to jets is deferred until later.

2.2 Measuring Fragmentation Functions

The process $e^+e^- \rightarrow q\bar{q}$ is ideally suited for measuring quark fragmentation functions; dijet events can be selected with an extremely high purity, e^+e^- annihilation events do not contain remnant jets from the beam particles and the energy scale of the interaction is unambiguously and accurately known to be the centre-of-momentum energy, enabling z to be determined accurately.

Measuring gluon fragmentation functions at e^+e^- experiments is harder as 3-jet events are suppressed by a factor of $\mathcal{O}(\alpha_s)$ relative to 2-jet events. According to pQCD, gluon fragmentation functions are expected to be different from quark fragmentation functions. Perturbative QCD calculations predict that the larger probability of a gluon to radiate another gluon rather than a quark, causes gluon jets to have a larger particle multiplicity, softer fragmentation function and larger angular width than quark jets of a similar energy. Confirmation of these predictions at e^+e^- experiments has proved difficult because in addition to the $\mathcal{O}(\alpha_s)$ suppression of 3-jet events, statistics are further reduced by event topology selection criteria which ensure the gluon and quark jets are of similar energy so that an unbiased comparison can be made. The DELPHI [26], ALEPH [27] and OPAL [28] collaborations have measured the gluon-to-charged particle fragmentation function and have confirmed the expected differences between quark and gluon jets. It is only recently that a study of identified particles within gluon jets has been performed by DELPHI [29].

2.3 Parametrisation of Fragmentation Functions

Leading and next-to-leading order (LO and NLO) quark and gluon-to- $\pi^{\pm}$, $K^{\pm}$ and $K^0 + \bar{K}^0$ fragmentation functions have been determined by Binnewies et al. [1, 2]. They parametrised fragmentation functions in the form

$$D_f^h(z, Q_0^2) = N_f z^{\alpha_f}(1-z)^{\beta_f} \tag{2.6}$$

where $f = u, d, s, c, b, g$ at $Q_0^2 = 2$ GeV^2. The free parameters of the fragmentation functions, N_f, α_f and β_f, were determined by fitting the energy fraction spectrum $\frac{1}{\sigma_{HAD}}\frac{d\sigma}{dz}$, of $\pi^{\pm}$, $K^{\pm}$ and $K^0 + \bar{K}^0$ measured in e^+ e^- annihilation. The $\pi^{\pm}$ and $K^{\pm}$ data were measured by the TPC collaboration [30] at $\sqrt{s} = 29$ GeV and the ALEPH collaboration [31, 32] at $\sqrt{s} = 91$ GeV. The K^0 data were measured by the Mark II collaboration [33] at $\sqrt{s} = 29$ GeV and ALEPH [34].

According to QCD, the energy spectra of hadrons of type h in e^+e^- annihilation is given by,

$$\frac{s}{\beta_h}\frac{d\sigma}{dx} = \sum_f \int_x^1 \frac{dz}{z} D_f^h(z,s)\frac{d\sigma_f}{dy}(\frac{x}{z}, s) \tag{2.7}$$

where $y = \frac{x}{z}$ and the sum is over all active partons. As for structure functions, the GLAP equations relate $D_f^h(z,s)$ to the input form $D_f^h(z,Q_0)$. Expressions for the parton level cross sections $\frac{d\sigma_f}{dy}(y,s)$ at LO and NLO are given in [35]. The only condition imposed on the fragmentation functions were $D_u^{\pi^+ + \pi^-} = D_d^{\pi^+ + \pi^-}$ and $D_s^{K^+ + K^-} = D_u^{K^+ + K^-}$. The ALEPH data [32] on charged hadron production is given for three cases; (*i*) sum over all quark flavours, (*ii*) sum over u, d, s quarks and (*iii*) b quarks; and is used to constrain the fragmentation functions for different flavoured quarks. For the gluon fragmentation function, $\alpha = -1$ or 0, gave reasonable descriptions of e^+e^- data. However, comparison of the gluon fragmentation function [35] to OPAL measurements [28] showed $\alpha = 0$ to be favoured by the data. Quark mass thresholds were accounted for during GLAP evolution, by including c and b quark fragmentation at energy scales $Q_0 = m(\eta_c) = 2.979$ GeV and $Q_0 = m(\Upsilon) = 9.460$ GeV, respectively.

The $K^0 + \bar{K}^0$ fragmentation functions [2] were obtained in a similar manner to the charged hadron fragmentation functions. The condition $D_s^{K^0 + \bar{K}^0} = D_u^{K^0 + \bar{K}^0}$ was applied. Unlike the charged particle fragmentation function calculations, no experimental information on the relative contributions of different quark flavours or the gluon to K^0 production in e^+ e^- annihilation was available. Gluon fragmentation into neutral kaons was therefore taken to be the same as in the charged particle fragmentation function analysis, thus, $D_g^{K^0 + \bar{K}^0} = D_g^{K^+ + K^-}$.

The fragmentation functions derived in [1, 2] from e^+e^- data and described in

section 2.3 are compared in this thesis to charged particle and K^0 fragmentation functions measured in hard photoproduction events at ZEUS. An attempt to separate gluon jets from quark jets is not attempted in this analysis. A first comparison between measured and predicted fragmentation functions in hard photoproduction, averaged over all quark flavours and the gluon is made, providing a limited test of the universality of fragmentation functions. Since no attempt is made to separate quark and gluon jets in the analysis presented in this thesis the subscript on $D_f^h(z, Q^2)$ will be dropped to denote it represents an average over quarks and gluons.

2.4 The PYTHIA Monte Carlo Model

Monte Carlo models provide a technique for simulating interactions in high energy physics. A model usually involves three stages:

- simulation of the hard scattering;
- perturbative evolution of scattered partons by parton showering;
- hadronisation.

The data in this analysis is compared to predictions of the PYTHIA [36, 37] Monte Carlo with hadronisation modelled by JETSET [38]. The generated sample of PYTHIA events were also used to calculate detector effects and efficiencies which were applied in order to make direct comparison between the data and PYTHIA predictions.

2.4.1 The Hard Scatter and Multiple Interactions

For photoproduction events generated in PYTHIA the hard scattering simulation starts by choosing the energy of the incident photon according to the Weizsäcker-Williams approximation. The initial quark and gluon momenta entering the hard scatter are then chosen from the parton distribution functions of the incident

particles. This procedure determines the energies of initial state particles. The energy and momentum of the final state quarks or gluons are then generated according to the first order cross sections for all possible QCD interactions. To avoid the low energy region where pQCD calculations are not applicable a transverse momentum cut-off, p_{Tmin}, is applied to the hard scatter.

It is possible in hadron-hadron interactions for more than one parton from each beam particle to interact and PYTHIA therefore includes an option for generating resolved photoproduction events with multiple parton-parton interactions. Multiple interactions (MI) are motivated by the differences between the predictions and measurements of total cross sections at high energy. The theoretical uncertainty and lack of measurements in the low-x region of parton distributions, and the divergence of pQCD calculations of the total cross sections as $p_{Tmin} \rightarrow 0$ means that many predictions exceed measurements [20, 39]. To avoid this problem total cross section measurements can be interpreted as hadron-hadron, rather than single parton-parton cross sections. The average number of parton-parton scatterings in an event,$< n_{scat} >$, is then given by

$$< n_{scat} >= \frac{\sigma_{hard}}{\sigma_{hadron}} \tag{2.8}$$

where σ_{hadron} is the total hadron-hadron cross section and σ_{hard} is the parton-parton cross section calculated according to

$$\sigma_{hard}(p_{Tmin}) = \int_{p_{Tmin}^2}^{s^2/4} \frac{\mathrm{d}\sigma}{\mathrm{d}p_T^2} \mathrm{d}p_T^2 \tag{2.9}$$

PYTHIA generates multiple interactions by calculating the mean number of parton-parton scatterings according to equations 2.8 and 2.9. The number of scatterings occurring in an event are determined using Poisson statistics, and each scattering is generated independently.

2.4.2 Parton Showers

As an approximation to higher-order QCD effects, Monte Carlo generators use a technique known as parton showering to simulate gluon radiation from the

incident and scattered partons. This method corrects the first order cross-section with logarithmic terms corresponding to successive $1 \rightarrow 2$ parton branchings. Two independent parton showers, initial and final state, are generated within PYTHIA. The GLAP splitting functions determine the momentum fractions of the radiated partons. In the initial state parton shower the incident partons become increasingly more virtual as they radiate gluons or quarks. After the hard scatter, the virtual partons radiate gluons or quarks, decreasing in virtuality until their mass reaches $m_{min} = 1$ GeV, where non-perturbative effects become large and the event simulation enters the hadronisation stage.

Theoretical studies and experimental measurements [40, 31, 41, 42, 43] have shown the need to take into account an effect known as coherence within parton showers. Coherence causes angular ordering of gluon emissions such that the angle at which gluons are emitted increases in the initial state parton shower and decreases in the final state parton shower. While coherence does not naturally arise from the approach to parton showers used in PYTHIA, its effects are simulated by forcing angular ordering of QCD radiation.

2.4.3 JETSET Hadronisation

The PYTHIA Monte Carlo uses the Lund string model [44] as implemented in JETSET to simulate hadronisation. The JETSET model is based on the description of confinement in section 1.3.

After the parton shower stage PYTHIA has produced a final state consisting of quarks and gluons which are viewed as having colour fields or 'strings' stretched between them. As the final state partons separate, it eventually becomes energetically more favourable for the string to break. In the Lund model, this process converts potential energy stored in the string into a $q\bar{q}$ pair.

When the colour field breaks the $q\bar{q}$ pair should be produced at the same point in space, otherwise local conservation laws such as those of charge and flavour would not be obeyed. However as some of the string's potential energy is converted into the quark and anti-quark's mass and momentum when the string

breaks, the Lund model appears not to satisfy these laws. This problem is avoided by postulating that the $q\bar{q}$ pair quantum mechanically tunnel from the same point in space (obeying local conservation laws) to the end of the string where they are then 'produced' with the requisite mass and momentum. The quantum mechanical tunnelling probablility for production of a quark or antiquark with mass m_q and transverse momentum relative to the string, p_T, is then given by

$$\mathcal{P} = \exp\left(-\frac{\pi m_q^2}{\kappa}\right) \exp\left(-\frac{\pi p_T^2}{\kappa}\right) \tag{2.10}$$

κ is the energy density of the string at large distances as in equation 1.3. This process continues until the remaining mass to be hadronised is about 1 GeV. The cut-off mass varies from event to event, and is chosen so that the rapidity distribution of particles in the centre-of-momentum system is flat. At this point all quarks and anti-quarks are grouped into hadrons.

The lower production rate of hadrons containing s valence quarks relative to hadrons containing only u and d valence quarks is then explained in the Lund model as due to the larger s quark mass relative to u and d quark masses. The relative rates of $u : d : s$ $q\bar{q}$ pair production in JETSET is given by $1{:}1{:}P_s/Pu$ where P_s/P_u is the strangeness suppression factor with default value $P_s/P_u = 0.3$. This value is not well determined since confinement prevents the quark masses from being directly measured experimentally, and at present there is no theoretical method of predicting the quark masses. By this argument c or heavier quark production is suppressed by a factor $\mathcal{O}(10^{-13})$ and so are not produced by this method.

In addition to predicting overall particle production rates, Monte Carlo models must be able to simulate hadron momentum spectra. JETSET uses the Lund symmetric fragmentation function as default,

$$D(z) = z^{-1}(1-z)^a \exp\left(-bm_T^2/z\right) \tag{2.11}$$

where

$$m_T^2 = E^2 - p_z^2 = m^2 + p_x^2 + p_y^2 \tag{2.12}$$

is the 'transverse mass' of a hadron with 4-momentum (E, p_x, p_y, p_z), z is the hadron momentum in units of its parent quark momentum, and a and b are free parameters which control the shape of the fragmentation function at high and low z, and the transverse momentum which $q\bar{q}$ pairs are created with. This form is derived from the condition that the momentum distribution of final state particles does not depend on the end of the string from which the fragmentation started.

The treatment of hadronisation in gluon jets was neglected in the above discussion. As already discussed in section 2.3, differences between quark and gluon fragmentation functions are expected. Since the resolved process is dominant in the kinematic region studied in this analysis, most events contain a hard final state gluon jet and so the JETSET simulation of gluon jet hadronisation will be tested in this analysis. Lorentz invariance requires that the hadronisation of high energy gluon jets is the same as gluons produced in the parton shower stage, and it is the latter case which will be considered here. In the Lund model, gluons are viewed as kinks on the string. Quark-antiquark pairs are produced in the string as described earlier. The gluon combines with a quark and antiquark produced by the string on either side of the kink to form a hadron, with the constraint that the hadron has the correct mass. Hadronisation of the strings on either side of the gluon then proceeds as in quark jets with $q\bar{q}$ pair production. Gluons are effectively treated as consisting of two colour fields and this provides the Lund model explanation for differences between quark and gluon jet fragmentation.

2.4.4 Refinements to Hadronisation Models

A more complete description of hadron production requires simulation of other processes, such as production of higher spin states and baryon production. This leads to a large number of parameters within the Lund model to control particle production rates. Baryon production is simulated in JETSET by the 'popcorn' mechanism in which $q\bar{q}$ pairs are successively produced in the field between other $q\bar{q}$ pairs to form qqq and $\bar{q}\bar{q}\bar{q}$ states. The 'popcorn' mechanism derives its name from the fact that the innermost $q\bar{q}$ pair may combine to form a meson

(M), leaving the outer qq $\bar{q}\bar{q}$ pairs to combine with neighbouring quarks and antiquarks. In this way, baryon anti-baryon ($B\bar{B}$) pairs do not always appear next to each other in the fragmentation chain. The magnitude of the popcorn parameter determines the relative occurrence of $B\bar{B}$: $BM\bar{B}$ combinations in fragmentation. Particles are also produced by decays of heavy quark or excited states so that uncertainties in branching ratios of such states lead to uncertainties in the modelled production rate and momentum spectra of lighter hadrons. There is also possible evidence that Bose-Einstein correlations [34, 45] should be considered in determining the hadronic final state of events containing two identical particles. The effects described in this section are, however, beyond the scope of the analysis presented in this thesis.

2.5 Monte Carlo Samples

'Enriched' samples of resolved and direct photoproduction events containing at least one hadron jet as defined in section 5.1 satisfying $E_T^{HAD} > 5$ GeV and $|\eta^{HAD}| < 2.5$ were generated separately, with $p_{Tmin} = 2.5$ GeV using the GRV LHO photon and MRSA proton parton distribution functions. This value of p_{Tmin} was chosen since it was the highest value of p_{Tmin} at which the cross section for production of jets with $E_T > 5$ GeV was independent of p_{Tmin}. By using samples of unenriched PYTHIA events it was found that more than 97 % of all resolved and 99 % of all direct events which satisfied the calorimeter jet cuts discussed in section 5.2 also passed the jet enrichment cuts applied at the event generation stage. The data is also compared to a sample of PYTHIA events generated with $P_s/P_u = 0.20$, and to PYTHIA with multiple interactions both using the GRV LO photon parton distribution function. The resolved and direct events in each sample were combined according to their cross-sections, to produce a full set of photoproduction events.

Chapter 3

The HERA Accelerator and ZEUS Experiment

3.1 The HERA Accelerator

HERA (the **H**adron-**E**lektron-Speicher**R**ing-**A**nlage) at DESY, Hamburg, is the world's first high energy $e^{\pm}p$ colliding beam facility. The ring is 6.3 km in circumference and was designed to collide 30 GeV electrons or positrons with 820 GeV protons at four interaction points. The nominal centre-of-momentum energy available in these collisions is therefore 314 GeV equivalent to a 53 TeV beam incident on a fixed target. HERA was designed to operate at a luminosity of $1.5\text{x}10^{31}$ $\text{cm}^{-2}\text{s}^{-1}$, to be achieved by colliding 60 mA $e^{\pm}$ and 160 mA p in 220 bunches, with a bunch crossing interval of 96 ns. Of the 220 bunches in each beam 10 were to be empty to enable background studies. These design specifications placed stringent conditions on the design of the ZEUS detector and trigger system, which will be discussed in later sections.

The layout of the HERA injection system and the HERA accelerator are shown in figures 3.1 and 3.2 respectively. Proton injection starts with the acceleration of unbunched H^- ions to 50 MeV in the Proton Linac. The H^- ions are stripped and bunched in DESY III, where they are accelerated to 7.5 GeV. Once 70 bunches are transferred to PETRA the protons are accelerated to 40 GeV, then injected

into the HERA proton storage ring. The injection process is repeated twice, then the 210 bunch p beam is accelerated to 820 GeV.

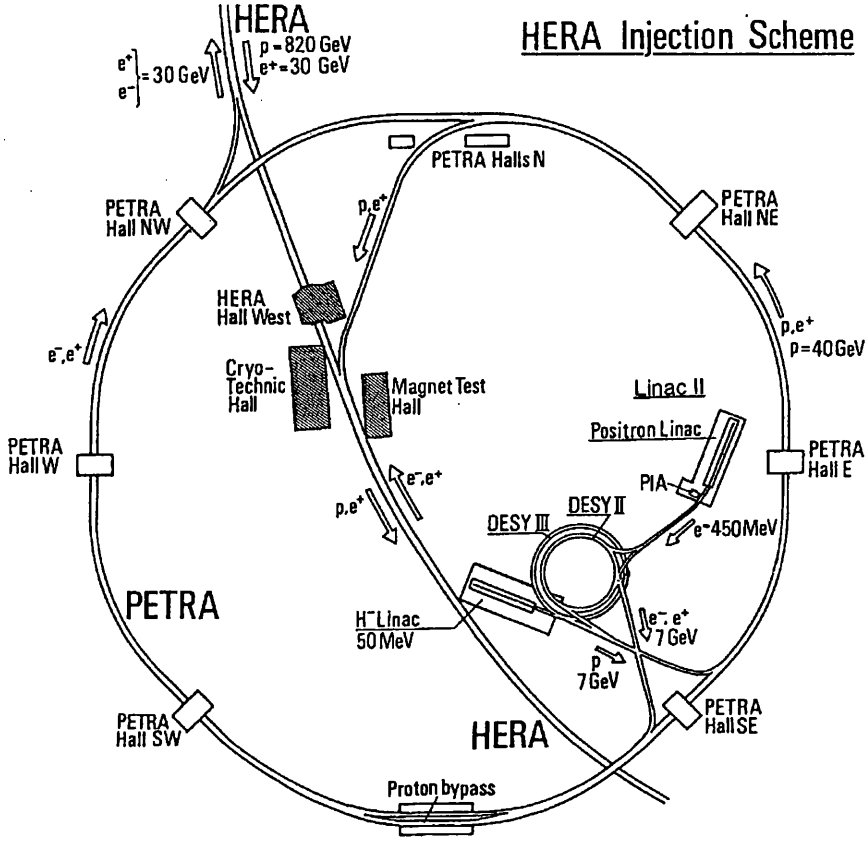

Figure 3.1: The HERA injection system.

Electrons or positrons are initially accelerated to 450 MeV in LINAC2, and accumulated in PiA as a single bunch. The e^+/e^- bunch is transferred to DESY II for acceleration to 7.5 GeV, then into PETRA. When 70 bunches are stored in PETRA they are accelerated to 14 GeV, then injected into the HERA electron storage ring to be accelerated to their full energy.

To maintain a 30 GeV e^+/e^- beam orbit, a 0.165 T bending field is required. This is achieved with the use of conventional magnets. To maintain the p beam orbit, a bending field of 4.65 T is required. This is provided by superconducting magnets. Synchrotron radiation is a major energy loss for the e^+/e^- beam. This is compensated for by use of radio-frequency cavities.

In 1994, HERA operated for a short period in e^-p mode then switched to e^+p

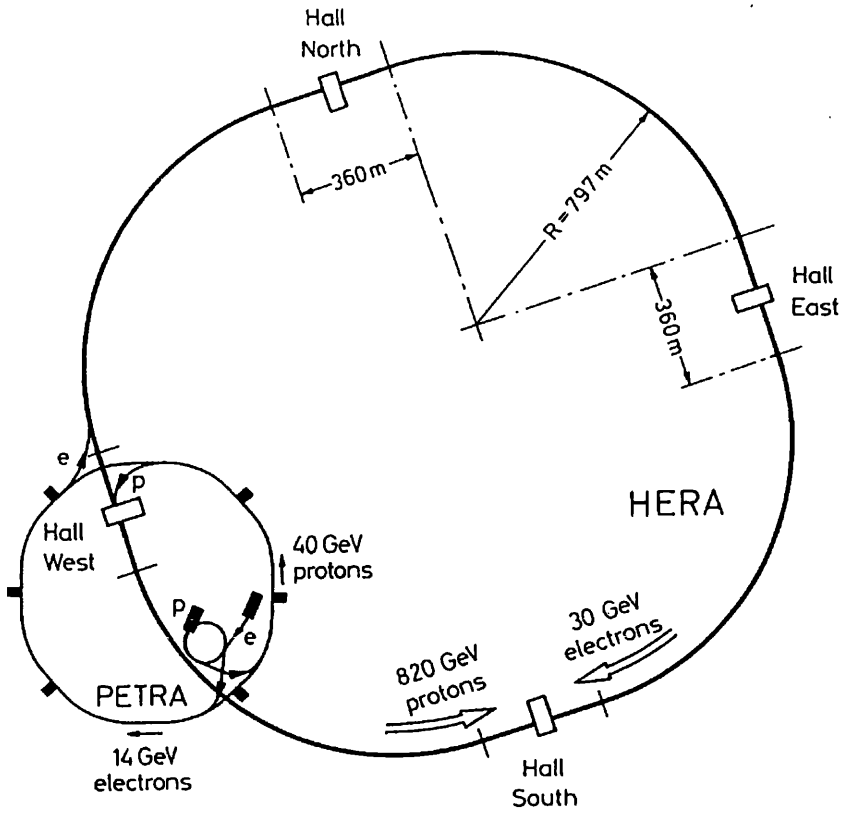

Figure 3.2: The HERA Accelerator.

running, as the e^+ beam had a lifetime approximately a factor of two longer than the e^- beam. The beam energies were 27.52 GeV and 820 GeV. HERA ran with 153 paired e^+p bunches, 15 unpaired (pilot) $e^\pm$ bunches and 17 p pilot bunches. From the 6.2 pb^{-1} integrated luminosity delivered by HERA, 3.3 pb^{-1} of data was written to tape.

3.2 The ZEUS Detector

The ZEUS detector has been described in detail in [46]. ZEUS employs a right-handed coordinate system with the $+z$-axis defined as the proton beam direction. Polar angles are measured with respect to the $+z$ (forward) direction. The asymmetric detector configuration reflects the difference in the initial state $e^\pm$ and p energies, which leads to a greater density of high energy particles being produced in the forward direction.

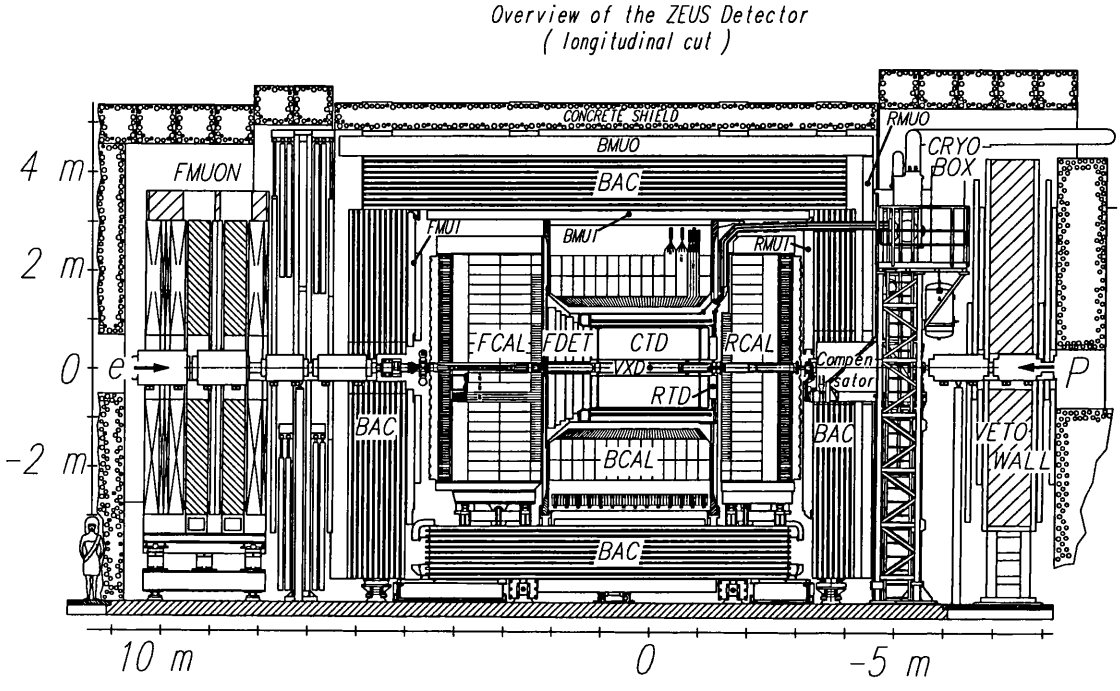

Figure 3.3: Longitudinal cross-section of the ZEUS Detector.

A longitudinal cross section of ZEUS is shown in figure 3.3. The e^+ and p beams collide in a 9 cm radius aluminium beampipe. Charged particles are observed with the Vertex and Central Tracking Detectors (VXD, CTD). The solenoid magnet provides a 1.43 T magnetic field with which to determine particle charge, momentum. The Vertex Detector (VXD) improves the charged particle momentum resolution over the CTD alone, and aids reconstruction of short lived particles. Tracking acceptance is increased in the forward direction by the Forward Tracking Detectors (FTD) and in the rear direction by the Rear Tracking Detector (RTD). In the future, Transition Radiation Detectors will enhance particle identification in the forward direction. In 1994, the VXD, CTD and RTD were operational and equipped with readout electronics.

Charged and neutral particle energies are measured in the Uranium Calorimeter (UCAL) which is split into three parts, forward, barrel and rear (FCAL,

BCAL, RCAL). The magnet yoke is instrumented to act as a backing calorimeter (BAC) for energy deposits not fully contained in the UCAL, and also acts as a muon tagger. Muon detectors are installed on the inner (FMUI, BMUI, RMUI) and outer (BMUO, RMUO) surfaces of the BAC. Muons produced at small angles in the proton direction enter the Forward Muon Detector (FMUON). A toroidal 1.7 T magnet within the FMUON improves their momentum measurement over that from the CTD and VXD alone.

Other components not shown in figure 3.3 provide small angle tagging for low momentum transfer processes. The Luminosity Monitor consists of two calorimeters, EDET and GDET, 35 and 107 m downstream in the e^+ direction, which tag the e^+ and γ from bremsstrahlung interactions. The EDET is also used to tag photoproduction events. The Leading Proton Spectrometer (LPS), which comprises a series of six silicon planes stationed between 24 and 90 m, tags events where the proton is scattered at low angles.

3.2.1 Inner Tracking Detectors

The tracking detectors were designed to provide reconstruction of final state particles with high position and momentum resolution over a wide angular range. In order to study heavy flavour production and to act as a probe for new physics, accurate primary and secondary vertex reconstruction was also required. A tracking trigger based on the primary vertex position was considered vital to reduce the number of accepted events from p beam gas interactions. This trigger is also desirable for retaining charged current events.

Vertex Detector

The VXD is a high precision drift chamber positioned between the beampipe and CTD. It has an active length of 1.59 m and inner and outer active radii of 99 and 142 mm respectively. There are 12 radial layers of sense wires, which form 120 drift cells in azimuth. The sense wires lie parallel to the VXD axis. A stainless steel flange houses the readout electronics at the rear of the VXD.

All other walls are made from carbon fibre to minimise particle scattering and photon conversions.

The chamber is operated at an electric field of 2 kV/cm and is flushed with DME gas. The angle between ionisation drift and the negative electric field direction (the Lorentz angle) is small, 5°. The small Lorentz angle in addition to the fact that the VXD axis is not coincident with the beam axis means the left-right ambiguity is solved without requiring tilted drift cells. The single hit resolution ranges from 50 μm in the cell centre to 150 μm at the cell edges.

Central Tracking Detector

The CTD is a cylindrical drift chamber, with an active volume 2m in length, extending between 190 and 785 mm radially from the HERA beamline. It provides tracking information for particles emerging in the polar angle range 15° to 154°. An octant of the CTD is shown in figure 3.4. The CTD contains concentric field and sense wire layers, which are grouped into 9 superlayers. The wires in odd superlayers are strung parallel to the ZEUS z-axis; these are called axial superlayers. Wires in even numbered superlayers lie at small angles ($\pm 5°$) to the ZEUS z-axis; these are called stereo superlayers. Each superlayer is further divided into cells containing a plane of alternating sense and field wires, bounded on either side by a plane of field wires. There are 576 cells in total, each containing 8 sense wires. The number of cells increases with superlayer number such that the maximum drift distance in any cell is $\sim$ 25 mm. Cells are rotated such that a radius vector at the cell centre would make an angle of 45° with the sense wire plane.

The CTD was flushed with a 85:8:7 mixture of Ar:CO_2:C_2H_6 bubbled through ethanol. The gas was chosen due to its high drift velocity, typically 50 μm/ns and results in a high Lorentz angle, 43°. The direction of the Lorentz angle is opposite to the sense plane tilt, to obtain azimuthal ionisation drift. This gives optimal resolution for high p_T tracks. The choice of a high drift velocity gas enables the CTD to participate in the First Level Trigger.

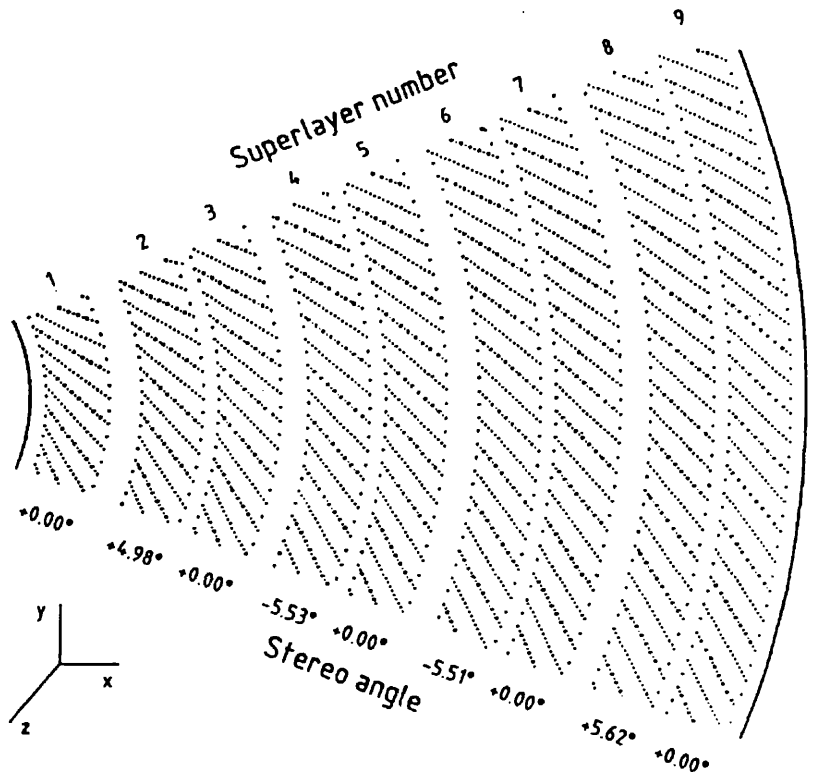

Figure 3.4: An octant of the CTD.

Signals induced in the sense wires by charged particles ionising the CTD gas are read out by two electronic systems, the z-by-timing and r-ϕ systems.

All wires in superlayer 1, and alternate wires in superlayers 3 and 5 are equipped with z-by-timing electronics. The time difference between pulses propagating in opposite directions along sense wires is used to measure the z-position of particle tracks with a resolution of 4 cm. This information allows the First Level Trigger to estimate if an event contains tracks consistent with an e^+p interaction at the nominal interaction point. Pattern recognition and track fitting also uses the z-by-timing information as an aid in determining the polar angle of tracks. The z-by-timing system is concentrated in inner superlayers to provide good acceptance for z measurement of tracks at extreme polar angles.

All sense wires are used in the r-ϕ system. Each sense wire is read out by a flash-analogue-to-digital converter (FADC), into a 10 μs pipeline. If the first level

trigger accepts an event the pipeline is frozen and the pulseheight spectrum is read out by the data acquisition system. The drift time of a signal is determined by a constant-fraction algorithm and is measured relative to the HERA clock. The pulse height spectrum can also be used for particle identification by dE/dx.

The 45° sense plane tilt allows easy resolution of the left-right ambiguity. The distance from the sense plane at which a charged particle created ionisation is calculated from the drift time and drift velocities. When reconstructed at the correct position the 'hits' form track segments in each superlayer lying along a helical track originating from the interaction point. If the hit is reconstructed on the wrong side of the sense plane, the resulting segment of 'ghost' hits neither points toward the interaction point, nor towards a segment in another superlayer. Due to the tilted sense planes, unambiguous assignment of tracks to an event is accomplished. High p_T tracks cross at least one sense plane in each superlayer and therefore have at least one hit less than 96 ns. Furthermore, the assignment of hits to the wrong event means track segments lose hits outside cell boundaries and are discontinuous at the sense plane. The single hit resolution achieved for high p_T tracks perpendicular to the z-axis in 1994 was $\sigma_{r\phi} = 190$ μm. Stereo superlayers provide tracking information in the z-direction. The nominal single hit resolution in the z-direction for stereo superlayer hits is $\sigma_z = 1.6$ mm. The CTD gives an accuracy on track impact parameters of 300 μm over much of its polar angle coverage. This is improved by a factor of 2 to 3 when combined with the VXD tracking.

Forward and Rear Tracking Detectors

In order to provide angular coverage for track reconstruction at small and large polar angles where the CTD acceptance is low, three (one) planar drift chambers are installed in the forward (rear) directions. The Forward and Rear Tracking Detectors provide polar angle coverage for track reconstruction in the polar angle ranges $7.5° < \theta° < 28°$ and $160° < \theta° < 170°$ respectively. The asymmetry in the initial state $e^{\pm}p$ energies will produce dense jets in the forward direction. Hence

three chambers were installed there to allow track reconstruction and linking to the CTD and VXD. The FTD chambers are separated by two 210 mm gaps which contain the Transition Radiation Detectors. The RTD improves measurement of the scattered $e^{\pm}$ angle in low momentum transfer DIS.

Each planar drift chamber has the same structure. Three layers of wires are strung perpendicular to the beam axis. Each successive layer is rotated by 120° with respect to the previous layer and contains cells of six sense wires. The sense wires are staggered by ± 150 μm with respect to the median line through the cell. This allows resolution of the left-right ambiguity at an early stage of track reconstruction. The drift chambers are flushed with $Ar/CH_4(50/50)$.

In the 1994 running period only the RTD was fully equipped with FADC readout electronics. The single hit resolution obtained was 160 μm [47].

3.2.2 The Uranium Calorimeter

The aim of the Uranium Calorimeter is to enable accurate reconstruction of the kinematics and energy flow in an event, and thus good energy resolution and containment are required. It has to provide energy measurements for neutral particles not measured in the tracking detectors, in addition to charged particles produced inside and outside the acceptance of the tracking detectors. To compliment the tracking resolution the calorimeter was designed to provide good angular resolution to enable jet structure to be studied and separation of jets to be achieved. The UCAL is also designed to provide the main mode of triggering, by means of global energy sums, missing transverse energy sums, and identification of likely scattered $e^{\pm}$ candidates in DIS events.

The UCAL is divided into three distinct components.

- Forward calorimeter, FCAL, covering polar angles from $2.2° \leq \theta \leq 39.9°$;
- Barrel calorimeter, BCAL, covering $26.7° \leq \theta \leq 129.1°$;
- Rear calorimeter, RCAL, covering $128.1° \leq \theta \leq 176.5°$;

The total solid angle coverage is 99.8% in the forward and 99.5% in the rear hemispheres. Geometrical acceptance losses arise only from particles leaving the interaction region by the HERA beampipe.

Each of the three calorimeter components are built in a similar modular structure, the basis of which is a 'tower' of alternating depleted uranium (DU) and plastic scintillator tiles. A typical FCAL module is shown in figure 3.5. Each calorimeter tower is divided into electromagnetic (EMC) and hadronic (HAC) sections. The DU and scintillator tiles are 3.3 cm (equivalent to 1 X_0[1]) and 2.6 cm thick respectively. The scintillator tile thickness was chosen to achieve 'compensation' which is discussed later. The DU tiles are clad with stainless steel of thickness 0.2 mm (0.4 mm) in the EMC (HAC). This serves to reduce noise due to uranium decays, while still allowing the uranium to act as a calibration source.

The EMC is segmented into cells of dimension 5x20 cm^2 and 10x20 cm^2 in the FCAL and RCAL respectively. The EMC cells are 25 X_0 deep, and have a nuclear interaction length of $\sim 1\lambda$ [2]. There are two HAC sections in the FCAL and BCAL, but only one in the RCAL, the HAC depth varying from $\sim 6\lambda$ in the FCAL to $\sim 3\lambda$ in the RCAL. The larger HAC depth in FCAL and BCAL is required to contain showers from the greater number of highly energetic particles produced in the forward direction. Beam tests showed the HAC to contain 95% of the energy for 90% of all jets. The cells in FCAL and RCAL are non-projective in polar and azimuthal angle. In the BCAL, EMC and HAC cells are projective in azimuth. BCAL EMC cells are almost projective in polar angle. To prevent particles from escaping from the interaction point through gaps between the BCAL modules, BCAL modules are rotated by 2.5° away from the radial direction in azimuth.

Each calorimeter cell is read out on two sides by wavelength shifter plastic scintillator bars which also operate as light guides connecting the cells to

[1]The radiation length of a material, X_0, is the distance at which the energies of $e^{\pm}$ and γ's in an electromagnetic shower are a fraction $1/e$ of the energy of the initiating particle.

[2]The nuclear interaction length, λ, is the distance at which the energies of particles in a shower induced by a hadron are a fraction $1/e$ of the initiating hadron's energy.

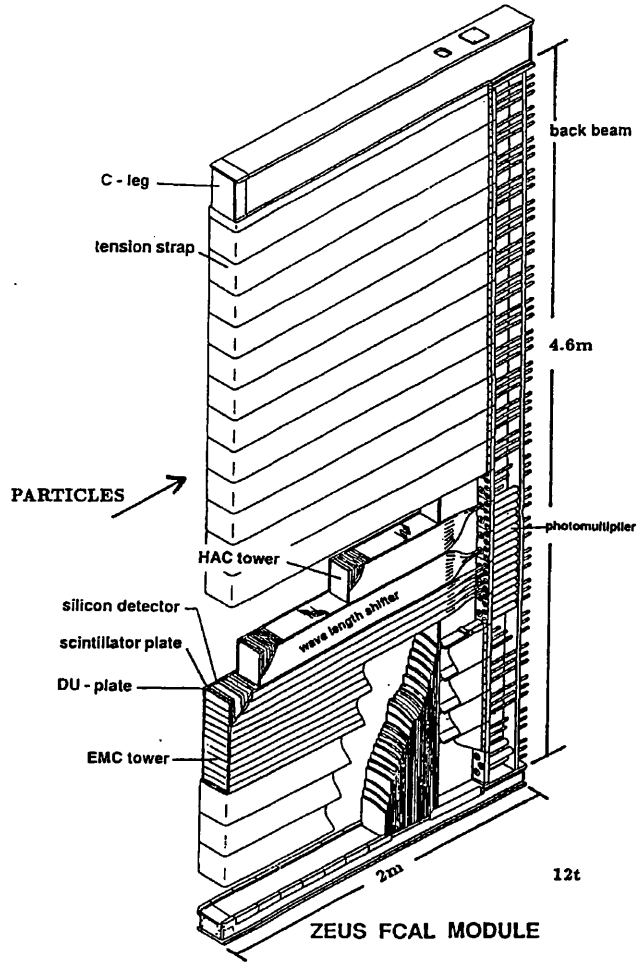

Figure 3.5: An FCAL module.

photomultiplier tubes. The wavelength shifter contains a fluorescent dye chosen because its absorption and emission suitably matches the scintillator tile emission and photomultiplier tube response, respectively. The use of scintillator and photomultipliers in the readout system gives fast pulse rise times and good timing resolution, $\sigma_t = 500 + 1500/\sqrt{E}$ ps for particles of energy, E, in GeV. Thus, for a 10 GeV particle $\sigma_t \sim 1$ ns. This enables the calorimeter to be used in the trigger; events can be accepted or rejected depending on whether calorimeter timing signals are consistent with a physics or background event. Pile-up is avoided since pulses are shorter than the 96 ns bunch crossing interval.

The thicknesses of the depleted uranium and plastic scintillator tiles were

chosen so that the UCAL is compensating; it gives an equal response to electrons and hadrons of the same energy, and hence optimal energy resolution for hadronic showers. The energy resolution of hadronic calorimeters is worse than electromagnetic calorimeters because statistical fluctuations in the π^0 content of hadronic showers result in variations of the nuclear and electromagnetic shower components. The shower of electrons, positrons and photons generated by an electromagnetic particle contains essentially all the energy of the initiating particle. However, the shower generated by a hadron typically has $15 - 20$ % energy less than the initiating hadron. The energy lost is used for ν-production and overcoming nuclear binding energy in nuclear break-up.

By using depleted uranium as absorber, it is possible to compensate for this energy loss. Slow neutrons produced in nuclear break-up undergo np scattering in the scintillator producing recoil protons with low energy. These protons create regions of very high ionisation density in the scintillator, boosting the scintillation light output and therefore the measured shower energy. The nominal energy resolution of the UCAL is

$$\frac{\sigma_E}{E} = \frac{18\%}{\sqrt{E}} \oplus 1\%$$

for electrons, and

$$\frac{\sigma_E}{E} = \frac{35\%}{\sqrt{E}} \oplus 2\%$$

for hadrons. (E is in GeV and $\oplus$ stands for addition in quadrature.)

3.2.3 Backing Calorimeter

The Backing Calorimeter consists of 3.7 cm thick aluminium proportional tube modules separated by 7.3 cm thick iron plates which provide the return path for the solenoid field. It provides additional energy measurement for showers not contained in the UCAL and also acts as part of the muon trigger in the bottom yoke where no muon chambers are present.

The energy deposited in the BAC is measured by the wires of the proportional tubes with an energy resolution for hadrons of $\sigma_E/E \sim 1/\sqrt{E}$. Position

measurement is by aluminium cathode pads. Three layers in the bottom yoke are provided with special pads giving a spatial resolution of about 1mm along the tubes. The magnetisation of the iron by the solenoid return flux is weak and non-uniform. Therefore conducting coils are added which provide a toroidal magnetic field of about 1.6 T enabling muon momentum measurement.

3.2.4 Luminosity Monitor

The Luminosity Monitor [48] consists of two separate sampling calorimeters for detecting low angle scattered e^+ and photons emitted by the bremsstrahlung process $ep \rightarrow ep\gamma$. The scattered e^+ are detected in the electron detector (EDET) at 35 m from the interaction point, and bremsstrahlung photons in the photon detector (GDET) at a distance of $104-107$ m from the interaction point as shown in figure 3.6.

Scattered e^+ in the energy range $0.2E_e < E'_e < 0.9E_e$ and $\theta \leq 6$ mrad are deflected out of the $e^\pm$ beam by the HERA magnet system into the EDET. The EDET is stationed behind a stainless steel window in the e^+ beam pipe. It consists of a lead/scintillator sandwich calorimeter which measures the scattered e^+ energy, and scintillator fingers to measure the position of the scattered electron.

The GDET detects bremsstrahlung photons emitted at angles $\theta \leq 0.5$ mrad down the proton beam-pipe leaving through a copper-beryllium window at a bend in the p beam-pipe 80 m from the interaction point. A carbon filter of thickness $0.5-3.5X_0$ absorbs synchrotron radiation. An air filled Čerenkov counter behind the carbon filter vetoes events where a photon has pair produced in the carbon filter. The photon energy is measured in a lead/scintillator sandwich calorimeter behind the Čerenkov counter. Two crossed planes of scintillator fingers at a depth of $7X_0$ in the calorimeter provide a measurement of the photon position. The scintillator plates are read out by wavelength shifter bars and photomultiplier tubes, the scintillator fingers by photodiodes.

The luminosity is determined from the Bethe-Heitler process, $ep \rightarrow ep\gamma$, by measuring the rate of bremsstrahlung photons, R_γ in the GDET. The cross-

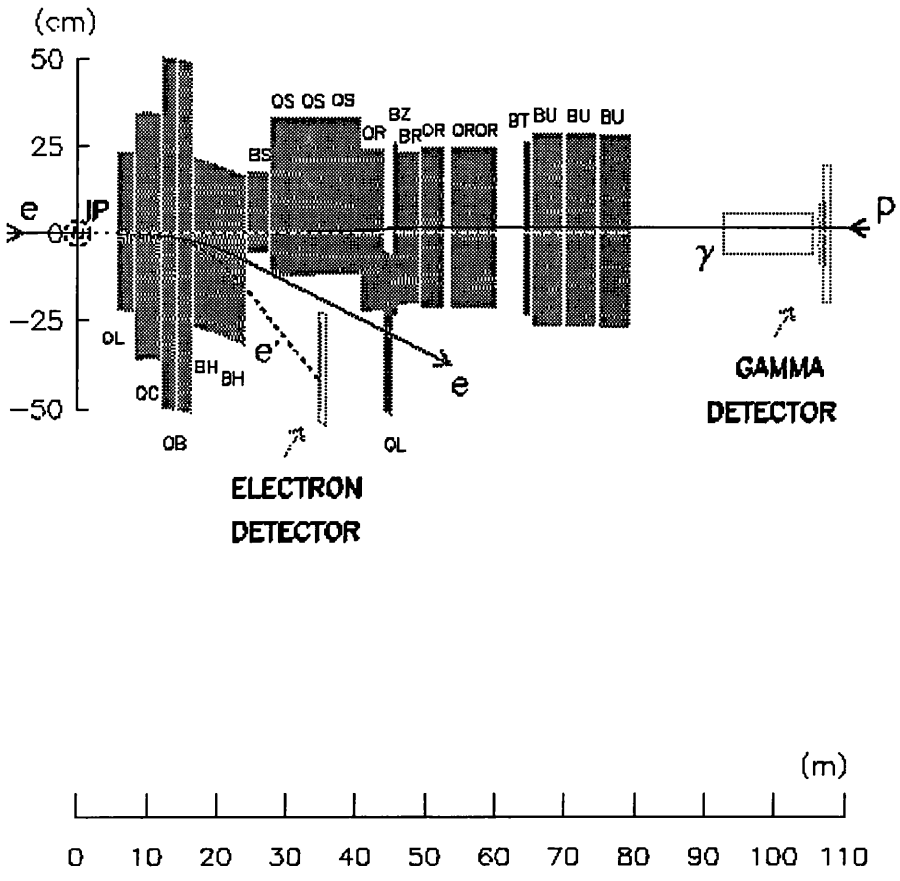

Figure 3.6: The layout of the Luminosity monitor.

section for this process, σ_{BH}, is theoretically well known [49]. However, before converting the measured photon bremsstrahlung rate into a luminosity, the background rate from e^+ beam gas interactions has to be subtracted. This is done by measuring the rate of bremsstrahlung photons from e^+pilot bunch crossings, $R_{e-pilot}$. The true rate of bremsstrahlung photons from the Bethe-Heitler process is then

$$R_{ep} = R_\gamma - \frac{I_{ep}}{I_{e-pilot}} R_{e-pilot} \tag{3.1}$$

where I_{ep} are the currents of the e^+ bunches paired with p bunches and $I_{e-pilot}$ is the current in e^+ pilot bunches. The luminosity is then determined by

$$\mathcal{L} = \frac{R_{ep}}{\sigma_{BH}} \tag{3.2}$$

The luminosity monitor is also used to tag photoproduction events when the

scattered e^+ gives a signal in the EDET but there is no photon signal in the GDET. Radiative events are tagged by a photon signal in the GDET with the absence of an e^+ signal in the EDET.

3.2.5 Background Rejection

Out of time p beam induced background events are rejected using timing measurements from a series of detectors stationed on the p beamline before the ZEUS detector. The VETOWALL at $z = -7.3$ m consists of an 87 cm thick iron wall with scintillator hodoscopes on each side. It protects the main detector from the p beam halo as well as providing timing measurements. The C5 counter, a lead/scintillator counter at $z = -3.2$ m and the SRTD, a silicon pad tracking detector on the inner face of the RCAL provide timing measurements for rejecting p beam induced events occurring between the VETOWALL and nominal interaction point.

3.3 The ZEUS Trigger

Since bunch crossings occur every 96 ns the trigger has to be capable of handling a rate of 10 MHz. The actual event rate from e^+p interactions is expected to be $\sim$ 240 Hz dominated by photoproduction processes at a luminosity of 2×10^{31} cm^{-2}s^{-1}. This rate is swamped by background processes such as p beam-gas interactions, synchrotron radiation and cosmic rays which occur typically at the level of 10^5 Hz at the HERA design luminosity. ZEUS uses a three level trigger which reduces the rate from $\sim 10^5$ Hz to < 5 Hz, the maximum speed with which events can be written to tape.

The First Level Trigger (FLT) aims to reduce the rate from $\sim 10^5$ Hz to ~ 1 kHz. FLT decisions are based mainly on UCAL and CTD information, but also use the F/BMUON, BAC, LUMI, LPS and VETOWALL. The FLT accepts events passing total energy, total transverse energy and missing energy sums calculated from the UCAL information, or which have a primary vertex consistent with an

e^+p interaction as determined by the CTD z-by-timing tracking. Tracks found by the z-by-timing system are classified according to whether they do or do not point towards the primary vertex; tracks pointing to the primary vertex are 'good' tracks, otherwise they are called 'any' tracks. Less stringent UCAL and CTD requirements are placed on events tagged by the LUMI or LPS. Each FLT component has a 5 μs pipeline which stores data from every bunch crossing. After 2.6 μs every component sends a decision to the Global First Level Trigger, which accepts or rejects events 4.4 μs after the event entered the pipeline. Accepted events are then sent to the Second Level Trigger.

The Second Level Trigger (SLT) analyses in more detail events passing the FLT. At an input rate of 1 kHz the SLT aims to reduce the background rate by a factor of 10. More accurate calculations than are possible at the FLT are made on parallel transputers. The UCAL SLT calculates similar energy sums to the FLT but uses individual cells in the calculation. Calorimeter timing is also used to discriminate between physics and background events. The Global Second Level Trigger (GSLT) combines results of second level component triggers, passing accepted events to the Event Builder.

The Event Builder combines data from each component for analysis by the Third Level Trigger (TLT) which runs on a farm of SGI workstations. The TLT runs a simplified version of the offline reconstruction code, providing for example, a full 3d track and vertex fit and jet finding. According to the results of the reconstruction the TLT identifies potentially good events, reducing an input rate of $\sim$ 100 Hz to an output rate of 3-5 Hz. Events passing the TLT are sent over a high speed optical line to an IBM mainframe which writes them to tape.

3.4 ZEUS Detector Simulation and Reconstruction Software

Apart from providing predictions of physics at HERA, Monte Carlos are used to understand effects due to detector response in the data. This is achieved by

treating the output from an event generator as though it were actual data from a real e^+p collision and analysing it with the same software used for actual data. The event simulation procedure has three stages.

ZDIS The ZEUS interface to Monte Carlo generators. The output of this stage consists of particles and their 4-vectors. This information is kept through the whole detector simulation and event reconstruction process to allow an understanding of how the observed distributions in the data are related to the true generated distributions.

MOZART The final state particles produced by ZDIS are propagated through the components of the ZEUS detector. The GEANT [50] package simulates the effects of the magnetic field, particle energy loss and multiple scattering on the generated particles. The output from this stage contains for example raw hits in the CTD and energy deposits in the UCAL which can then be used in the full event reconstruction.

ZGANA The ZEUS trigger simulation.

3.4.1 Event Reconstruction

Events are reconstructed by the program ZEPHYR. It uses as input either 'real' events recorded by the ZEUS detector, or Monte Carlo events which have been processed by the detector simulation, MOZART, and the trigger simulation, ZGANA. ZEPHYR reconstructs events in several phases.

Phase 1 The calibrated raw data in each component is used to give physics information, for example, tracks in the CTD and VXD and cell energies in the UCAL.

Phase 2 Global aspects of the event reconstruction are performed, for example, linking tracks in the different tracking chambers, and matching tracks to energy deposits in the UCAL.

Phase 3 Combines measurements from several detectors to provide a more detailed understanding of an event and is intended for running standard analysis algorithms, such as e^+ identification routines and jet finders. In 1994 only e^+ finder algorithms were ran in phase 3.

DST selection The outcome of the event reconstruction is analysed by a physics filter routine and used to set DST (Data Summary Tape) bits to classify events. These allow quick selection of events during analysis by identifying events which, for example, contain a high transverse energy jet.

Track Reconstruction

The K^0 reconstruction algorithm employed in this analysis uses as its input, tracks from the reconstruction program VCTRAK [51]. In the first stage of the track reconstruction pattern recognition is performed which identifies candidate tracks. The second stage determines particle trajectories by a helix fit to the candidate tracks.

The pattern recognition stage starts track candidates from a segment of three axial seed hits in an outer CTD superlayer. Axial layer hits are added as the candidate trajectory is extended inwards. To guide the trajectory inwards a broad virtual hit at $x = y = 0$ is used. Hits from the z-by-timing system are matched to the resulting trajectory to estimate the intercept and slope of the track with respect to the z-direction. Stereo superlayer hits are then matched to the track by interpolating the circular trajectory between axial superlayers.

Track candidates are then fitted to a 5-parameter helix model by extrapolating the trajectory provided by the pattern recognition outwards from the innermost hit. From the helix fit determined at one layer, the distance between the extrapolated track and the measured hit at the next layer is calculated. This provides an estimate of the error on the next point on the trajectory, to which the helix fit is applied. The process of extrapolating the track outwards and repeating the helix fit is performed until the final hit on the track has been used.

The track fit calculates a covariance matrix for use in the primary vertex fit.

Coulomb scattering in material between the interaction region and the innermost hit is included in this matrix.

Primary Vertex Fit

The primary event vertex is determined using a perigee fitting technique [52]. The perigee of a track is the point of closest approach to the nominal vertex point in the $r\phi$ plane. In the vertex fit tracks are considered as occupying regions in space defined by their track parameters and errors. A weighted mean of the perigee positions of the tracks can then be used to identify the actual primary vertex position of the event. The vertex fit has three stages:

1. Only tracks which reached superlayer 1 in the CTD and are consistent with production at the beamline are used.

2. A simple vertex fit is performed by calculating the weighted centre-of-gravity of the selected tracks. Tracks which contribute a large amount to the vertex χ^2 are removed from the fit, which is repeated until an acceptable χ^2 is reached.

3. The resulting primary vertex candidate is used in a full vertex fit which solves for the final vertex position then refits tracks, constraining them to the primary vertex.

Chapter 4

CTD Calibration

4.1 Introduction

In order to precisely reconstruct charged particle tracks, the CTD has to be accurately calibrated. In this chapter an iterative algorithm for calibrating the CTD $r-\phi$ system based on the least squares method is presented. The calibration constants are defined in section 4.2 and the method is explained in section 4.3. Monte Carlo test results proving the reliability of the method are presented in section 4.4. Results obtained from ZEUS data are given in section 4.5.

4.2 The Calibration Constants

When traversing the CTD a high energy charged particle loses energy by ionising the gas along its path. In any given cell, the ionisation drifts onto a sense wire inducing a signal which is recorded by the CTD readout electronics. The time taken by the ionisation to drift onto the sense wire, the drift time, is the only free variable used to reconstruct a 'hit', the position where ionisation occurred. Three calibration constants affect the position at which a hit is reconstructed.

Drift time is measured relative to the bunch crossing time defined by the HERA clock. The time for a signal to propagate through the CTD and its readout electronics before arriving at the FADC's is therefore included in the drift time.

In addition, if an e^+p collision occurs at a position other than the nominal ZEUS interaction point then a time offset is incurred in all drift time measurements. This naturally occurs because of the p bunch length, or, if the e^+p bunches do not cross in synchronisation with the HERA clock. To determine the true drift time, a time offset, t_0, in the measured drift time has therefore to be taken into account.

From the measured drift time, the drift distance μ_i of a hit can be calculated from the time-to-distance relationship

$$\mu_i = \int_0^{t_i} v(t)dt \tag{4.1}$$

where $v(t)$ is the drift velocity at a distance corresponding to drift time t_i from a sense wire. Using the Lorentz equation for motion of charged particles in electric and magnetic fields and assuming that the ionisation drift velocity, v_0, is constant, it can be shown that [53]

$$\mathbf{v}_0 = \frac{\mu}{1+\omega^2\tau^2}\left(\mathbf{E} + \frac{\mathbf{E}\times\mathbf{B}}{B}\,\omega\tau + \frac{(\mathbf{E}\cdot\mathbf{B})\cdot\mathbf{B}}{B^2}\,\omega^2\tau^2\right) \tag{4.2}$$

where $\omega = -\frac{e\mathbf{B}}{m}$, τ is the mean time between collisions of the ionisation and gas molecules, and $\mu = \frac{e\tau}{m}$ is the electron's mobility. For perpendicular electric and magnetic fields, $\mathbf{E} = (E_x, 0, 0)$ and $\mathbf{B} = (0, 0, B_z)$, as in the ZEUS CTD,

$$v_x = \mu E_x \tfrac{1}{1+\omega^2\tau^2}, \quad v_y = -\mu E_x \tfrac{\omega\tau}{1+\omega^2\tau^2}, \quad v_z = 0 \tag{4.3}$$

so that the drift velocity is,

$$v_0 = \mu E_x \frac{1}{\sqrt{1+\omega^2\tau^2}} \tag{4.4}$$

The calibration method assumes a constant drift velocity so the time-to-distance relationship is simply $\mu_i = v_0 t_i$.

Having calculated the drift distance, a hit's position can be fully reconstructed if the ionisation drift direction is known. From equation 4.3 it can be seen that the ionisation drifts at an angle θ_L with respect to the electric field such that

$\tan\theta_L = \omega\tau$. θ_L is known as the Lorentz Angle. Rearranging, to express θ_L in terms of the drift velocity and applied fields gives,

$$\tan\theta_L = \frac{v_o B}{E} \tag{4.5}$$

The reconstruction uses the planar drift approximation [54], in which ionisation drift is assumed to occur in a plane of negligible thickness, at the angle θ_L with respect to the negative electric field vector.

4.3 Calibration Method

The aim of the calibration method is to find the values of the calibration constants which produce tracks that best fit the hits in the CTD. This is performed by a least squares minimisation of the residuals, i.e. by minimising

$$S = \sum_{i=1}^{n} (\frac{\delta_i}{\sigma_i})^2 \tag{4.6}$$

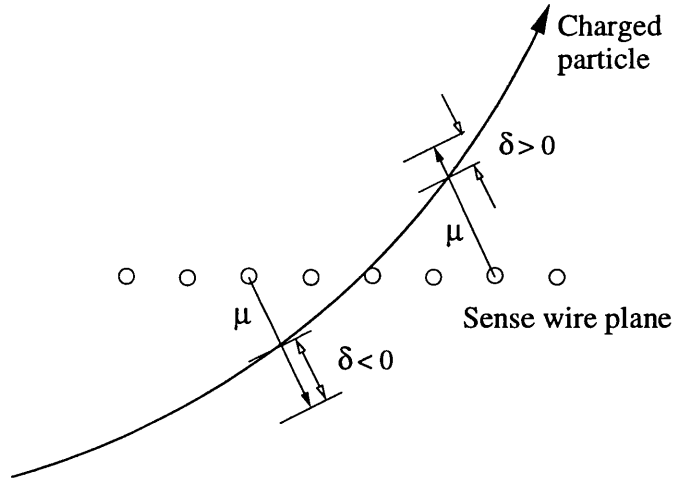

Figure 4.1: Definition of the residual.

The sum runs over hits associated with tracks. The residual, δ_i, as shown in figure 4.1, is the distance between the hit and the track reconstructed without that hit. Hits at azimuthal angles above(below) the sense wire plane are defined to have positive(negative) drift distances. This sign convention means hits at azimuthal angles above(below) tracks have positive(negative) residuals.

For small differences between the true calibration constants, ${t_0}^{true}$, ${v_0}^{true}$ and ${\theta_L}^{true}$, and the constants used in the hit reconstruction t_0', v_0', and θ_L' one can make a Taylor expansion of equation 4.6, giving,

$$S(t_0', v_0', \theta_L') = S(t_0, v_0, \theta_L) + \frac{\partial S}{\partial t_0}\delta t_0 + \frac{\partial S}{\partial v_0}\delta v_0 + \frac{\partial S}{\partial \theta_L}\delta\theta_L + \frac{1}{2}\left(\frac{\partial^2 S}{\partial t_0^2}\delta {t_0}^2 + 2\frac{\partial^2 S}{\partial t_0 \partial v_0}\delta t_0\, \delta v_0 + 2\frac{\partial^2 S}{\partial t_0 \partial \theta_L}\delta t_0\, \delta\theta_L + \ldots\right) \tag{4.7}$$

The best estimates of t_0 , v_0 and θ_L are given by minimising 4.6,

$$\frac{\partial S}{\partial t_0} = 0, \quad \frac{\partial S}{\partial v_0} = 0, \quad \frac{\partial S}{\partial \theta_L} = 0 \tag{4.8}$$

which is equivalent to solving for δt_0 , δv_0 and $\delta\theta_L$ in the equation,

$$\begin{pmatrix} \frac{\partial^2 S}{\partial t_0^2} & \frac{\partial^2 S}{\partial t_0 \partial v_0} & \frac{\partial^2 S}{\partial t_0 \partial \theta_L} \\ \frac{\partial^2 S}{\partial v_0 \partial t_0} & \frac{\partial^2 S}{\partial v_0^2} & \frac{\partial^2 S}{\partial v_0 \partial \theta_L} \\ \frac{\partial^2 S}{\partial \theta_L \partial t_0} & \frac{\partial^2 S}{\partial \theta_L \partial v_0} & \frac{\partial^2 S}{\partial \theta_L^2} \end{pmatrix} \begin{pmatrix} \delta t_0 \\ \delta v_0 \\ \delta\theta_L \end{pmatrix} = - \begin{pmatrix} \frac{\partial S}{\partial t_0} \\ \frac{\partial S}{\partial v_0} \\ \frac{\partial S}{\partial \theta_L} \end{pmatrix} \tag{4.9}$$

The residual is expected to have the form [54, 55],

$$\delta_i = v_0\delta t_0 + t_i\delta v_0 + |\mu_i| \cot\psi_i'\delta\theta_L \tag{4.10}$$

where

- t_i = drift time for the ith hit.
- μ_i = drift distance of the ith hit.
- ψ' = angle between nominal electron drift direction and track
- $\delta t_0 = t_0' - t_0^{true}$ = miscalibration of t_0
- $\delta v_0 = v_0' - v_0^{true}$ = miscalibration of v_0
- $\delta\theta_L = \theta_L' - \theta_L^{true}$ = miscalibration of θ_L

The first two terms represent the error in position caused by assuming a linear time-to-distance relation. The third term represents the error in the hit's

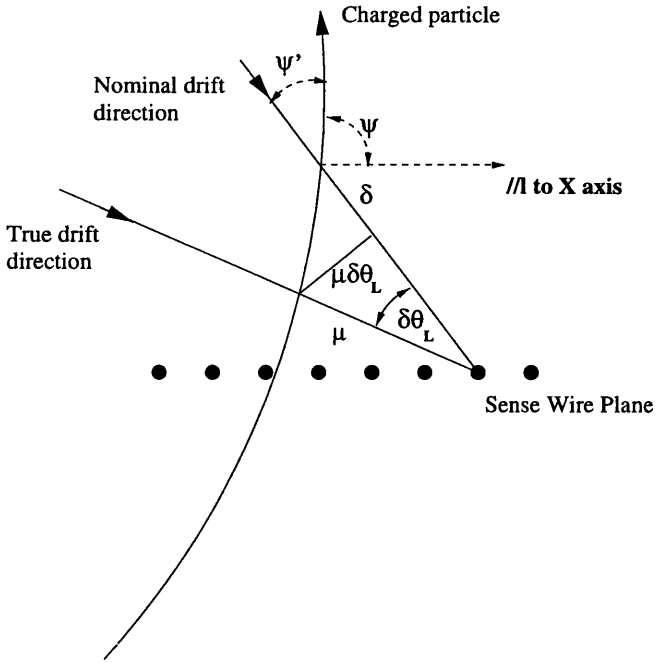

Figure 4.2: Contribution to the residual from a miscalibrated Lorentz angle.

position caused by reconstructing with the wrong drift direction as can be seen from Figure 4.2.

Differentiating 4.6 and 4.10 then substituting in 4.9 gives

$$\begin{pmatrix} \sum_{i=1}^{n}(\frac{v_0}{\sigma_i})^2 & \sum_{i=1}^{n}(\frac{v_0 t_i}{\sigma_i^2}) & \sum_{i=1}^{n}(\frac{v_0|\mu_i|\cot\psi_i'}{\sigma_i^2}) \\ \sum_{i=1}^{n}(\frac{v_0 t_i}{\sigma_i^2}) & \sum_{i=1}^{n}(\frac{t_i}{\sigma_i}^2) & \sum_{i=1}^{n}(\frac{t_i|\mu_i|\cot\psi_i'}{\sigma_i^2}) \\ \sum_{i=1}^{n}(\frac{v_0|\mu_i|\cot\psi_i'}{\sigma_i^2}) & \sum_{i=1}^{n}(\frac{t_i|\mu_i|\cot\psi_i'}{\sigma_i^2}) & \sum_{i=1}^{n}(\frac{|\mu_i|\cot\psi_i'}{\sigma_i})^2 \end{pmatrix} \begin{pmatrix} \delta t_0 \\ \delta v_0 \\ \delta\theta_L \end{pmatrix} = \begin{pmatrix} \sum_{i=1}^{n}(\frac{\delta_i v_0}{\sigma_i^2}) \\ \sum_{i=1}^{n}(\frac{\delta_i t_i}{\sigma_i^2}) \\ \sum_{i=1}^{n}(\frac{\delta_i|\mu_i|\cot\psi_i'}{\sigma_i^2}) \end{pmatrix} \quad (4.11)$$

or in matrix notation, $\mathbf{H}\delta\mathbf{a} = \mathbf{q}$

The matrix elements were evaluated by summing over hits associated with tracks. The track reconstruction gave all hits the same weight, σ_i. This is reasonable because to a first approximation, errors on hits will depend on the chamber properties rather than the hit itself. To avoid systematic effects which

influence the reconstructed hit positions, the following cuts were applied:-

- Track number of degrees of freedom > 30. This means only hits belonging to long, well measured tracks were used.
- As the expression used for the residual, equation 4.10 was not valid for stereo superlayer hits, only axial superlayer hits were used.
- $|\mu_i| > 0.8$cm and $\mu_{max} - |\mu_i| > 0.3$cm where μ_{max} is the maximum drift distance for the hit wire. These cuts limited hits to the uniform field region of a drift cell where the residuals were well understood [56].
- Only hits in the region $|\Delta z| < 50$cm and in the first 5 superlayers were used. The axial magnetic field is uniform to within 2% in this region [57].
- To avoid using badly reconstructed hits $|\delta_i| < 0.2$cm.
- Hits with only z-by-timing information were not used.

A polynomial correction function was used in the hit reconstruction to remove a systematic effect in the drift distance determination for hits on tracks with extreme ψ' values [56]. The corrected drift distance was used to evaluate a corrected drift time from $t_i = \mu_i/v_0$, with which the matrix elements were evaluated.

The calibration procedure was performed iteratively. Starting with either an uncalibrated sample of data events, or a sample of MC events, corrections to the calibration constants were determined. These were applied within the program which determined a new set of corrections. The error in each calibration constant was obtained from the corresponding entry on the main diagonal of $\mathbf{H^{-1}}$.

4.4 Monte Carlo Tests

The calibration method was tested using 1000 events each containing a single μ^- or μ^+, generated by the ZEUS detector simulation program, MOZART. The test

was to obtain the true values of the calibration constants when the reconstruction was started from incorrect values.

MOZART generated the events with the following calibration constant values.

$$t_0 = 0.0 \text{ dsp units}, \quad v_0 = 47 \ \mu\text{m/ns}, \quad \theta_L = 45^\circ \tag{4.12}$$

Since systematic effects were not modelled in the detector simulation the ψ' drift distance correction function was not applied in the hit reconstruction. However, the cuts listed in section 4.3 were applied, in order to provide a realistic test of the calibration procedure.

4.4.1 Null Test

The aim of this test is to prove the calibration procedure was not significantly biased towards any calibration constant values. The test was performed starting the track reconstruction with the true MOZART calibration constants. Figure 4.3 shows that no significant corrections to the calibration constants were found and the calibration was stable. Small systematic shifts in t_0 and θ_L were observed. The observed shift was $\Delta(t_0) = 0.1$ dsp units. Subsequent analysis [58] has shown this to be due to a spurious correlation between t_0 and $\tan\theta_L$. The systematic shift in $\tan\theta_L$ can be assigned to non-uniformity of the axial magnetic field. The magnetic field non-uniformity was at most $\frac{\Delta B_z}{B_z} \sim -2$ % corresponding to a variation in $\tan\theta_L$, $1 < \tan\theta_L < 1.02$. This meant the calibration method determined an average value of $\tan\theta_L$ over the volume of the CTD $|z| < 50$ cm, $r < 51$ cm. A small positive systematic shift of at most 2 % in the calculated $\tan\theta_L$ value is therefore expected. The observed shift was $\Delta(\tan\theta_L) = 0.013$.

4.4.2 t_0 Test

The results obtained calibrating from a wrong value of t_0 are shown in Figure 4.4. The initial value of t_0 was $t_0 = 2$ dsp units with v_0 and θ_L set at their true values. After two iterations the calibration constants were observed to have converged to the true values within error.

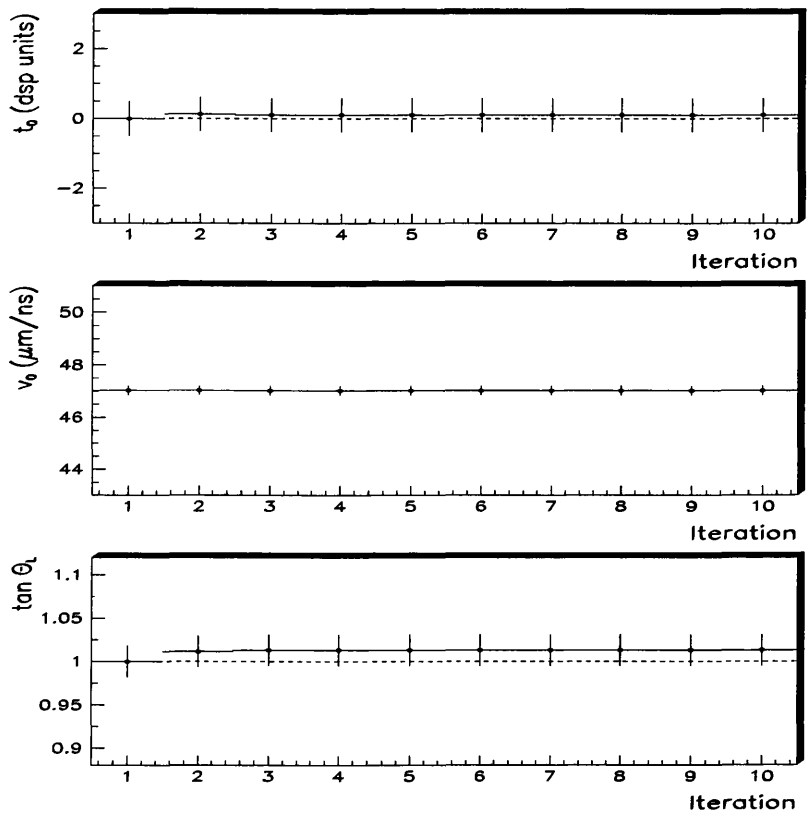

Figure 4.3: Calibration test using the true calibration constant values. No overall corrections to the calibration constants were calculated.

4.4.3 v_0 Test

The results obtained calibrating from a wrong value of v_0 are shown in Figure 4.5. The initial value of v_0 was $v_0 = 50$ μm/ns with t_0 and θ_L set at their true values. After two iterations the calibration constants were observed to have converged to the true values within error.

4.4.4 θ_L Test

The results obtained calibrating a wrong value of θ_L are shown in Figure 4.6. The initial value of θ_L was $\tan\theta_L = 1.05$ with t_0 and v_0 set at their true values. After one iteration the calibration procedure calculated $\tan\theta_L = 1.028 \pm 0.02$. No significant change was found at the next iteration, and it naïvely appeared

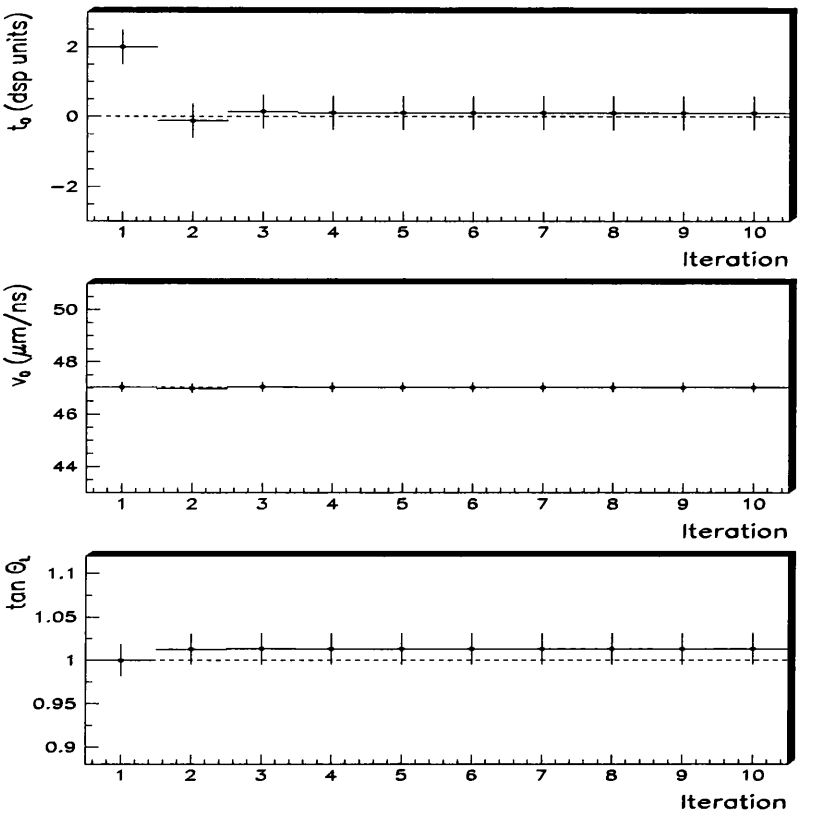

Figure 4.4: Calibration test with the initial calibration constant values $t_0 = 2.0$ dsp units, $v_0 = 47$ μm/ns, and $\tan\theta_L = 1.0$.

that the calibration method had failed this test. However, as explained in 4.4.1 the magnetic field non-uniformity means the calibration procedure actually determines a value of $\tan\theta_L$ averaged over the chamber volume. The value of $\tan\theta_L$ obtained in this test after one iteration is consistent with the average value obtained in 4.4.1.

4.4.5 Full Test

The results obtained when all the calibration constants were set at a wrong value are shown in Figure 4.7. The initial values of the calibration constants were

$$t_0 = -1.5 \text{ dsp units}, \quad v_0 = 50 \ \mu\text{m/ns}, \quad \tan\theta_L = 0.93 \tag{4.13}$$

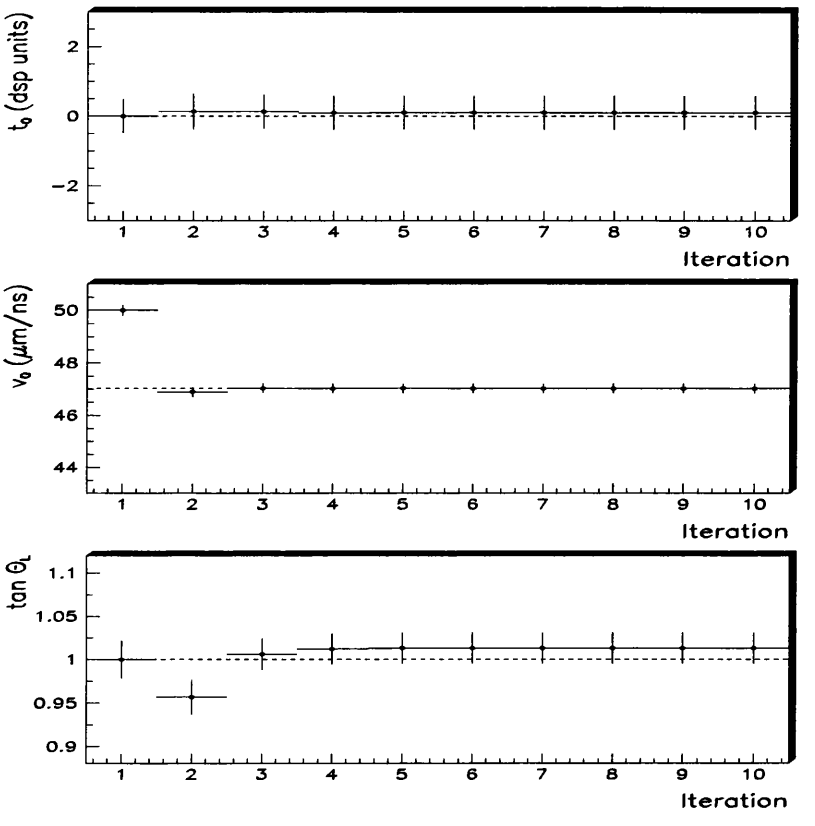

Figure 4.5: Calibration test with the initial calibration constant values $t_0 = 0.0$ dsp units, $v_0 = 50$ μm/ns, and $\tan\theta_L = 1.0$.

After two iterations the calibration constants were observed to have converged to the true values within error.

It is interesting to note in the calibration test shown in figure 4.7, t_0 and v_0 calibrated on the first iteration while θ_L calibrated on the second iteration. This is due to the fact that θ_L calibration is mostly affected by hits at large drift distances or extreme values of ψ'. Because the calibration constants used in the first iteration were very different from their true values many of these hits were either not reconstructed on tracks, or failed the drift distance selection cuts and were therefore not used by the calibration procedure. This can be seen in figure 4.8 where the number of recontructed hits passing the selection cuts and the mean drift distance of these hits are plotted against iteration. The number of reconstructed hits and the mean hit drift distance increase with each iteration

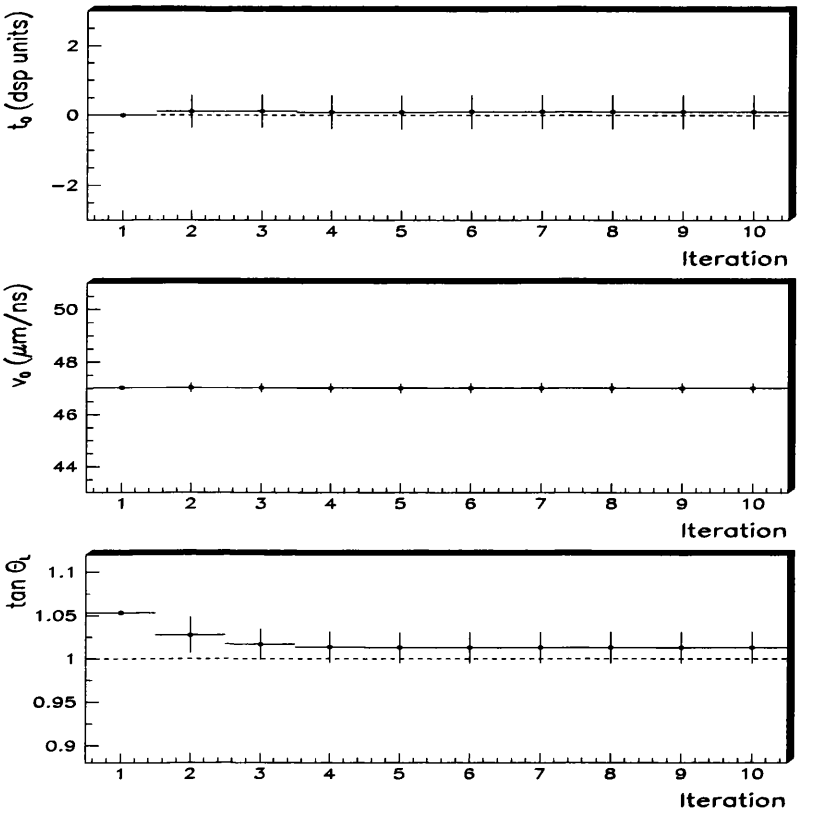

Figure 4.6: Calibration test with the initial calibration constant values $t_0 = 0.0$ dsp units, $v_0 = 47$ μm/ns, and $\tan\theta_L = 1.05$.

so that the hits necessary for calibrating θ_L were used.

4.4.6 Monte Carlo Test Conclusions

Taking into account systematic effects, no significant difference was observed between the values of the calibration constants used in the detector simulation and the calibration constants calculated by this calibration method.

4.5 Calibration of Data

The output from calibration of run 10020 is shown in Figure 4.9 The ψ' drift distance correction was applied. Hits used to determine the matrix elements were subject to identical cuts applied in the Monte Carlo tests. Only small changes in

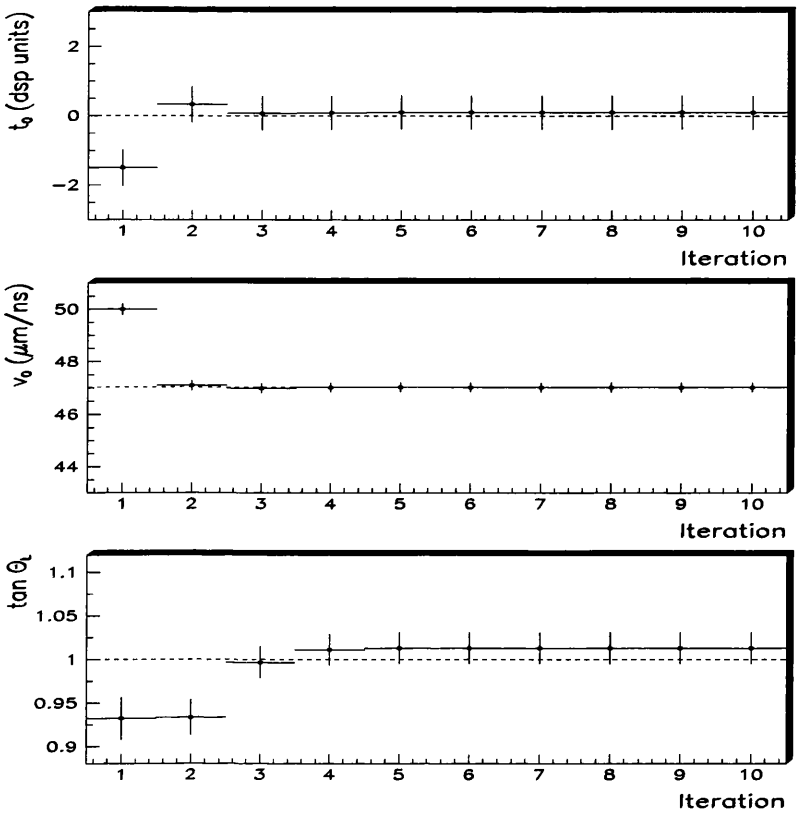

Figure 4.7: Calibration test with the initial calibration constant values $t_0 = -1.5$ dsp units, $v_0 = 50$ μm/ns, and $\tan\theta_L = 0.93$

the calibration constants relative to the default values were found.

The $r - \phi$ resolution, $\sigma_{r\phi}$, is plotted as a function of iteration in Figure 4.10. After the first iteration $\sigma_{r\phi}$ improved, then remained stable at 288 μm.

4.6 Conclusions

A global CTD calibration program based on the least-squares minimisation procedure has been developed. Tests on simulated data have proven the method reproduces the true calibration constants accurately. When applied to real data the calibration constants and $r - \phi$ resolution obtained were compatible with values obtained from the official calibration procedure.

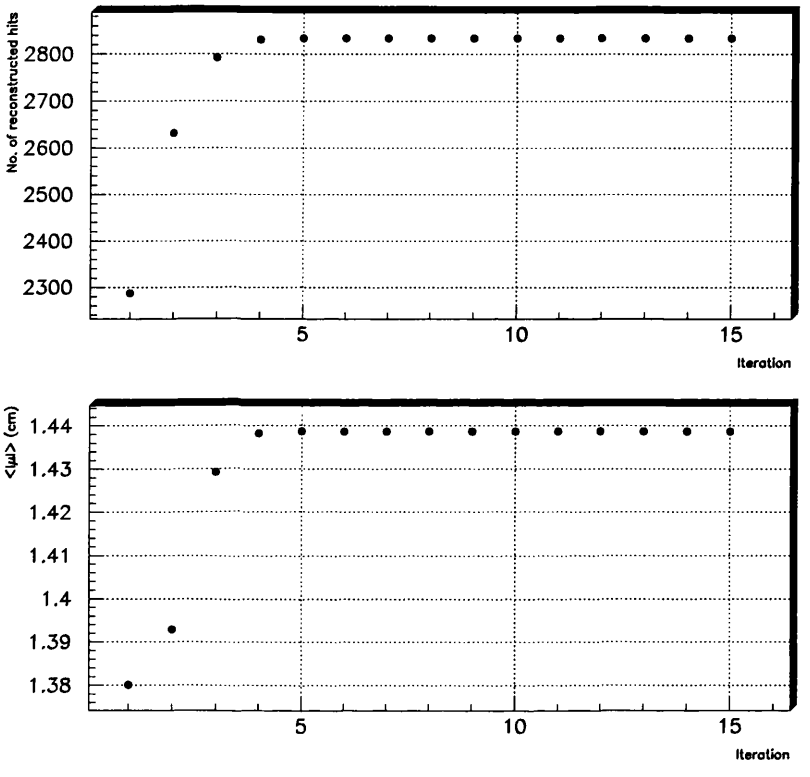

Figure 4.8: The number of hits passing the selection cuts, and mean magnitude of their drift distance as a function of iteration. The initial calibration constant values were $t_0 = -1.5$ dsp units, $v_0 = 50$ μm/ns, and $\tan\theta_L = 0.93$. After three iterations all hits which had failed the cuts due to using the wrong calibration constants had been recovered.

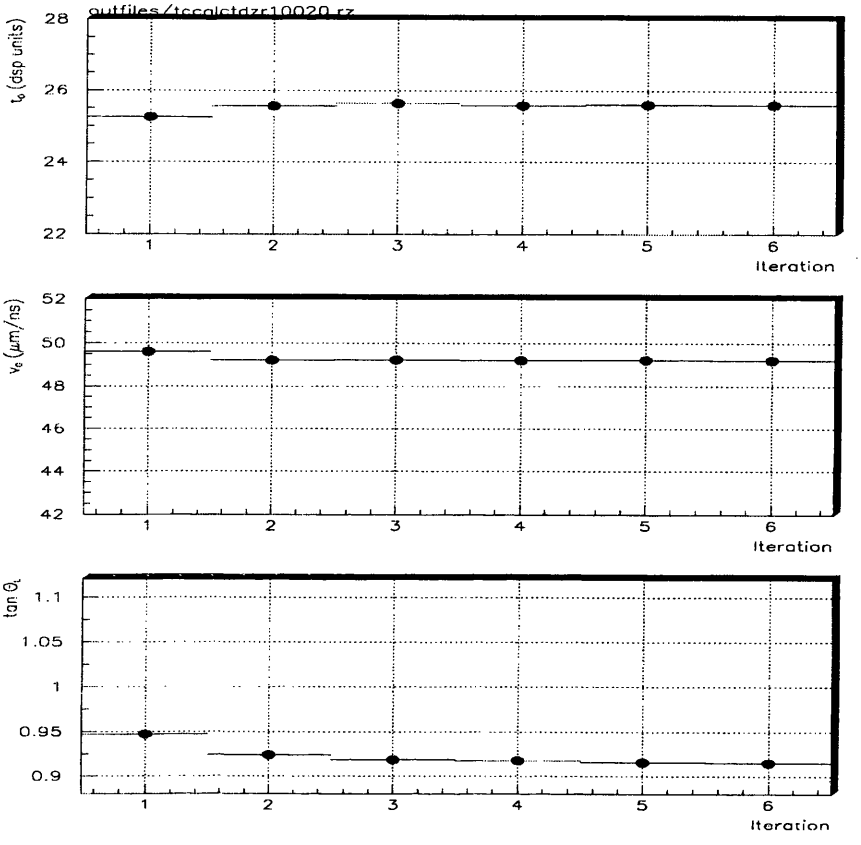

Figure 4.9: Calibration of data taken during run 10020. The only significant correction occurred at the first iteration.

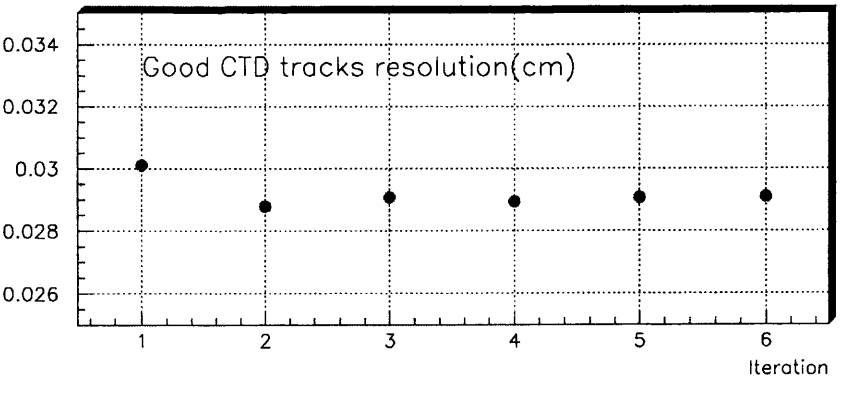

Figure 4.10: The resolution obtained for run 10020 as a function of iteration.

Chapter 5

Hard Photoproduction Event Selection

The method by which hard photoproduction events were selected from the 1994 data sample is described in this chapter. To ensure the selected events contain a hard interaction, events were required to contain a high E_T jet. The jet finding algorithm used is described in section 5.1. The kinematic region in which photoproduction events were selected is then defined in section 5.2. The trigger criteria and background rejection cuts used to select the sample of hard photoproduction events in the analysis are described in sections 5.3 to 5.6. The residual contamination from processes other than hard photoproduction is evaluated in section 5.7, and the PYTHIA Monte Carlo is shown to adequately describe general event properties in section 5.8

5.1 Jet Reconstruction

Jets were reconstructed using a standard ZEUS cone algorithm jet finder, EUCELL [59], which satisfies the Snowmass convention [60]. Cone algorithms reconstruct jets by searching for groups of particles or calorimeter energy deposits within a specified cone which have a transverse energy above a threshold value. EUCELL reconstructed jets either from energy deposits in the UCAL cells as

measured in ZEUS data or in events passed through the detector simulation, which will be referred to as UCAL jets, or from the four vectors of final state particles produced by the Monte Carlo simulation, which will be referred to as hadron level jets or hadron jets throughout this thesis. The jet finder operated in $\eta - \phi$ space so that its results were invariant with respect to a boost along the z-direction.

The procedure for reconstructing jets was the same for UCAL and hadron level jets:-

1. Starting at a high pseudorapidity value, $\eta_{max} = 3.5$ and going in the direction of decreasing η, preclusters of UCAL cells formed from arrays of 3 x 3 cells ('windows') with total transverse energy $E_T^{preclus} > E_T^{seed}$ were searched for in $\eta-\phi$ space. An E_T^{seed} value of 1 GeV was used in this analysis. To reduce effects of radioactive noise from the DU absorber material in the calorimeter cells with energies $E_{EMC} > 60$ MeV and $E_{HAC} > 110$ MeV in the EMC and HAC sections of the UCAL were used to form the preclusters. The initial jet direction was taken as $(\eta^{preclus}, \phi^{preclus})$ given by the cell at the precluster centre.

2. The total transverse energy deposited in UCAL cells within the radius

$$R = \sqrt{(\eta_i - \eta^{preclus})^2 + (\phi_i - \phi^{preclus})^2} = 1$$

was calculated according to

$$E_T^{cone} = \sum_i E_i \sin\theta_i \tag{5.1}$$

where E_i were the cell energies and η_i, ϕ_i and θ_i were the pseudorapidity, azimuthal and polar angles of cell centres with respect to the primary vertex coordinate.

3. The jet axis was evaluated from the cells within the cone radius according to

$$\eta^{cone} = \frac{\sum_i E_{Ti}\eta_i}{E_T^{cone}}$$

$$\phi^{cone} = \frac{\sum_i E_{Ti}\phi_i}{E_T^{cone}}$$

4. Stages 2 and 3 were repeated until the distance between the jet axes at each iteration, $\Delta R < 0.01$, or until 15 iterations had been performed.

5. If $E_T^{cone} > E_{T0}$ the UCAL cells formed a jet. A transverse energy threshold value $E_{T0} > 6$ GeV was used at the jet reconstruction stage in this analysis. The total jet energy and momentum components were then calculated from,

$$\begin{aligned} E^{cone} &= \textstyle\sum_i E_i, & P_x^{cone} &= \textstyle\sum_i E_i \cos\phi \sin\theta \\ P_y^{cone} &= \textstyle\sum_i E_i \sin\phi \sin\theta, & P_z^{cone} &= \textstyle\sum_i E_i \cos\theta \end{aligned} \tag{5.2}$$

   The reconstructed jets were therefore not massless.

6. Jets were reconstructed in order of decreasing E_T. During each scan of the window over the calorimeter, if a jet had a higher E_T than a previously reconstructed jet, the previous jet information was overwritten with the new reconstructed jet information. If the jet had lower E_T than other reconstructed jets its information was also saved, but could be overwritten at a later stage. The algorithm returned to stage 1, continuing from the next 3x3 array of cells.

7. After the window had scanned over all calorimeter cells in the pseudorapidity range $3.5 > \eta > -3$, cells contained in the reconstructed jet cone(s) were removed from the list of calorimeter cells to be used in jet reconstruction and the reconstructed jets were permanently stored. The algorithm returned to stage 1, and scanned through the calorimeter starting from η_{max}, looking for more jets. This loop was repeated until no more reconstructed jets above the E_T threshold were found.

5.2 Definition of Kinematic Region

The choice of kinematic region from which hard photoproduction events are selected for this analysis is motivated by previous studies on hard photoproduction

data selection [61] and the ZEUS inclusive jet measurement [21, 62]. For the analysis presented in this thesis, particle production is studied in events with jets of

$$E_T^{HAD} \geq 8 \text{ GeV and } |\eta^{HAD}| \leq 0.5 \tag{5.3}$$

in the kinematical region

$$0.2 \leq y \leq 0.85 \text{ and } Q^2 < 4 \text{ GeV}^2 \tag{5.4}$$

where E_T^{HAD} and η^{HAD} refer to jets reconstructed at the final state hadron level in the Monte Carlo. The hadron jet and kinematic selection criteria define a region which is largely free from non-photoproduction background processes and where the acceptance and purity correction factors determined in [21] were not large.

To select events measured in the ZEUS detector which correspond closely to the kinematic region defined by equations 5.3 and 5.4 the response of the UCAL was studied with a sample of resolved and direct PYTHIA events. Figures 5.1 and 5.2 show the E_T and η resolution of 'matching' UCAL and hadron level jets. Hadron level and UCAL jets were considered to be matching if,

$$\Delta R = \sqrt{(\eta^{UCAL} - \eta^{HAD})^2 + (\phi^{UCAL} - \phi^{HAD})^2} < 1 \tag{5.5}$$

where η^{UCAL}, ϕ^{UCAL} and η^{HAD}, ϕ^{HAD} were the UCAL and hadron level jet axes respectively. When two reconstructed jets satisfied the above criterion the UCAL jet closest to the hadron level jet was chosen. For both direct and resolved events a systematic shift of -13 % is observed in E_T^{UCAL} with respect to E_T^{HAD} in figure 5.1. This was observed in [21], and is due to several effects, such as, energy losses of particles in dead material before interacting in the UCAL and low p_T particles failing to reach the UCAL surface because of the effect of the magnetic field on their trajectory. No significant shift is observed in η^{UCAL} with respect to η^{HAD} in figure 5.2. So to take account of the 13 % difference between the energy scales of hadron level and reconstructed jets, inclusive jet events with at least one UCAL jet satisfying

$$E_T^{UCAL} \geq 7 \text{ GeV in } |\eta^{UCAL}| \leq 0.5 \tag{5.6}$$

were used in this analysis.

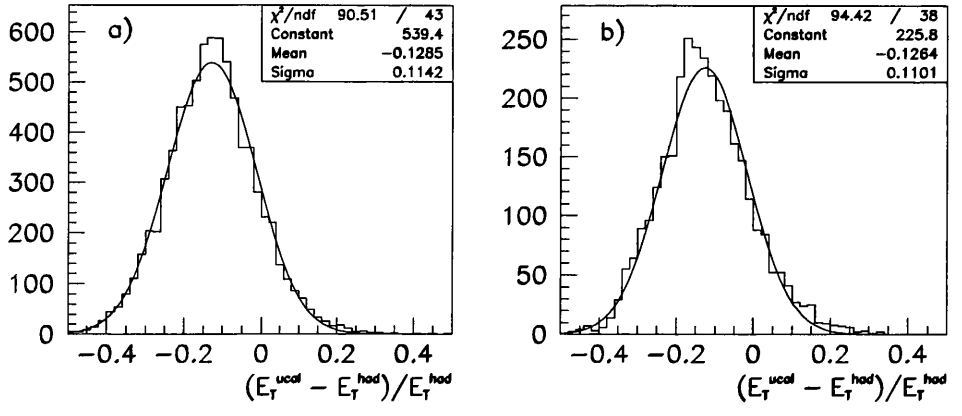

Figure 5.1: E_T^{UCAL} resolution in direct events (a) and resolved events (b).

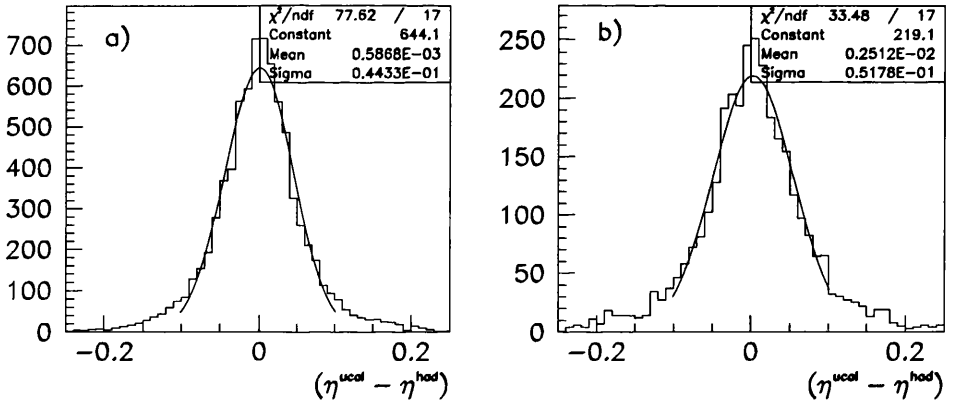

Figure 5.2: η^{UCAL} resolution in direct events (a) and resolved events (b).

The measurement of y was also observed to suffer from the effects of particle energy loss in dead material in front of the calorimeter in [21, 63]. Figure 5.3 shows the resolution of y_{JB}, when compared to y_{LUMI} and also the resolution in y_{JB} vs. y_{LUMI} in the data sample selected in this chapter. y_{JB} was calculated from the reconstructed UCAL cell energy deposits (including any DIS e^+ candidates) and

y_{LUMI} from the energy of the scattered e^+ in the LUMI EDET. y_{LUMI} was shown to measure accurately the true value of y in [21, 63]. The mean reconstructed value of y_{JB} is observed to be 20 % lower than y_{LUMI}. The deviation from linearity at low y_{LUMI} is a result of a trigger threshold described in the next section, while at high y_{LUMI} it is a result of particle losses down the rear beampipe. To a good approximation, hard photoproduction events from the kinematic region corresponding to equation 5.4 were selected by requiring,

$$0.15 \leq y_{JB} \leq 0.7 \tag{5.7}$$

It will be shown in section 5.7.2 that this cut also reduces the number of DIS events selected in the data to a negligible fraction.

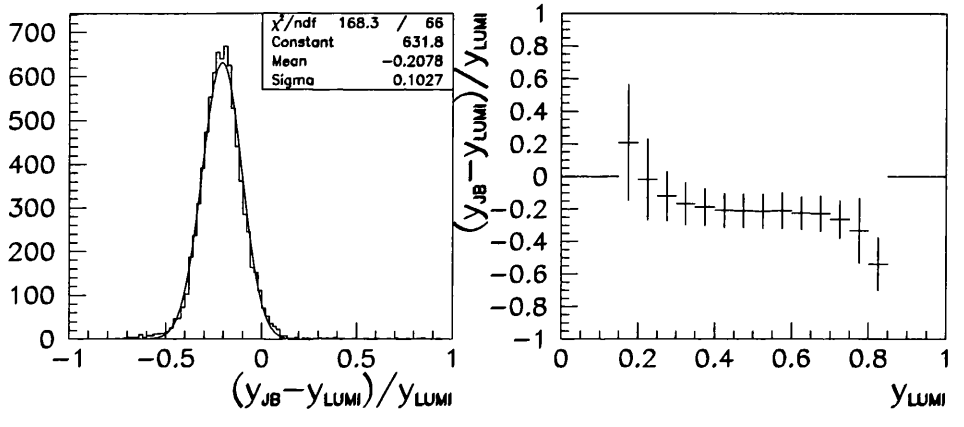

Figure 5.3: Resolution of y_{JB} with respect to y_{LUMI} (left) and resolution of y_{JB} as a function of y_{LUMI}.

5.3 Trigger

Events were required to satisfy the following trigger slots/branches.

- FLT CALgTRK94. This is an .OR. of five FLT slots in coincidence with a CTD z-by-timing track pointing to the nominal vertex. The five

contributing FLT slots placed conditions on global or regional energy sums which are given in table 5.1. The beam-gas background rate is reduced in three of the FLT slots by excluding the ring of calorimeter cells closest to the beampipe. High trigger thresholds are set so that photoproduction events which contain a hard scattering are selected from the majority of soft photoproduction events. Events with a timing signal in the VETOWALL, C5, or SRTD consistent with p beam induced background events were rejected.

- SLT High Et. Events were required to satisfy $E - p_z > 12$ GeV and $p_z/E < 0.95$, where $E = \sum_i E_i$ is the sum of calorimeter cell energies and $p_z = \sum_i E_i cos\theta_i$ is the total longitudinal momentum, θ_i being evaluated at the centre of each cell with respect to the nominal interaction point as tracking information was not available at the SLT in 1994. Both sums exclude cells within 10° of the FCAL beampipe hole.

- TLT One or Dijet. The TLT selected events with jets identified using a modified version of the cone jet finder described in section 5.1. The jet finder was modified to increase its speed; it sought any jet above threshold and did not perform the iterative stages. The one jet branch required at least one jet satisfying $E_T > 6.5$ GeV.AND.$2 < \eta^{JET} < 2.5$ .OR. $E_T > 5.5$ GeV.AND.$\eta^{JET} < 2$. The dijet branch required two or more jets each satisfying either $E_T > 4.0$ GeV.AND.$2 < \eta^{JET} < 2.5$ .OR. $E_T > 3.5$ GeV.AND.$\eta^{JET} < 2$.

- DST One or Dijet. In addition to the above criteria the DST filter required the calorimeter timing to satisfy $t_r > -6$ ns, $t_f - t_r < 6$ ns and that the event had a primary vertex with $|14t_f + z_{vtx}| < 60$ cm.

Trigger	Meaning	Threshold (MeV)
CAL_E	Total calorimeter energy	14968
EMC_E	EMC energy excluding forward beampipe region	10068
Et	Transverse energy excluding forward beampipe region	11574
BEMC_E	BCAL EMC energy	3404
REMC_E	RCAL EMC energy excluding rear beampipe region	2032

Table 5.1: FLT triggers, and energy thresholds contributing to the FLTgTRK94 slot.

5.4 Preliminary Event Sample

Events were selected from a data sample with an integrated luminosity of 2.65 pb^{-1}. 648156 events satisfied the trigger and filter criteria. Requiring at least one jet to satisfy the criteria of section 5.1 reduced this sample to 51739 events. Of these, 8549 events contained a e^+ with $E > 5$ GeV in the LUMI EDET monitor. In the following sections these events will be referred to as the LUMI tagged sample.

5.5 Detector Operation

In addition to the cuts outlined below, events were required to pass the EVTAKE routine. EVTAKE required that:

- the CTD high voltage was fully on and there were no large dead regions in the CTD;
- the solenoid magnet was on;
- the calorimeter was operating, and did not contain a large number of neighbouring dead cells; and,
- the luminosity monitor was on.

5.6 Background Rejection

Under the assumption that LUMI tagged events constituted a background free sample of e^+p physics events, background rejection cuts were established by comparing distributions of quantities in the inclusive jet sample and the LUMI tagged sample. The cuts are listed in this section in the same order as they were applied in the analysis.

5.6.1 Radiative Event Rejection

Radiative photoproduction events were removed by requiring less than 2 GeV energy deposited in the LUMI GDET.

5.6.2 Primary Vertex Position

The primary vertex z_{vtx} coordinate distribution for the inclusive jet and LUMI tagged samples are shown in figure 5.4. Vertices were required to be well reconstructed with $\chi^2/ndf < 10$. Both event samples have a similar Gaussian shape in the region $-30 < z_{vtx} < 30$ cm. The tails above and below this region can be attributed to p beam gas interactions by comparing with the distribution from p pilot bunches. The LUMI tagged sample was well fit by a Gaussian with mean $< z >= 3.5$ cm and standard deviation, $\sigma_z = 10.4$ cm. Events were required to satisfy a $4\sigma_z$ cut on the primary vertex z-coordinate:

$$-37 \leq z \leq 45 \text{ cm} \tag{5.8}$$

5.6.3 Proton Beam Gas Rejection

Events originating from proton beam gas interactions produce many high momentum tracks in the proton direction associated with a primary vertex upstream of the detector. The number of well measured tracks attributable to an upstream p

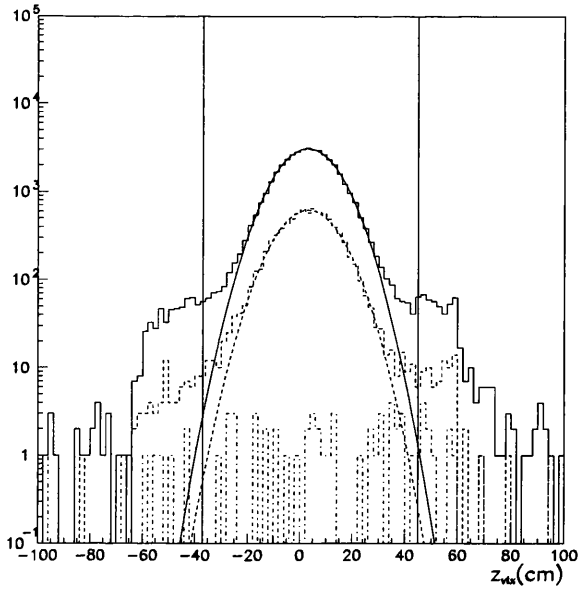

Figure 5.4: Primary vertex distributions for all events (solid histogram) and for LUMI tagged events (dashed histogram). The results of Gaussian fits to the central range of the distributions and limits of the z_{vtx} selection cut are also shown.

beam background event, n_{bad}, was defined as the number of tracks satisfying

$$\begin{aligned} &p_T > 0.15 \text{ GeV}, \quad 5° \leq \theta \leq 70°, \quad z_{helix} \leq -75 \text{ cm} \\ &ndf \geq 20, \qquad\quad n_{ax} > 5, \qquad\quad n_{ste} > 5 \end{aligned} \tag{5.9}$$

where z_{helix} is the z-coordinate of the point of closest approach of the track to the z-axis, and n_{ax} and n_{ste} are the number of axial and stereo layer hits on the track, respectively.

Figure 5.5 shows the n_{bad} distributions for the inclusive jet and LUMI tagged event samples. Both samples show a peak at low values of n_{bad}, however there is a tail in the inclusive jet sample, not present in the LUMI tagged sample. The n_{bad} distribution for events originating from p pilot bunches is also shown in figure 5.5 and is similar in shape to the inclusive jet sample at $n_{bad} > 4$. The tail in the inclusive jet sample is therefore attributable to p beam gas events. An event was accepted if it satisfied,

$$n_{bad} < 4 \tag{5.10}$$

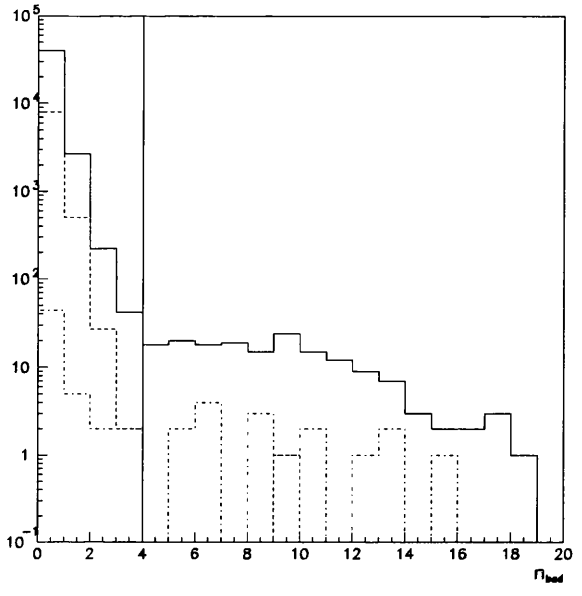

Figure 5.5: The number of bad tracks in all events (solid histogram), LUMI tagged (dashed histogram), and unpaired p bunch events (dash dotted histogram). The vertical line at $n_{bad} = 4$ denotes the upper limit of the event selection cut.

5.6.4 DIS Event Rejection

To limit the event sample to photoproduction interactions, DIS events were rejected by anti-tagging scattered positrons. Scattered e^+ candidates were identified in the UCAL by the difference in their shower shape from muons and hadrons by a standard ZEUS electron finder, ELEC5 [64]. Figure 5.6 shows a plot of y_{JB} vs. y_e for events containing a e^+ candidate. In this analysis y_{JB} was calculated from a sum over all particles in an event, and so included any e^+ candidate. This is different from DIS analyses where the sum does not include the e^+ candidate. Events are observed to particularly populate two regions in figure 5.6(a).

- A band at high y_e extending over the range of y_{JB} values. This arises from photoproduction events where a 'positron' has been found. These positrons usually arise from misidentified π^0 decays, from low energy $\pi^\pm$ showers or from semi-leptonic decays. Since they usually have low energy, y_e has a

high value.

- A cluster of events at $y_{JB} > 0.7$ and low y_e due to DIS. Energy and momentum conservation gives $y_{JB} = 1$ for a fully contained, perfectly reconstructed DIS event, but the finite calorimeter energy resolution, energy losses of particles in dead material before the calorimeter and particle losses down the beampipe degrade the y_{JB} measurement.

A plot of y_{JB} vs. y_e is shown for events where a scattered e^+ is found in the LUMI EDET in figure 5.6(b). The LUMI tagged events populate the high y_e region with very few events in the region $y_{JB} > 0.7$.

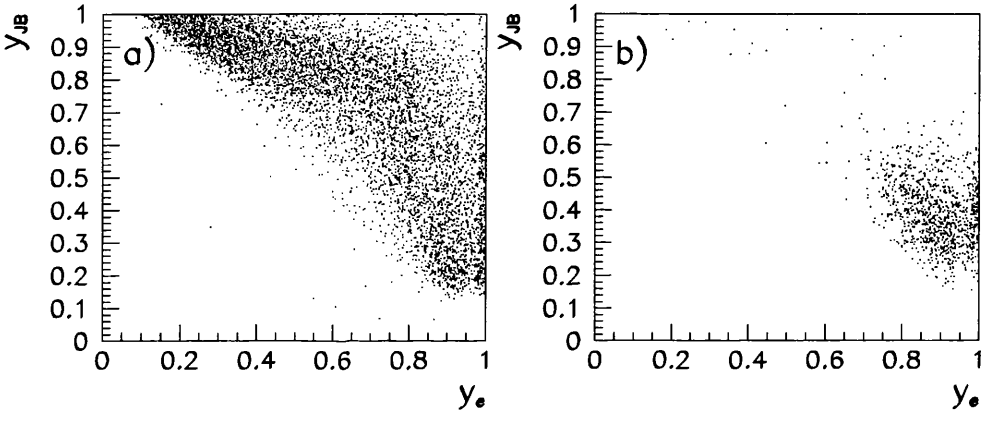

Figure 5.6: Correlation plots of y_{JB} vs. y_e for all events (a) and LUMI tagged events (b), containing a e^+ reconstructed in the UCAL.

Figure 5.7 shows a plot of y_e for events containing a scattered positron with $E_{e+} > 5$ GeV. The distribution from the inclusive jet sample extends over the full range of y_e, while the LUMI tagged sample does not extend below $y_e \sim 0.7$.

DIS events were therefore removed by rejecting events containing a scattered positron with

$$E_{e+} > 5 \text{ GeV and } y_e < 0.7 \tag{5.11}$$

and by also requiring

$$y_{JB} \leq 0.7 \tag{5.12}$$

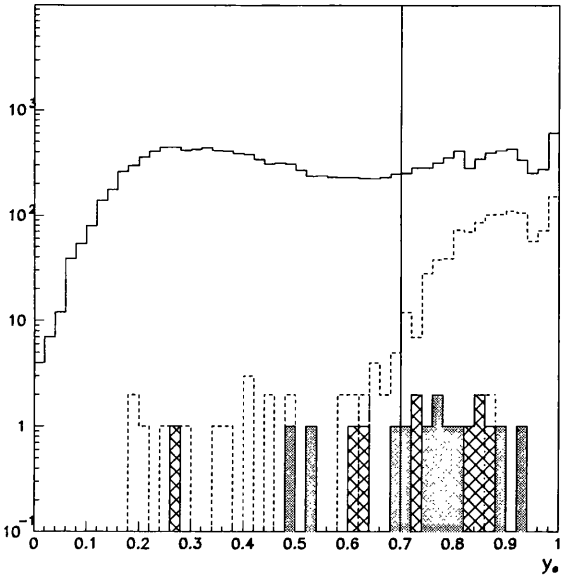

Figure 5.7: y_e distribution for all events with a scattered e^+ candidate (solid histogram), LUMI tagged events (dashed histogram), unpaired p bunches (dash-dotted histogram), unpaired e^+ bunches (cross-hatched histogram) and empty buckets (shaded histogram). The event selection cut at $y_e = 0.7$ is shown as the vertical line.

As explained in section 5.2 events were also required to satisfy

$$y_{JB} \geq 0.15 \tag{5.13}$$

This cut also had the benefit of removing a kinematic region where contamination from p beam induced background events was originally high [61]. However, as can be seen in figure 5.8 there are very few events with a low y_{JB} due to the $E - P_z$ and p_z/E cuts at the SLT.

5.6.5 Charged Current and Cosmic Ray Rejection

Cosmic and charged current events were rejected using a missing p_T cut. Missing transverse momentum was calculated from $p\!\!\!/_T = \sqrt{(\sum_i p_{x_i})^2 + (\sum p_{y_i})^2}$ where the sum is over all calorimeter cells, and angles were evaluated at the cell centres. Figure 5.9 shows the distribution of $\frac{p\!\!\!/_T}{\sqrt{E_T}}$ for the inclusive jet and LUMI tagged samples. Both samples are peaked at low $\frac{p\!\!\!/_T}{\sqrt{E_T}}$. The inclusive jet sample exhibits

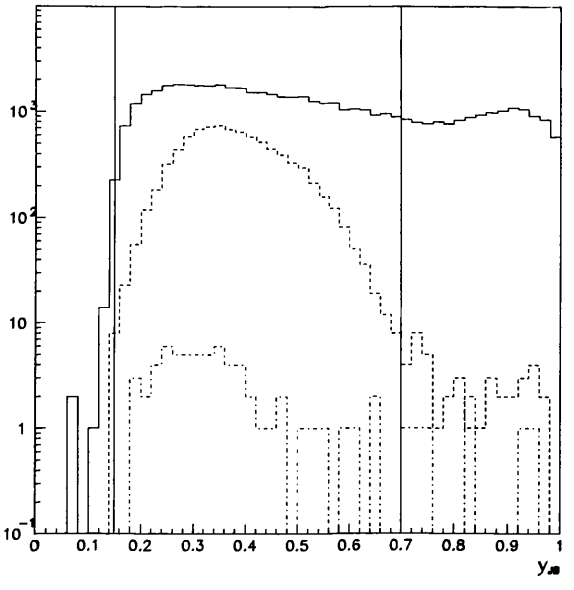

Figure 5.8: y_{JB} distribution for all events (solid histogram), LUMI tagged events (dashed histogram) and unpaired p bunches (dash-dotted histogram). The event selection range lies between the two vertical lines.

a shoulder at higher values of $\frac{p\!\!\!/_T}{\sqrt{E_T}}$ not present in the LUMI tagged sample. Figure 5.9 also shows the $\frac{p\!\!\!/_T}{\sqrt{E_T}}$ distribution for events triggered in coincidence with an empty bucket crossing which has a similar shape to the inclusive jet distribution at high values of $\frac{p\!\!\!/_T}{\sqrt{E_T}}$. Cosmic ray and charged current events were removed from the data sample by requiring,

$$\frac{p\!\!\!/_T}{\sqrt{E_T}} \leq 2 \text{ GeV}^{1/2} \tag{5.14}$$

The UCAL timing accuracy of $\sim$ 1 ns allows discrimination of real physics events from background events. Cosmic ray event rejection was enhanced by applying a cut on the average time of signals in the upper and lower halves of the UCAL. Figure 5.10 shows a plot of $t_u - t_d$ for events with well defined average time measurements in the upper and lower halves of the calorimeter. Both the inclusive jet and LUMI tagged samples peak at $t_u - t_d \sim 0$, but the inclusive jet sample also contains events at $t_u - t_d < -6$ ns not present in the LUMI tagged sample. Also shown in figure 5.10 is the $t_u - t_d$ distribution for events

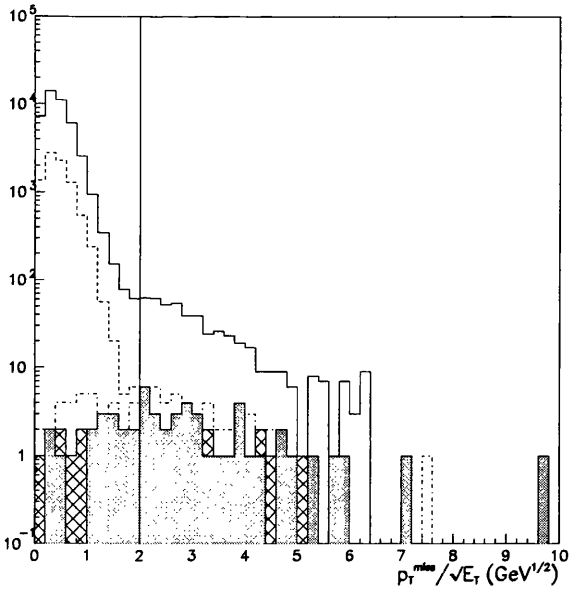

Figure 5.9: Missing transverse momentum distribution for all events (solid histogram), LUMI tagged events (dashed histogram), unpaired p bunches (dash-dotted histogram), unpaired e^+ bunches (cross-hatched histogram) and empty buckets (shaded histogram).

triggered in coincidence with an empty bunch crossing. These events have a similar distribution to the inclusive jet sample at low values of $t_u - t_d$. Cosmic ray events were therefore further rejected by requiring,

$$t_u - t_d \geq -6 \text{ ns} \tag{5.15}$$

5.6.6 Diffractive Event Rejection

DIS Events containing little energy flow in the region near the FCAL beampipe were reported in [65]. These diffractive events were interpreted as interactions in which the structure of a colourless object emitted by the proton was being probed instead of the proton. Events of this nature were identified from the pseudorapidity distribution of the most forward energy deposit η_{max}. The η_{max} distribution for energy deposits with $E_T > 400$ MeV in the selected sample of hard photoproduction events is shown in figure 5.11 and is observed to show an excess of events at $\eta_{max} < 1.5$ compared to the mixed resolved and direct

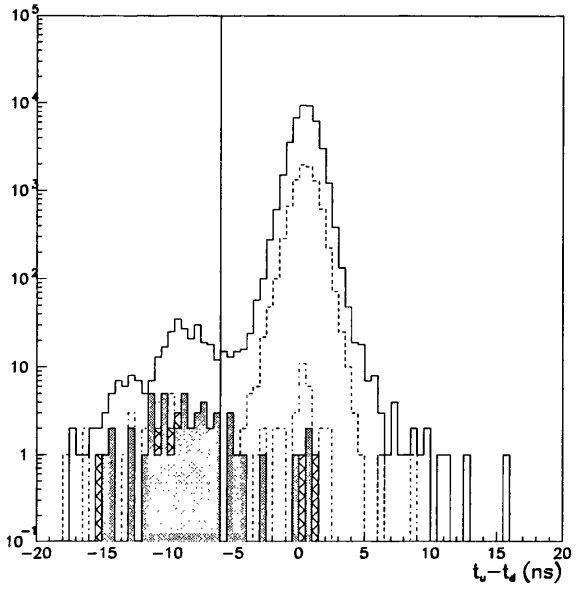

Figure 5.10: $t_u - t_d$ distribution for all events (solid histogram), LUMI tagged events (dashed histogram), unpaired p bunches (dash-dotted histogram), unpaired e^+ bunches (cross-hatched histogram) and empty buckets (shaded histogram). The event selection cut at $t_u - t_d = -6$ ns is shown as the vertical line.

η_{max} distribution from PYTHIA. Diffractive events were removed from the hard photoproduction event sample by requiring,

$$\eta_{max} \geq 1.5 \tag{5.16}$$

5.7 Selected Event Sample

Applying the above cuts to events satisfying the trigger criteria gave a sample of 35695 hard photoproduction inclusive jet events, of which 8309 were LUMI tagged. The number of events passing each stage of the event selection are given in table 5.2.

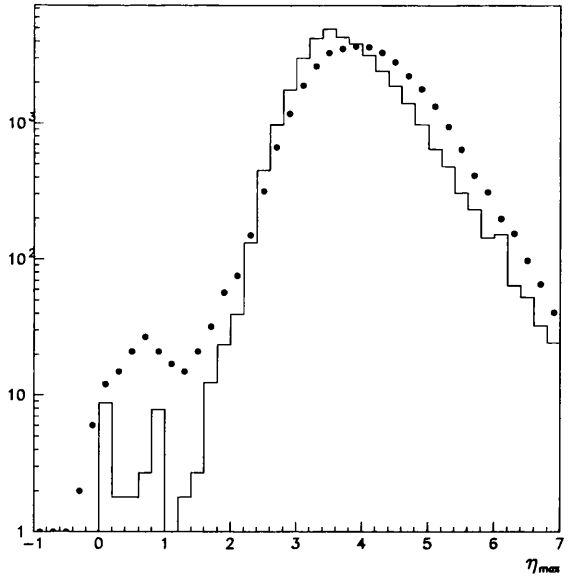

Figure 5.11: Pseudorapidity distribution of the most forward energy deposit with $E_T >$ 400 MeV for data (dots) and PYTHIA resolved plus direct Monte Carlo (solid histogram).

5.7.1 Non *ep* Physics Contamination

Of the inclusive jet events, 5 were from unpaired p bunches, 2 were from unpaired e^+ bunches, and 4 were from empty bunch crossings. The background contamination from e-gas, cosmics and charged current events was therefore estimated to be < 0.1 %, and 0.17 % for p-gas events, and was neglected in the analysis.

5.7.2 DIS Contamination

The e^+ anti-tag cut employed, limits the selected event sample to the region $Q^2 < 4$ GeV^2. This is shown in figure 5.12. A sample of 59913 HERACLES + ARIADNE DIS Monte Carlo events with $Q^2 > 1.8$ GeV^2 were passed through the full detector simulation and were subjected to the trigger and event selection criteria above. The Q^2 distribution of this Monte Carlo sample before and after all selection criteria were applied is shown in figure 5.12. From 25369 events with $Q^2 > 4$ GeV^2, 4 passed the trigger and event selection criteria. This

Event Selection Cut	Events Selected	
Trigger and filter	648156	
$E_\gamma < 2$ GeV	620541	(101101)
$E_T > 7$ GeV, $\|\eta\| < 0.5$	51739	(8549)
$-37 < z < 45$ cm	50473	(8402)
$n_{bad} < 3$	50362	(8402)
$0.15 < y_{JB} < 0.7$	36637	(8358)
Reject $E_e > 5$ GeV, $y_e < 0.7$	36239	(8346)
$\frac{p\!\!\!/_T}{\sqrt{E_T}} \leq 2$ GeV$^{1/2}$	35896	(8340)
$t_u - t_d > -6$ ns	35843	(8338)
$\eta_{max} > 1.5$	35695	(8309)

Table 5.2: The number of events passing each stage of the event selection cuts. The cuts are listed in the order they were applied in the analysis. Numbers in brackets correspond to the LUMI tagged sample.

demonstrates that the criteria above have selected an essentially pure sample of photoproduction events with $Q^2 < 4$ GeV^2.

The residual contamination from DIS events with $Q^2 > 4$ GeV^2 was estimated using a sample of 192081 $Q^2 > 4$ GeV^2 HERACLES + ARIADNE DIS Monte Carlo events. A total of 62 events passed the event selection cuts. The luminosity of the Monte Carlo sample was 444 nb^{-1}, therefore one expects approximately 310 DIS events in the hard photoproduction sample amounting to 0.9 % of the inclusive jet event sample.

5.7.3 Diffractive Contamination

The cross section for jet production in diffractive hard photoproduction events with $0.2 < y < 0.85$, $E_T^{JET} > 8$ GeV and $|\eta^{JET}| < 1$ for different values of η_{max} was reported in [66]. For $1.5 < \eta_{max} < 2.4$ the cross section is 156.3 pb, equivalent to 414 jets in the hard photoproduction sample selected in this analysis. Assuming

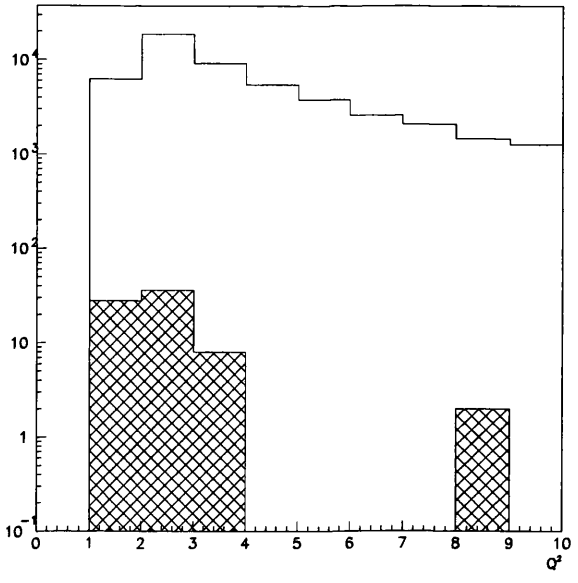

Figure 5.12: The Q^2 distribution of the HERACLES + ARIADNE DIS Monte Carlo sample with $Q^2 > 1.8$ GeV^2 is shown as the solid histogram. The Q^2 distribution of events from this sample passing the combined trigger and event selection criteria is shown as the cross-hatched histogram.

all diffractive events contain just one reconstructed jet, the contamination in the selected hard photoproduction sample from diffractive processes is 1.2 %. This is an upper limit due to the above assumption and also since the η region of the measured jet cross section is $|\eta^{JET}| < 1$, whereas the selected hard photoproduction event sample used in this analysis satisfies $|\eta^{JET}| < 0.5$

5.8 Comparison of Inclusive Jet Data with Monte Carlo Simulation

Distributions of reconstructed variables in the hard photoproduction data sample and mixed resolved and direct Monte Carlo sample are compared in figure 5.13. There is good agreement in all the distributions, except for the large η region of the η^{JET} distribution. This is in agreement with the excess of the jet cross section in data over Monte Carlo observed in [21]

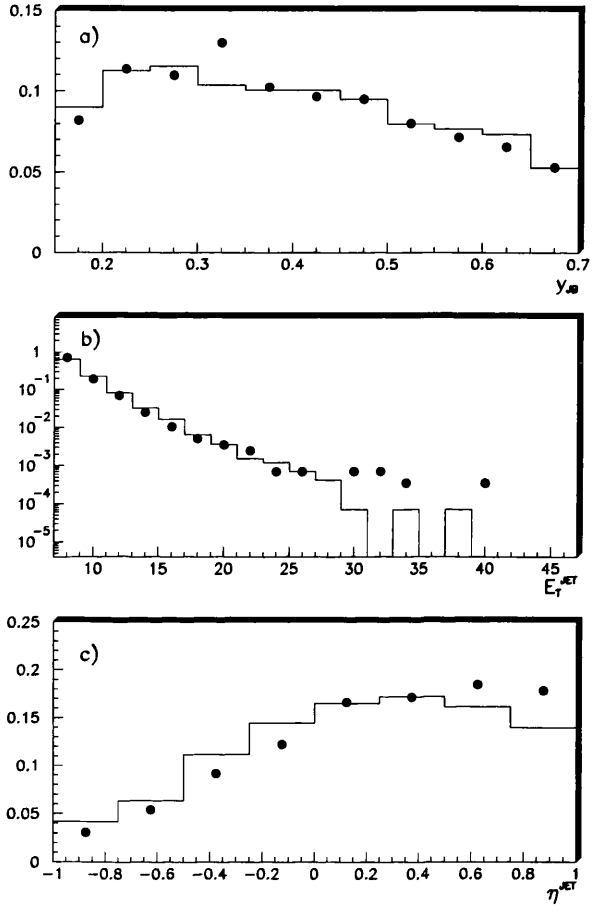

Figure 5.13: Comparison of reconstructed variables in selected events in DATA (filled circles) and mixed resolved + direct MC (solid histogram).

Chapter 6

K^0 Analysis

In this chapter the method used and cuts applied to identify K_s^0 are described and the accuracy of the K_s^0 reconstruction method is established. The properties of reconstructed K_s^0 in the PYTHIA Monte Carlo sample are shown to reproduce adequately the distributions of reconstructed K_s^0 in data events selected using the criteria of section 5, and the efficiency of the K_s^0 reconstruction procedure is determined from the Monte Carlo sample. Corrected K_s^0 p_T, η spectra, multiplicities per jet, and fragmentation functions in hard photoproduction events are derived and systematic errors in each of the distributions are calculated.

6.1 K_s^0 Reconstruction

K_s^0 were identified by their charged decay mode $K_s^0 \rightarrow \pi^+\pi^-$. This decay mode is easily identifiable since K_s^0 decay via the weak interaction, with a lifetime $\tau \sim 10^{-10}$ s, so that in many cases their decay vertices are spatially separated from the primary event vertex.

In addition to reconstructing K_s^0 mesons, Λ particles were identified by their decay $\Lambda \rightarrow p\pi$. An analysis of Λ production was not made. Instead, Λ candidates were removed from the reconstructed K_s^0 sample in order to enable better determination of the combinatoric background in the K_s^0 signal.

A general outline of the reconstruction algorithm is given here. For details of

the algorithm see appendix A. The reconstruction starts by pairing oppositely charged tracks. Conditions were placed on the track transverse momentum, $p_T > 150$ MeV and pseudorapidity, $|\eta| < 1.75$ since these tracks were known to be well reconstructed by the tracking detectors and offline reconstruction code. Particle tracks were assumed to be circular in the transverse plane, since most K_s^0 decays occurred in the central region of the ZEUS tracking detectors. As already discussed in chapter 4 the magnetic field is uniform to 2 % in this region. Candidate secondary vertices were found for each pair of tracks by calculating their two intersection points in the transverse plane. The z-coordinates of both tracks at each candidate vertex were calculated assuming uniform motion in the z-direction. If the tracks did not intersect in the transverse plane, the track pair was rejected from the reconstruction algorithm. Scattering of particles in the walls of the VXD and CTD was neglected. The momentum components of each track measured at the perigee point with respect to the ZEUS z-axis, were extrapolated to each candidate secondary vertex where the total invariant mass of the two particles was calculated assuming they were pions in the case of K_s^0 decay and $p\pi$ in the case of Λ decay.

6.2 K_s^0 Selection Cuts

To improve the K_s^0 signal to background ratio, cuts were applied on:-

1. the separation in z between the daughter tracks at the secondary vertex;
2. the angle, α, between the candidate K_s^0 momentum and its line-of-flight from the primary vertex;
3. the impact parameter of each track with respect to the primary vertex;
4. the mass of the pair of tracks;

Each cut was developed by a similar method to [67], using the default sample of PYTHIA events passed through the full detector simulation. For each variable

studied, the purity and efficiency of K_s^0 reconstruction were calculated as a function of the cut variable. Purity was defined as the ratio of true $K_s^0 \rightarrow \pi^+ \pi^-$ decays to the total number of candidates passing the cuts. Efficiency was defined as the fraction of true $K_s^0 \rightarrow \pi^+ \pi^-$ decays which passed the cut. The optimal value for each cut was selected to be at the maximum of purity*efficiency.

6.2.1 $|\Delta z|$ Cut

The separation in z between the K_s^0 daughter tracks, at the candidate secondary vertex with minimum $|\Delta z|$ is shown in figure 6.1. The $|\Delta z|$ distribution for true K_s^0 is observed to be narrower than for all K_s^0 candidates. There is little variation in the purity*efficiency distribution above $|\Delta z| = 3$ cm, therefore to keep the combinatoric background at a minimum K_s^0 candidates were required to satisfy $|\Delta z| \leq 3$ cm.

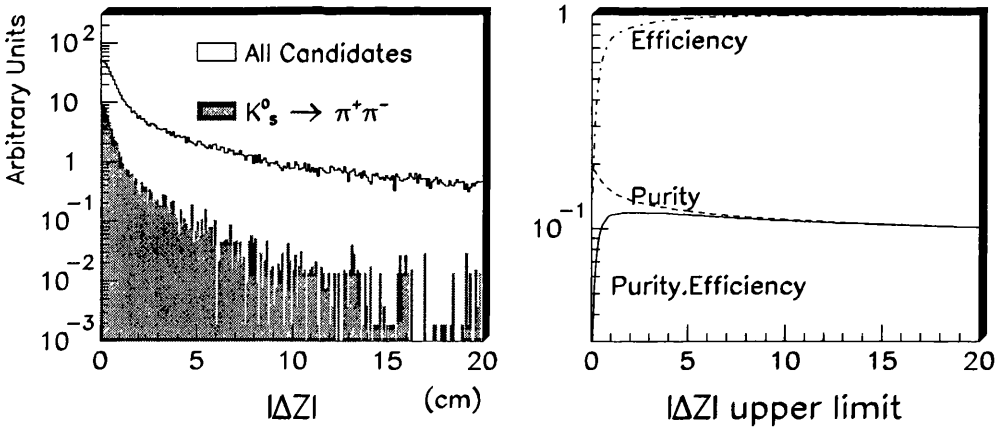

Figure 6.1: Distribution of the z separation between daughter tracks (left) for all K_s^0 candidates, and true K_s^0 candidates. The purity and efficiency (right) of K_s^0 reconstruction as a function of the $|\Delta z|$ upper limit.

6.2.2 Collinearity Cut

The collinearity angle, α, was defined as the angle between the K_s^0 transverse momentum and the line joining the primary to secondary vertex projected onto the $x-y$ plane. The distribution in α for all K_s^0 and true K_s^0 candidates is shown in figure 6.2. The distribution in α is broader for all K_s^0 candidates than for true K_s^0 candidates. The K_s^0 reconstruction purity and efficiency suggest the optimal choice of cut to be $\alpha \leq 8.1°$, or equivalently, $\cos\alpha \geq 0.99$.

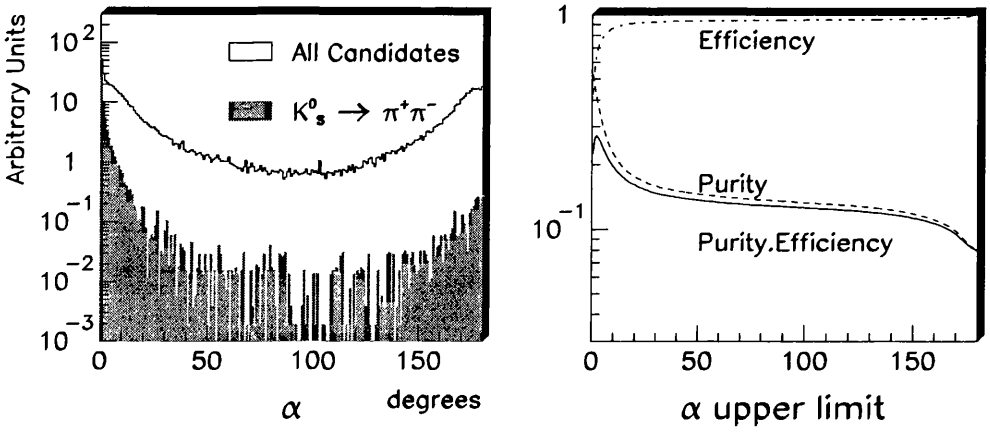

Figure 6.2: Collinearity Angle (left) distribution for all K_s^0 candidates, and true K_s^0 candidates. The purity and efficiency (right) of K_s^0 reconstruction as a function of the collinearity angle upper limit.

6.2.3 Impact Parameter Cut

To reduce the combinatoric background from false K_s^0 candidates associated with tracks on the primary vertex, a cut was made on the impact parameter, $|\epsilon|$, of the daughter tracks used in K_s^0 reconstruction. Figure 6.3 shows the impact parameter distribution for the daughter track with minimum impact parameter for each K_s^0 candidate. Since kaons typically decay a few centimetres from the primary event vertex, the daughter tracks from true K_s^0 candidates have a larger impact parameter than tracks from all K_s^0 candidates, most of which are formed

from track pairs intersecting at the primary event vertex. Compromising between K_s^0 reconstruction purity and efficiency suggests requiring both daughter tracks to have an impact parameter $|\epsilon| \geq 0.3$ cm.

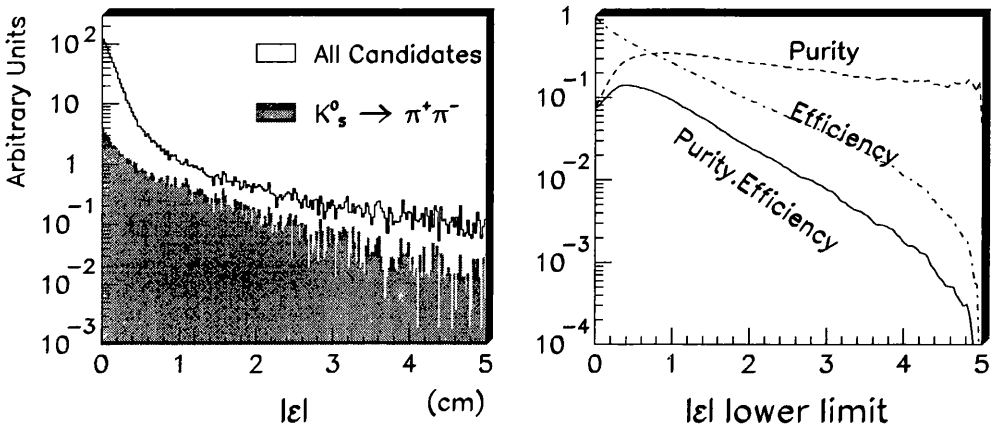

Figure 6.3: Impact parameter (left) distribution for all K_s^0 candidates, and true K_s^0 candidates. The purity and efficiency (right) of K_s^0 reconstruction as a function of the impact parameter lower limit.

6.2.4 Photon Rejection Cut

If a particle of mass m undergoes two body decay to equal mass daughter particles, then the energies of the daughters, E_1, E_2 and the opening angle between them, θ_{12}, are approximatley related by $(E_1 + E_2)\theta_{12} = 2m$. Figure 6.4 shows the $(E_1+E_2)\theta_{12}$ distribution for photon conversions in the double-hatched histogram. Placing a cut at $(E_1 + E_2)\theta_{12} > 0.2$ GeV removes 95 % of the photon conversions in the K_s^0 sample. Also shown is the $(E_1 + E_2)\theta_{12}$ distribution for K_s^0 candidates passing the collinearity, $|\Delta z|$, and impact parameter cuts. As expected, a peak at approximately 1 GeV is observed.

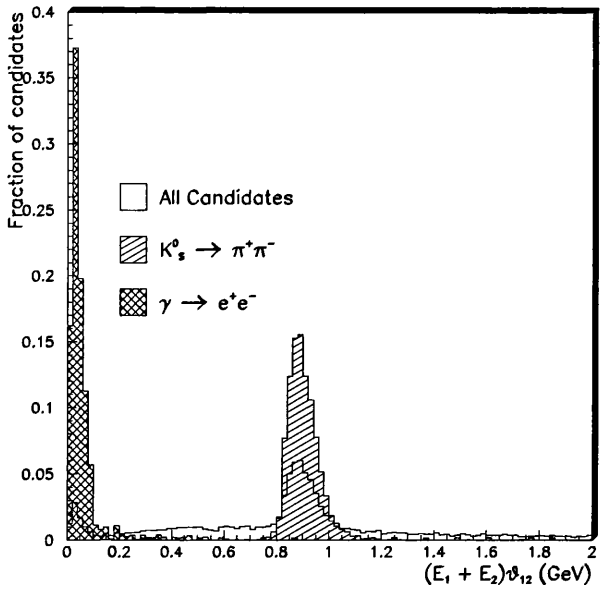

Figure 6.4: The $(E_1 + E_2)\theta_{12}$ distribution for K^0_s candidates passing the collinearity, $|\Delta z|$, and impact parameter cuts for all candidates (blank histogram), true K^0_s decays (single-hatched histogram) and true photon conversions (double-hatched histogram).

6.2.5 $\Lambda(\overline{\Lambda})$ Rejection Cut

By assuming the higher momentum daughter track to be a proton instead of a π, the Λ mass hypothesis was calculated for each track pair. Figure 6.5 shows a plot of $m(p\pi)$ vs. $m(\pi^+\pi^-)$ for each track pair satisfying the above K^0_s selection cuts. K^0_s candidates with a Λ mass hypothesis $m(p\pi) \leq 1.12$ GeV were rejected from the K^0_s sample.

The $p\ \pi^-$ and $\overline{p}\ \pi^+$ mass spectra for Λ and $\overline{\Lambda}$ candidates with $p_T \geq 0.5$ GeV and $|\eta| \leq 1.5$ in the selected data events are shown in figure 6.6. The numbers of Λ and $\overline{\Lambda}$'s are expected to be equal in this pseudorapidity region. The $p\ \pi^-$ and $\overline{p}\ \pi^+$ mass spectra were fitted by the function

$$f(m) = g(m) + bg(m) \tag{6.1}$$

where the signal was given by the Gaussian,

$$g(m) = \frac{N(\Lambda)}{\sqrt{2\pi}\sigma} \exp\left(-\frac{1}{2}\left(\frac{m - m(\Lambda)}{\sigma}\right)^2\right) \tag{6.2}$$

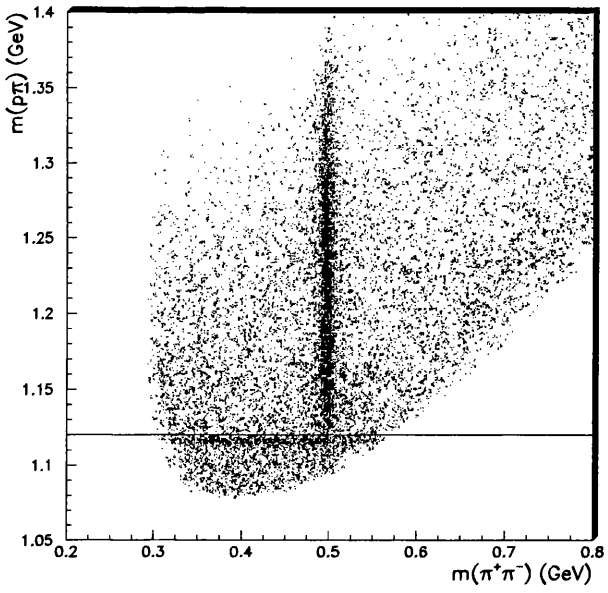

Figure 6.5: Invariant mass of candidates using two mass hypotheses, $\pi^+\pi^-$ and $p\pi$. Candidates in K^0_s sample with $m(p\pi) < 1.12$ GeV were rejected as being probable Λ candidates.

and the background by,

$$bg(m) = (m - m_{THR})^a \cdot \exp(bm + cm^2 + dm^3) \tag{6.3}$$

$m_{THR} = 1.077$ being the threshold mass. The fit gave 297 ± 22 Λ and 320 ± 25 $\overline{\Lambda}$ candidates. The Λ and $\overline{\Lambda}$ masses were determined to be $m(\Lambda) = 1116.0 \pm 0.2$ MeV and $m(\overline{\Lambda}) = 1116.1 \pm 0.2$ MeV, in fair agreement with the PDG value, 1115.7 ± 0.006 MeV [68].

6.2.6 Data - Monte Carlo K^0 Selection Cut Comparison

A comparison between data and the PYTHIA Monte Carlo simulation of the cut variables used in the isolation of a K^0_s signal is shown in figure 6.7. Plots 6.7(a - c) show a comparison of the $|\Delta z|$, $\cos\alpha$ and $|\epsilon|$ distributions, requiring *only* that the K^0_s candidates have $m(\pi^+\pi^-) = 0.497 \pm 0.25$ GeV. The background candidates in the signal region are therefore still present in these plots. Although the widths of the peaks in the data and Monte Carlo differ in the $|\Delta z|$ and $\cos\alpha$ distributions, the cuts generously contain the peaks, are not in sensitive regions and the tails

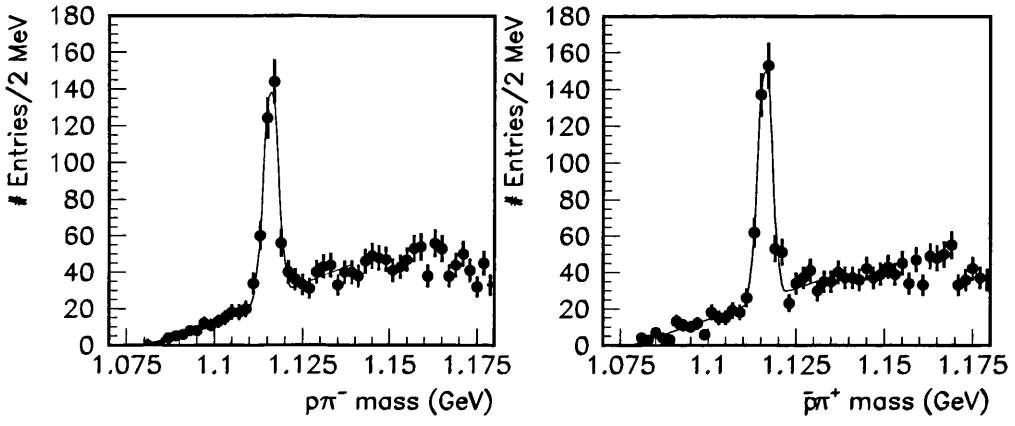

Figure 6.6: Invariant mass spectra of Λ (left) and $\overline{\Lambda}$ (right) candidates with $p_T \geq 0.5$ GeV and $|\eta| \leq 1.5$ in hard photoproduction events with $0.15 \leq y_{JB} \leq 0.7$, containing a calorimeter jet with $E_T^{UCAL} \geq 7$ GeV and $|\eta^{UCAL}| \leq 0.5$.

are well described. Figure 6.7(c) shows good agreement in the impact parameter distribution in data and Monte Carlo. The $(E_1 + E_2)\theta_{12}$ distribution is plotted in figure 6.7(d) before applying any K_s^0 selection cuts and shows good agreement between the data and Monte Carlo.

A comparison of the combined $p\ \pi^-$ and $\overline{p}\ \pi^+$ mass spectra in the data and resolved plus direct Monte Carlo is shown in figure 6.8. The Monte Carlo histogram is normalised to the number of entries in the data histogram and is seen to agree well with the data.

6.3 K_s^0 Reconstruction Resolution

The accuracy and resolution of the K_s^0 reconstruction method was evaluated from PYTHIA events with default parameter settings passed through the full detector simulation, by comparing the values of reconstructed and true variables for true K_s^0 candidates. The accuracy of the secondary vertex reconstruction is demonstrated in figure 6.9 and 6.10. The error bars in figures 6.9 and 6.10 represent the RMS of the plotted quantities.

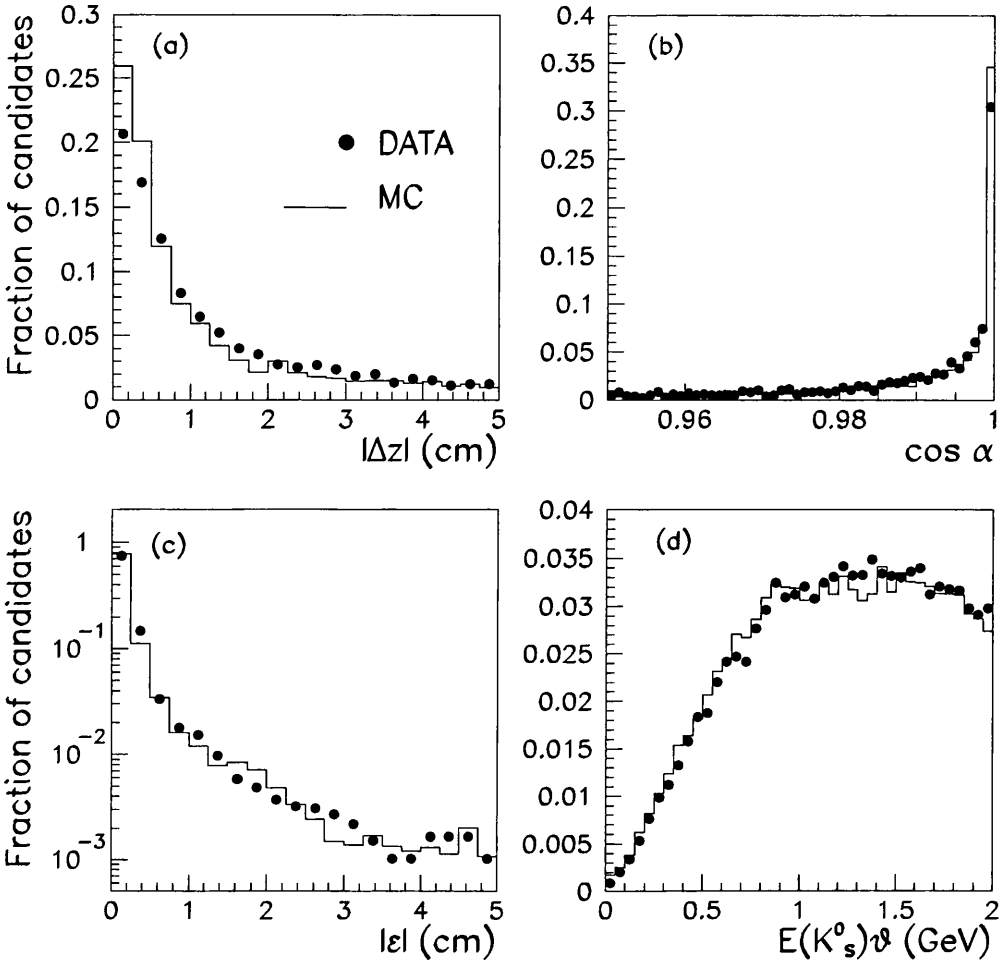

Figure 6.7: Comparison of $|z|$ (a), $\cos\alpha$ (b), $|\epsilon|$ (c) and $(E_1+E_2)\theta_{12}$ (d) distributions in data (filled circles) and mixed resolved plus direct PYTHIA Monte Carlo (histogram).

The difference between the reconstructed and true (x, y, z) coordinates of the secondary vertex are plotted in figures 6.9(a), (d) and (g). The mean of each distribution is compatible with zero. Figures 6.9(b), (e) and (h) show the difference between the reconstructed and true (x, y, z) coordinates of the secondary vertex plotted against azimuthal angle of the secondary vertex. The reconstructed secondary vertex is accurately reconstructed over all azimuth. The RMS of the vertex reconstruction is observed to vary in x and y with azimuth. This was attributed to the error in the secondary vertex coordinate

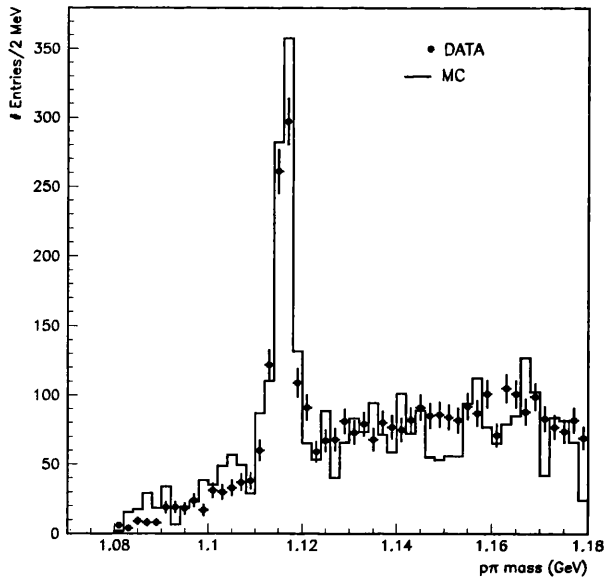

Figure 6.8: Combined invariant mass spectra of Λ and $\overline{\Lambda}$ candidates with $p_T \geq 0.5$ GeV and $|\eta| \leq 1.5$ in hard photoproduction events with $0.15 \leq y_{JB} \leq 0.7$, containing a calorimeter jet with $E_T^{UCAL} \geq 7$ GeV and $|\eta^{UCAL}| \leq 0.5$. The data (filled circles) is compared to the resolved plus direct default PYTHIA Monte Carlo distribution (histogram).

reconstruction being dominated by the radial position rather than azimuthal angle. Figures 6.9(c), (f) and (i) show the difference between the reconstructed and true (x, y, z) coordinates of the secondary vertex plotted against polar angle of the secondary vertex. The reconstructed secondary vertex is accurately reconstructed over the whole polar angle range.

Figures 6.10(a) (d) and (g) show the difference between the reconstructed K_s^0 (p_T, η, p_z) and the true K_s^0 (p_T, η, p_z); the offset in p_T^{reco}, η^{reco} and p_z^{reco} relative to the true value is negligible. The resolution was observed to be dependent on p_T and p_z, but flat in η, $\sigma(\eta) = 0.01$ in figures 6.10(b), (e) and (h). Figures 6.10(c), (f) and (i) show the difference between the reconstructed and true K_s^0 (p_T, η, p_z) as a function of pseudorapidity. Only the p_z reconstruction resolution is observed to be η dependent and only at large $|\eta|$.

The bin sizes for the multiplicity measurements in p_T and η were chosen such that migration effects due to the K_s^0 reconstruction resolution were negligible,

and also so that there was a large enough K_s^0 signal with which to evaluate the K_s^0 reconstruction efficiency.

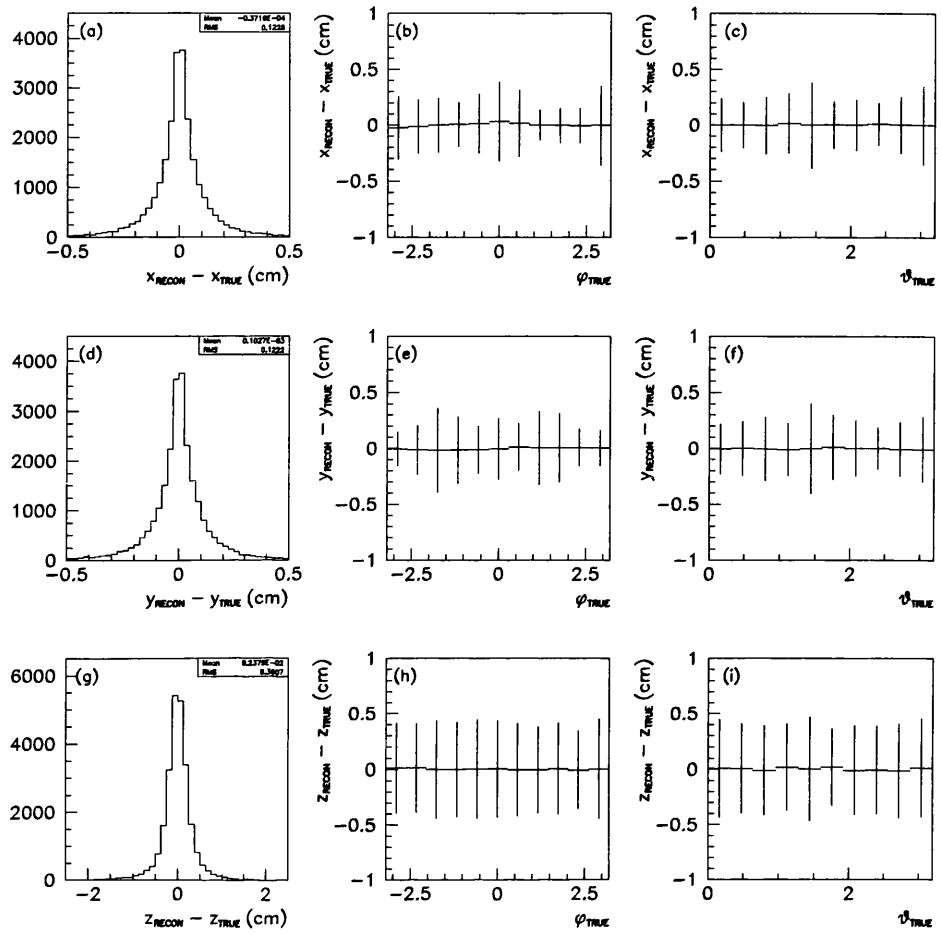

Figure 6.9: K_s^0 secondary vertex reconstruction resolution. The error bars represent the RMS of the quantity plotted.

6.4 K_s^0 Signal

The $\pi^+\pi^-$ mass spectra obtained from the ZEUS 1994 e^+ p data and the default PYTHIA resolved plus direct Monte Carlo after applying all event and K_s^0 selection cuts are shown in figure 6.11. A K_s^0 peak over a low level, slowly varying background is observed in both the data and Monte Carlo distributions.

The number of reconstructed K_s^0 was estimated in this analysis by using a

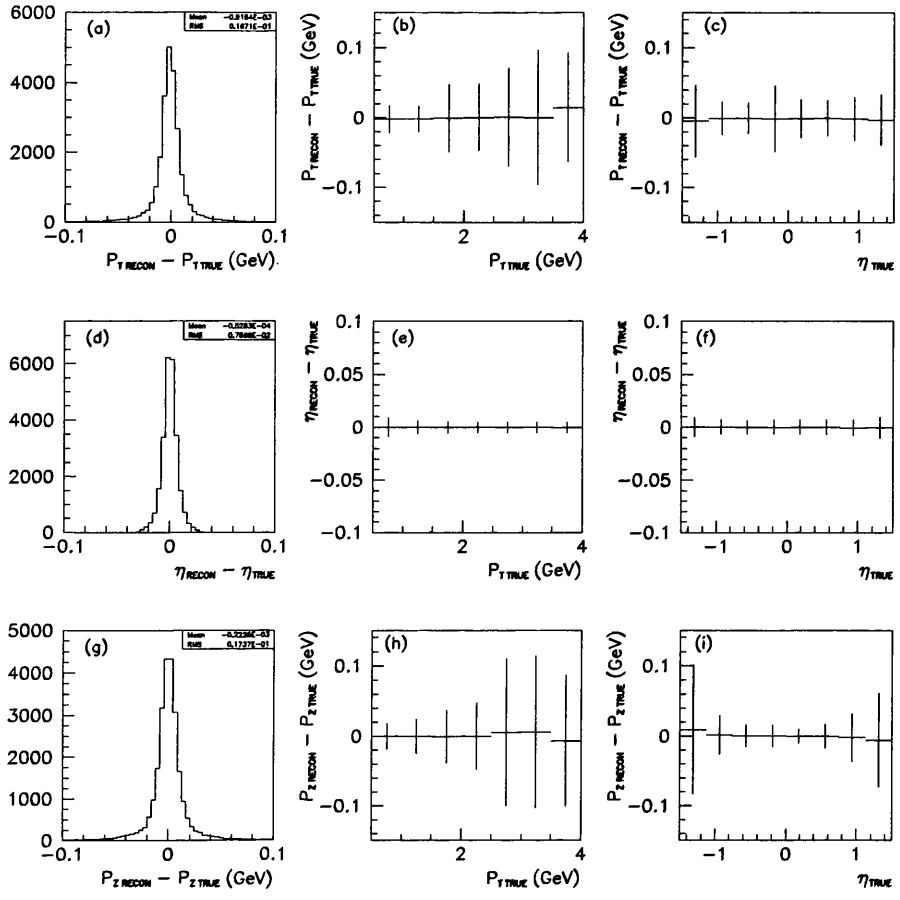

Figure 6.10: K^0_s reconstruction resolutions in p_T, η and p_z. The error bars represent the RMS of the quantity plotted.

background subtraction technique. In this method the K^0_s signal was calculated as the number of candidates within 25 MeV of the nominal K^0_s mass and the background was given by the average of the number of candidates within windows at $0.4 - 0.45$ and $0.55 - 0.6$ GeV. The Monte Carlo histogram in figure 6.11 was normalised to have the same average number of candidates in the background windows as the data. A signal of 3580 ± 65 K^0_s candidates was obtained from the data sample. This result was checked by fitting the $\pi^+\pi^-$ mass spectrum with a double gaussian signal and a linear background. The fit gave 3759 ± 40 K^0_s candidates which was consistent with the background subtraction technique once candidates in the tails of the K^0_s signal outside the 25 MeV signal window

had been accounted for. In the Monte Carlo 96 % of K_s^0 candidates contained in the two gaussian signals were reconstructed with a mass inside the K_s^0 signal region. This was consistent with the data where 95 % of K_s^0 candidates in the two gaussian signals lay in the K_s^0 signal region.

The K_s^0 mass was calculated from the double gaussian fit by weighting the mean of each gaussian according to the fraction of the total number of K_s^0 candidates contained in each gaussian. The K_s^0 mass determined from the data was 497.2±0.2 MeV, consistent with the K_s^0 mass obtained from the Monte Carlo, 497.1 MeV, but slightly low compared to the PDG value of 497.67±0.03 MeV [68]. The K_s^0 mass quoted above was determined using the VXD, CTD and RTD tracking detectors. It was consistent with the K_s^0 mass determined using the CTD tracking information alone.

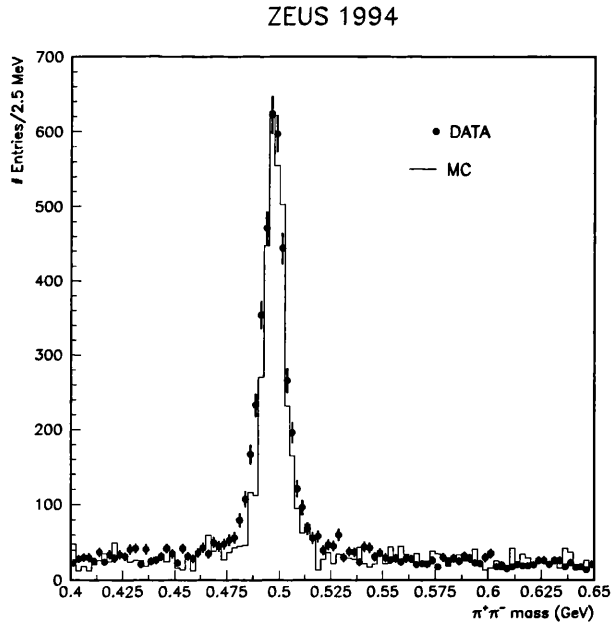

Figure 6.11: The reconstructed $\pi^+\pi^-$ mass spectrum from 1994 ZEUS data (full circles) compared to the $\pi^+\pi^-$ mass spectrum predicted by the default resolved plus direct PYTHIA Monte Carlo (histogram).

As a further check of the K_s^0 reconstruction figure 6.12 shows the proper $c\tau$ distribution in the data (full circles) compared to the default resolved plus direct PYTHIA Monte Carlo (histogram). The contribution to the $c\tau$ distribution

from K_s^0 background candidates was subtracted from the data and Monte Carlo histograms. The Monte Carlo was normalised to give the same number of entries as the data. The K_s^0 lifetime was estimated using a similar approach to TASSO's B hadron lifetime measurement [69]. The default Monte Carlo K_s^0 $c\tau$ distribution was reweighted to give different K_s^0 lifetimes according to

$$n_{K_s^0}^{MC}(c\tau_i; c\tau') = n_{K_s^0}^{MC}(c\tau_i; c\tau_o)\exp(c\tau_i(\frac{c\tau' - c\tau_o}{c\tau_o c\tau'})) \tag{6.4}$$

where $n_{K_s^0}^{MC}(c\tau_i; c\tau_o)$ is the number of observed K_s^0 decays in the bin $c\tau_i$ for a K_s^0 lifetime of $c\tau_o$. The K_s^0 decays were simulated by MOZART with a lifetime of $c\tau_o = 2.676$ cm and the $c\tau$ distribution was reweighted to lifetime values in the range $2.45 < c\tau' < 2.95$ cm. The χ^2 value for each K_s^0 lifetime was calculated according to

$$\chi^2(c\tau') = \sum_{i=1}^{n} \frac{(n_{K_s^0}^{DATA}(c\tau_i) - n_{K_s^0}^{PYTHIA}(c\tau_i; c\tau'))^2}{(n_{K_s^0}^{DATA}(c\tau_i) + n_{K_s^0}^{PYTHIA}(c\tau_i; c\tau'))} \tag{6.5}$$

where the sum was taken over all bins in the range, $0.5 \leq c\tau_i \leq 10$ cm. The lifetime obtained was insensitive to inclusion of the first bin of the $c\tau$ distribution. The dependence of χ^2 on K_s^0 lifetime is also shown in figure 6.12. The best fit of the PYTHIA lifetime distribution to the data is shown in figure 6.12 and gave a K_s^0 lifetime of $c\tau_o = 2.72^{+0.10}_{-0.04}$ cm in agreement with the value used for the Monte Carlo generation and the PDG value [68].

6.5 Uncorrected K_s^0 Inclusive Multiplicities.

The starting point for determining the inclusive multiplicities $\frac{1}{N_{JETS}}\frac{dN(K_s^0)}{dp_T^2}$, $\frac{1}{N_{JETS}}\frac{dN(K_s^0)}{d\eta}$ in hard photoproduction events was calculating the numbers of reconstructed K_s^0 uncorrected for K_s^0 reconstruction and event selection inefficiencies, and the effect of the detector on the reconstruction of the quantities characterising the kinematics of hard photoproduction events, y_{JB} and the jet transverse energies. The background subtraction technique described in section 6.4 was used to estimate the numbers of reconstructed K_s^0 from the $\pi^+\pi^-$ mass spectra split into p_T and η bins.

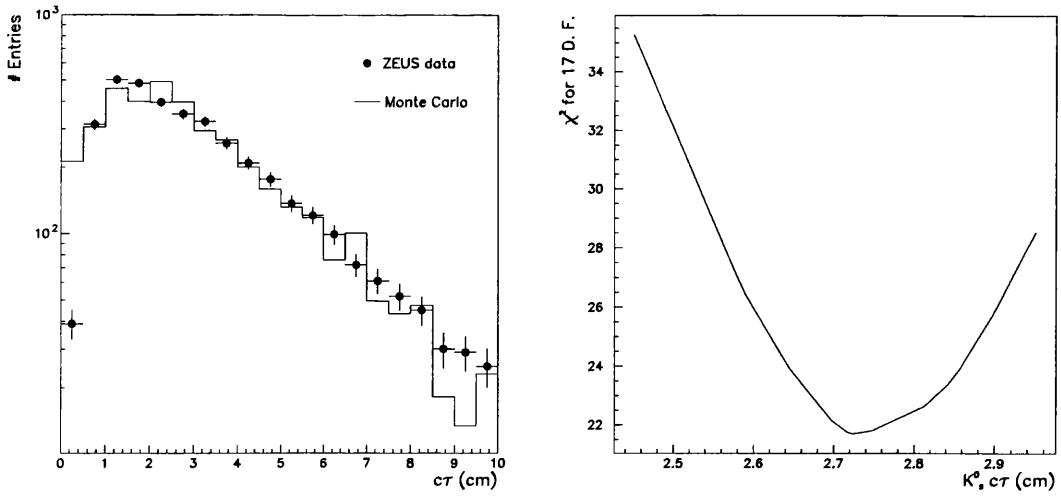

Figure 6.12: The reconstructed K_s^0 proper lifetime distribution in data (full circles) and the reweighted resolved plus direct PYTHIA distribution (histogram) which best fit the data (left) and the χ^2 distribution as a function of K_s^0 lifetime (right).

Figure 6.13 shows the $\pi^+\pi^-$ mass spectra in the chosen p_T bins and the number of reconstructed K_s^0 is given in table 6.1. The uncorrected $\frac{1}{N_{JETS}}\frac{dN(K_s^0)}{dp_T^2}$ inclusive multiplicity is compared to several PYTHIA Monte Carlo samples in figure 6.15(a). The default PYTHIA Monte Carlo sample describes the data reasonably at $0.5 < p_T < 0.75$ GeV, and well at $p_T > 0.75$ GeV. PYTHIA reweighted with the LAC1 photon structure function also provides a good description of the data. The $P_s/P_u = 0.20$ PYTHIA sample underestimates the uncorrected number of K_s^0 in the data over the full p_T range, while PYTHIA with multiple interactions tends to overestimate the data at low p_T.

The $\pi^+\pi^-$ mass spectra in the chosen η bins are shown in figure 6.14, and the number of reconstructed K_s^0 are given in table 6.2. The uncorrected $\frac{1}{N_{JETS}}\frac{dN(K_s^0)}{d\eta}$ inclusive multiplicity is compared to several PYTHIA Monte Carlo samples in figure 6.15(b). In contrast with the p_T spectrum, the $P_s/P_u = 0.20$ PYTHIA sample describes the data better than the default PYTHIA and LAC1 Monte Carlo samples in the negative pseudorapidity region. There is, however, an excess in the data at $\eta > 0.75$ which is poorly modelled by all the Monte Carlo samples, except for PYTHIA with multiple interactions. However, PYTHIA with multiple

p_T range (GeV)	Reconstructed K_s^0
$0.5 \leq p_T < 0.625$	332 ± 24
$0.625 \leq p_T < 0.75$	384 ± 24
$0.75 \leq p_T < 1.0$	716 ± 30
$1.0 \leq p_T < 1.4$	814 ± 31
$1.4 \leq p_T < 1.95$	661 ± 27
$1.95 \leq p_T < 2.5$	341 ± 20
$2.5 \leq p_T < 4.0$	302 ± 19

Table 6.1: Numbers of reconstructed K_s^0 in p_T bins.

η range	Reconstructed K_s^0
$-1.5 \leq \eta < -1.125$	80 ± 10
$-1.125 \leq \eta < -0.75$	252 ± 18
$-0.75 \leq \eta < -0.375$	398 ± 22
$-0.375 \leq \eta < 0$	642 ± 28
$0 \leq \eta < 0.375$	768 ± 31
$0.375 \leq \eta < 0.75$	652 ± 29
$0.75 \leq \eta < 1.125$	498 ± 26
$1.125 \leq \eta < 1.5$	313 ± 21

Table 6.2: Numbers of reconstructed K_s^0 in η bins.

interactions overestimates the K_s^0 multiplicity at central pseudorapidities. Integrating over $|\eta(K_s^0)| < 1.5$ apparently averages out the difference in shape of the data and Monte Carlo η spectra so that the default PYTHIA Monte Carlo p_T spectrum appears to give a good description of the data.

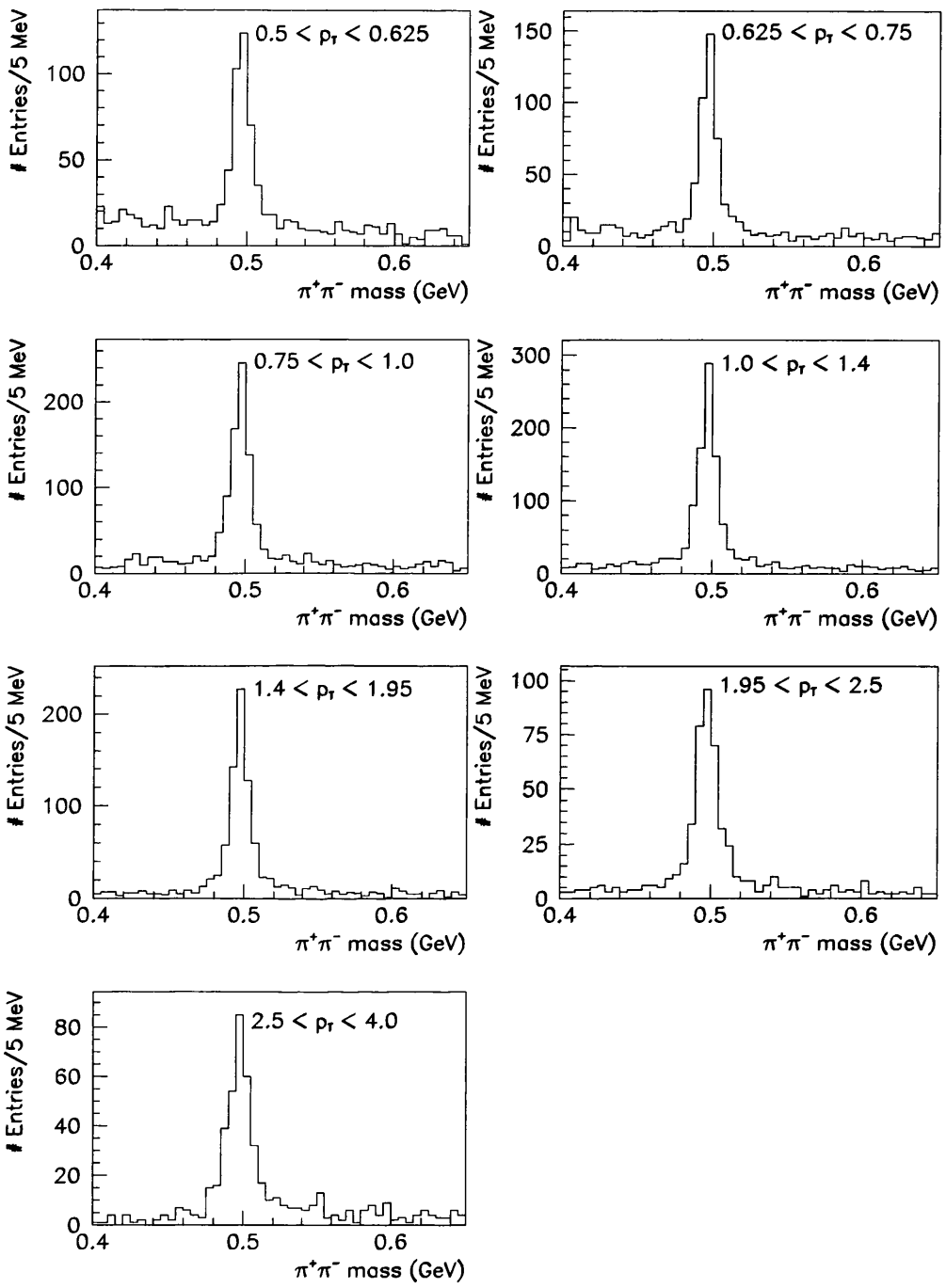

Figure 6.13: Reconstructed $\pi^+\pi^-$ mass spectra in the bins used for $\frac{1}{N_{JETS}}\frac{dN(K^0)}{dp_T^2}$ multiplicity determination.

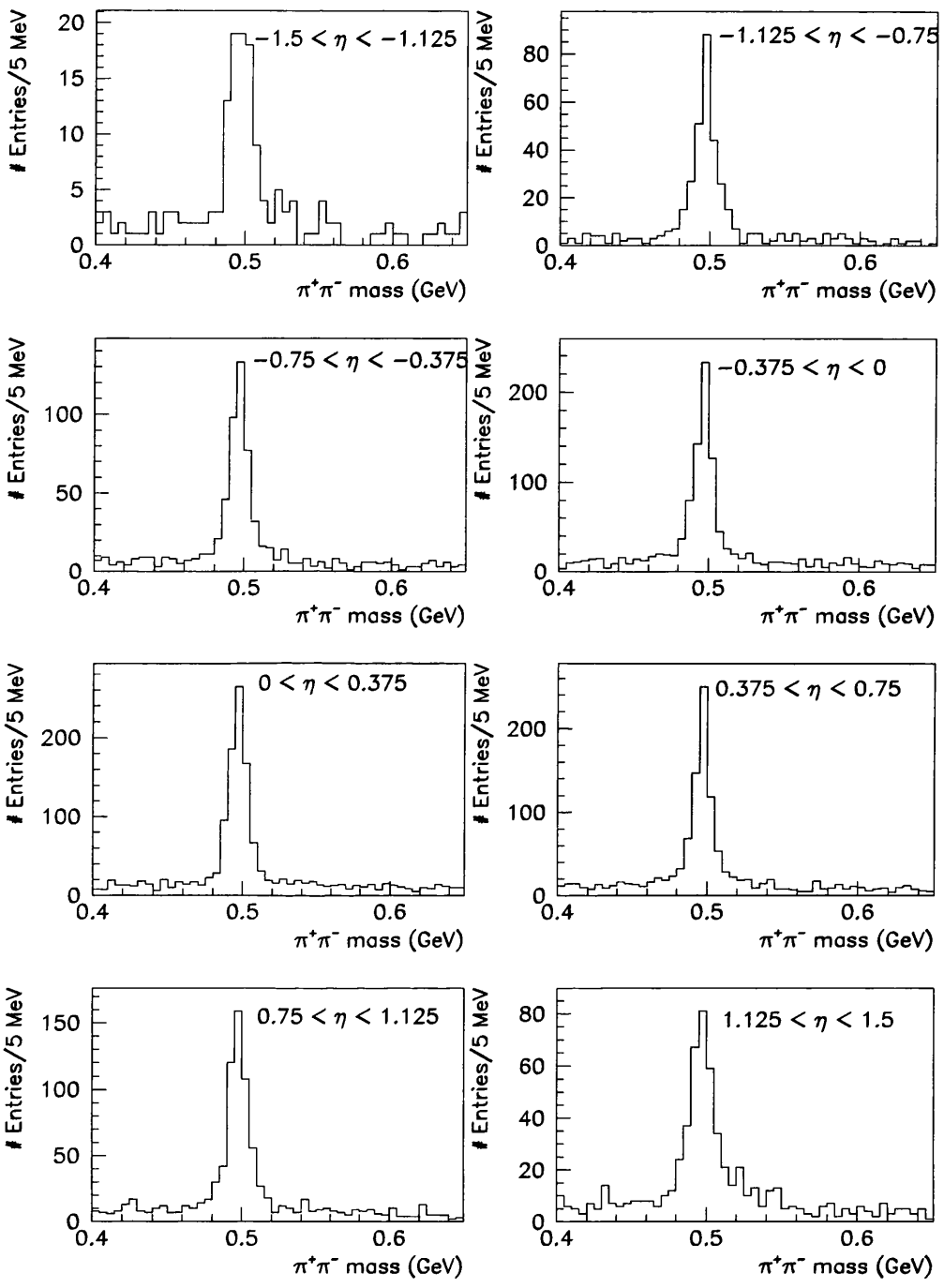

Figure 6.14: Reconstructed $\pi^+\pi^-$ mass spectra in the bins used for $\frac{1}{N_{JETS}}\frac{dN(K^0)}{d\eta}$ multiplicity determination.

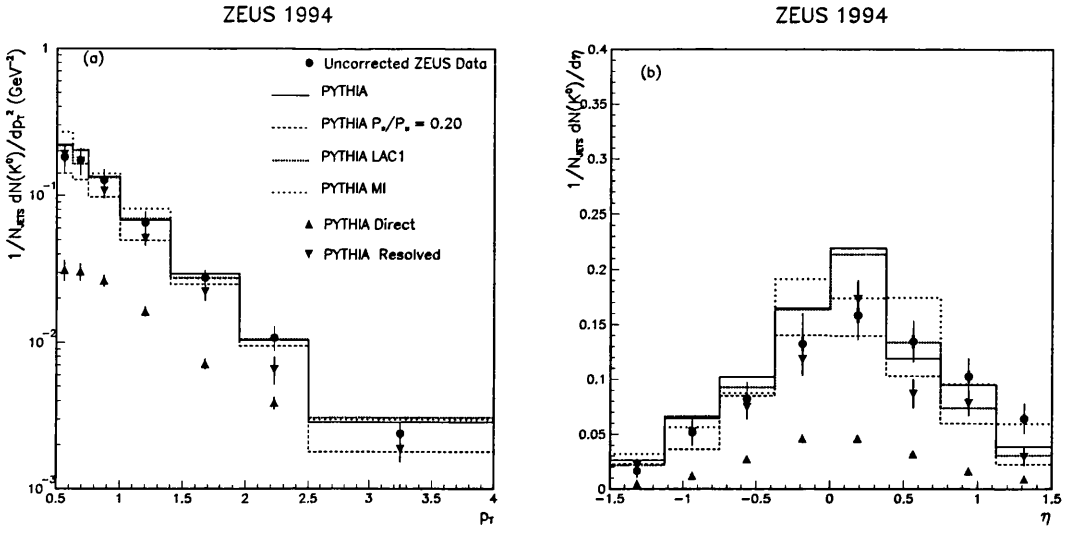

Figure 6.15: Uncorrected K_s^0 inclusive multiplicities as a function of p_T (a) and η (b) in hard photoproduction events with $0.15 \leq y_{JB} \leq 0.7$, containing a calorimeter jet with $E_T^{UCAL} \geq$ 7 GeV and $|\eta^{UCAL}| \leq 0.5$. The data (filled circles) is compared to PYTHIA samples of direct (triangles), resolved (inverted triangles), mixed resolved plus direct (solid line), mixed $P_s/P_u = 0.20$ (dash-dotted line), mixed with LAC1 photon structure function(dotted line), and with multiple interactions (sparse dotted).

6.6 Correction Procedure

The uncorrected PYTHIA Monte Carlo sample described the shape of the uncorrected K_s^0 p_T and η spectra in the data reasonably well, except in the region $\eta > 0.75$. It was therefore possible to use the PYTHIA sample to determine correction factors which could be applied to the uncorrected data to obtain the true inclusive multiplicities $\frac{1}{N_{JETS}} \frac{dN(K^0)}{dp_T^2}$, $\frac{1}{N_{JETS}} \frac{dN(K^0)}{d\eta}$ corrected back to hadron level events defined in section 5.2, bearing in mind that the results in the region $\eta > 0.75$ suffer from a model-dependent systematic error.

For any distribution, the following bin-by-bin correction factors were calculated:-

- K_s^0 **Reconstruction Efficiency.** This was determined from Monte Carlo events passing the data selection criteria of section 5. For any variable, x,

the K_s^0 reconstruction efficiency was defined as,

$$\epsilon_{K_s^0}(x) = \frac{N^{obs}_{SELRECO}(x)}{N^{gen}_{SELRECO}(x)} \tag{6.6}$$

where $N^{obs}_{SELRECO}(x)$ was the number of observed $K_s^0 \to \pi^+\pi^-$ decays counted using the background subtraction technique in selected reconstruction level events, and $N^{gen}_{SELRECO}(x)$ was the number of generated $K_s^0 \to \pi^+\pi^-$ decays in selected reconstruction level events.

- **Trigger Efficiency.** This correction factor accounted for losses in the number of reconstructed K_s^0 due to event selection cuts or trigger criteria. The trigger efficiency was defined as

$$\epsilon_{trig}(x) = \frac{N^{gen}_{SELRECO}(x)}{N^{gen}_{RECO}(x)} \tag{6.7}$$

where $N^{gen}_{RECO}(x)$ was the number of generated $K_s^0 \to \pi^+\pi^-$ decays in all events reconstructed as having $0.15 \leq y_{JB} \leq 0.7$ and at least one jet satisfying $E_T^{UCAL} \geq 7$ GeV, $|\eta^{UCAL}| \leq 0.5$, irrespective of whether they satisfied the trigger criteria.

- **RECO-to-HADRON level Correction Factor.** This was defined as

$$C(x) = \frac{N^{gen}_{RECO}(x)}{N^{gen}_{HAD}(x)} \tag{6.8}$$

where $N^{gen}_{HAD}(x)$ was the number of generated $K_s^0 \to \pi^+\pi^-$ decays in hadron level events with $0.2 \leq y \leq 0.85$ and at least one jet satisfying $E_T^{HAD} \geq 8$ GeV, $|\eta^{HAD}| \leq 0.5$.

In this way, the correction factors accounted for

- K_s^0 reconstruction efficiency due to selection criteria;
- daughter track reconstruction inefficiency;
- event selection and reconstruction efficiency;
- migration in K_s^0 p_T and η;

- migration in jet E_T and η.

The effects of migration are discussed in section 6.7. The errors on the K_s^0 reconstruction and trigger efficiencies were calculated according to the binomial theorem, for example in each p_T bin the error on the K_s^0 reconstruction efficiency was calculated from,

$$\sigma(\epsilon_{K_s^0}) = \sqrt{\frac{\epsilon_{K_s^0}(1-\epsilon_{K_s^0})}{N^{gen}_{SELRECO}}} \tag{6.9}$$

Figure 6.16 shows the K_s^0 reconstruction efficiency as a function of p_T and η. The main factor contributing to the low value of the K_s^0 reconstruction efficiency is the impact parameter cut, which enhances the signal-to-background ratio in the $\pi^+ \pi^-$ spectrum by removing K_s^0 candidates arising from the large number of intersecting tracks at the primary vertex. The reconstruction efficiency increased with p_T until $p_T \sim 2$ GeV then decreased. One expects low p_T particles to have a lower track reconstruction efficiency than higher p_T tracks because low momentum tracks which do not have enough transverse momentum to traverse all 9 superlayers in the CTD, describe several periods of a helical trajectory, then exit at the CTD endplates. These particle tracks are less accurately measured than higher p_T tracks since they are often split during the track reconstruction and have fewer measured points. The decrease in K_s^0 reconstruction efficiency at $p_T > 2$ GeV was attributed to longer lived K_s^0 decay within the tracking detectors decreasing the daughter track length available for reconstruction.

The event selection efficiencies for accepting events with a calorimeter level jet satisfying $E_T^{UCAL} \geq 7$ GeV, $\eta^{UCAL} \leq 0.5$ as a function of K_s^0 p_T and η are shown in figure 6.17. All distributions were flat at around 95 %. As one would expect, losses arose here from events failing the background rejection cuts rather than the trigger criteria.

The UCAL-to-HADRON level correction factor is shown in figure 6.18 as a function of K_s^0 p_T and η. There is no strong dependence on either p_T or η.

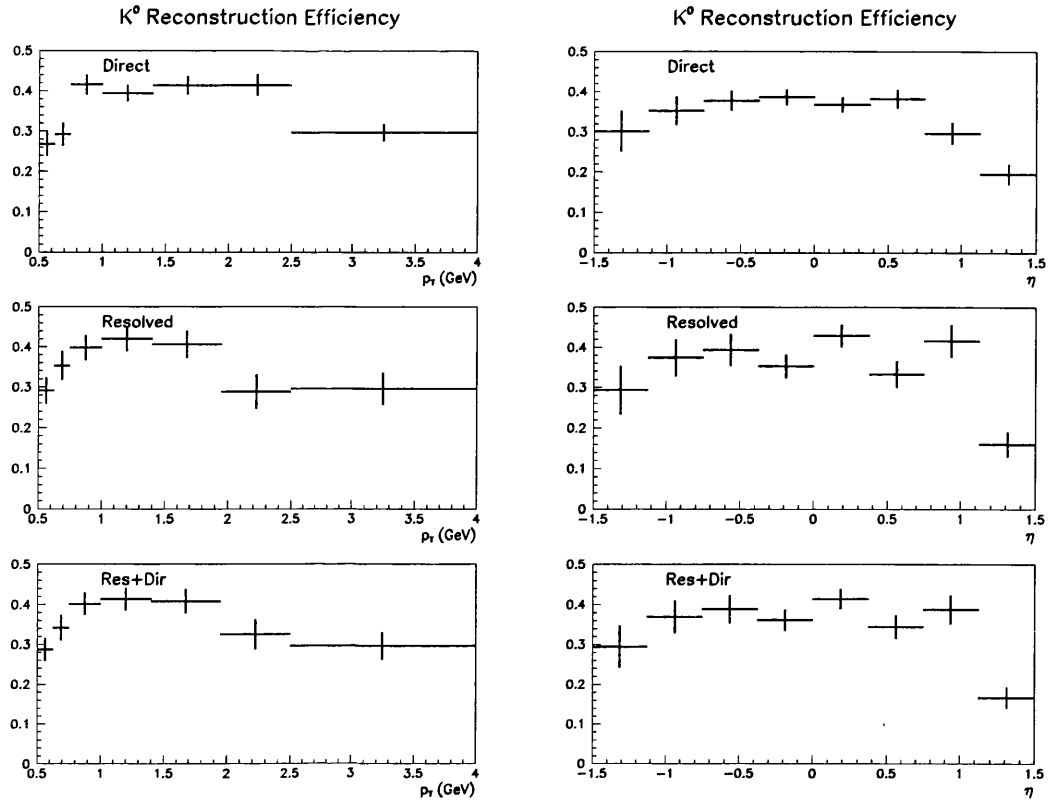

Figure 6.16: K^0_s reconstruction efficiency as a function of p_T (left column) and η (right column) for direct (top row), resolved (middle row) and mixed resolved plus direct (bottom row) PYTHIA Monte Carlo samples.

6.7 Effects of Migration

In section 6.3 it was shown that the K^0_s p_T and η reconstruction was extremely accurate. Since the bins in the inclusive multiplicity distributions are much larger than the K^0_s reconstruction resolution bin-to-bin migrations will be very small and have been neglected in this analysis.

The jet reconstruction resolution is, however, a large source of event migration. While the jet η reconstruction was shown to be accurate and had a resolution of 6° there is a shift of –13% between the hadron and calorimeter level jet E_T with a resolution of 11%. Coupled to the steeply falling jet cross section in E_T, the jet reconstruction gives rise to event migrations. A PYTHIA Monte Carlo sample was generated as described in section 2.5 but without any jet enrichment requirements to study event migration. It was found that approximately 30% of generated

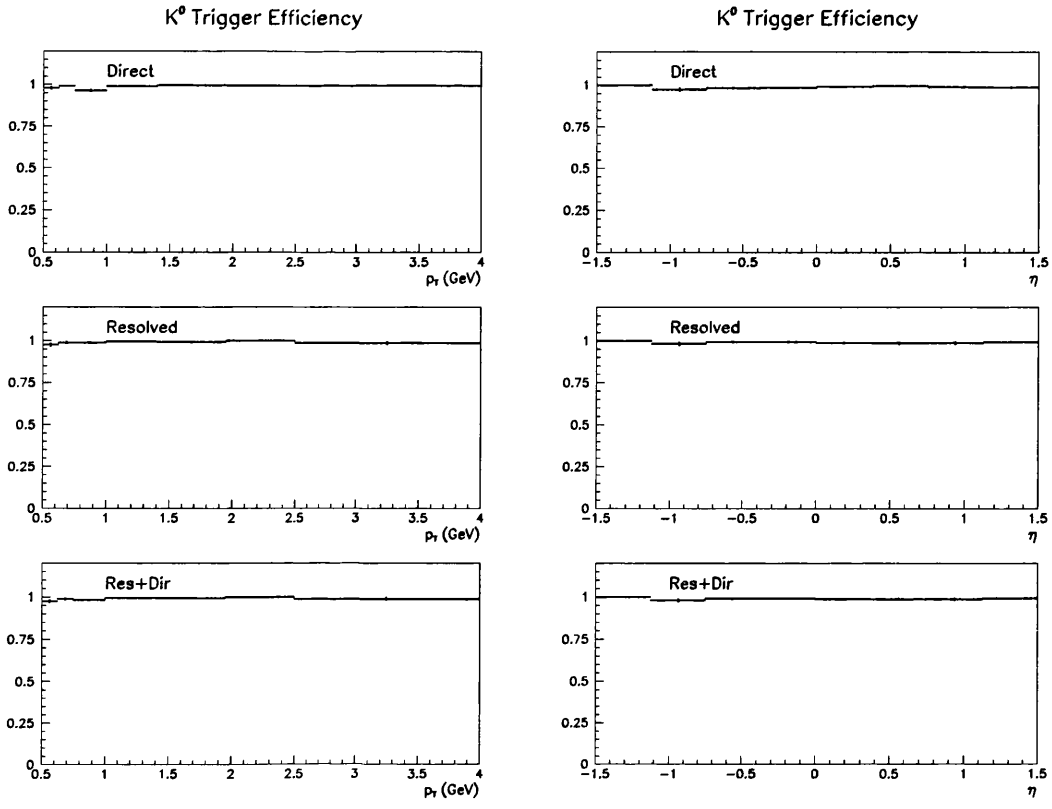

Figure 6.17: Trigger efficiency as a function of p_T (left column) and η (right column) for direct (top row), resolved (middle row) and mixed resolved plus direct (bottom row) PYTHIA Monte Carlo samples.

events which passed the hadron level selection criteria failed the calorimeter level criteria and so migrated out of the measurement region. Conversely, approximately 20% of events which failed the hadron level selection criteria passed the calorimeter level criteria, migrating into the measurement region.

Of more importance to this analysis is how the migrating events change the inclusive multiplicity distributions. Figure 6.19 shows the resolved plus direct uncorrected K^0_s multiplicity p_T and η spectra for events passing the jet and y_{JB} selection criteria. These are compared to the K^0_s spectra for events migrating into and out of the measurement region. In general, the p_T and η spectra of selected and migrant events are consistent within errors. The K^0_s multiplicity decreases by 1% due to event migration.

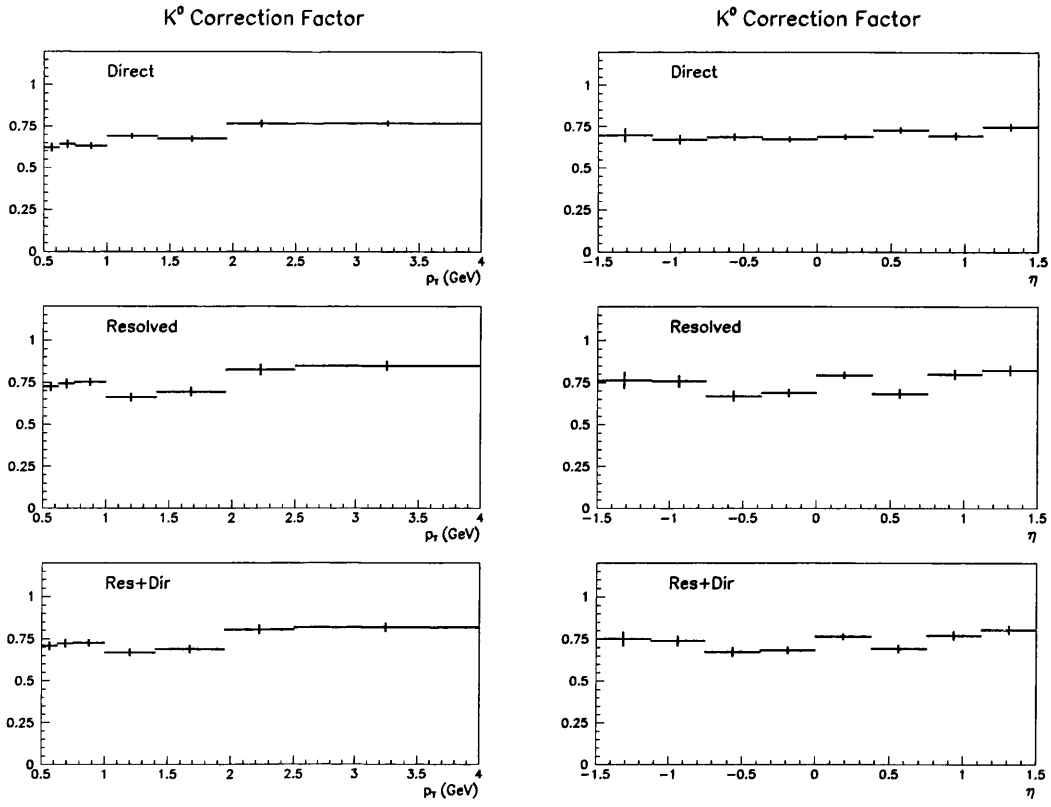

Figure 6.18: Correction factor as a function of p_T (left column) and η (right column) for direct (top row), resolved (middle row) and mixed resolved plus direct (bottom row) PYTHIA Monte Carlo sample.

6.8 Systematic Errors

The systematic errors for each of the K^0 distributions have been calculated on a point-by-point basis. The systematic error attributed to each aspect of the analysis was calculated by changing a cut or reconstruction procedure in the Monte Carlo and data, and comparing the subsequent corrected result with the corrected result from the nominal cuts and procedure. Where two changes were made to a particular cut e.g. the primary vertex cut, the systematic error on each point was taken as the largest shift in the measured quantity. The total systematic error was then calculated by combining the change from each systematic variation in quadrature. The changes made to the analysis procedure are discussed in the following section.

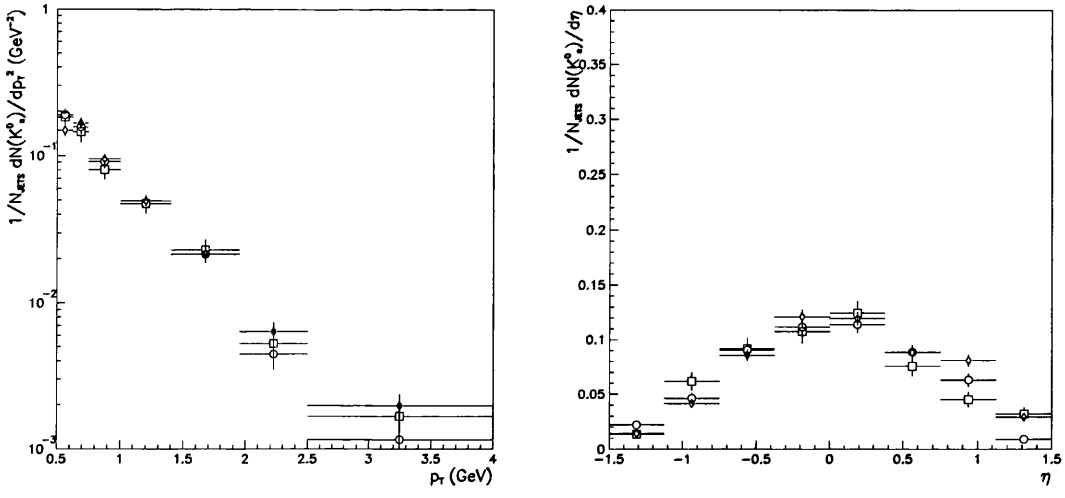

Figure 6.19: The uncorrected K^0_s multiplicity spectra (diamonds) as functions of p_T (left) and η (right), compared to the multiplicity spectra for events migrating into (circles), and events migrating out of the event selection region (squares).

6.8.1 Systematic Changes to Analysis Procedure

The following changes were made in the analysis procedure to calculate the systematic errors associated with each cut, or reconstruction procedure.

Event Selection Cuts

1. As shown in figure 5.3, for events with a e^+ scattered into the LUMI EDET the value of y_{JB} measured in the UCAL was about 20 % lower than y_{LUMI}. The stability of the distributions obtained by correcting data events satisfying $0.15 < y_{JB} < 0.7$ with Monte Carlo events satisfying $0.2 < y < 0.85$ was tested by changing the data cut to $0.2 < y < 0.8$ and leaving the Monte Carlo cut unchanged.

2. The primary vertex position cut was changed from $-37 \leq z \leq 45$ cm to $-32 \leq z \leq 40$ cm and $-42 \leq z \leq 50$ cm.

3. The n_{bad} cut was changed from $n_{bad} \leq 3$ to $n_{bad} \leq 2$ and $n_{bad} \leq 4$.

4. The missing transverse momentum cut was changed from $\frac{p\not{t}}{\sqrt{E_T}} \leq 2$ GeV$^{1/2}$ to $\frac{p\not{t}}{\sqrt{E_T}} \leq 1.8$ GeV$^{1/2}$ and $\frac{p\not{t}}{\sqrt{E_T}} \leq 2.2$ GeV$^{1/2}$

5. The UCAL timing cut was changed from $t_u - t_d \geq -6$ ns to $t_u - t_d \geq -5$ ns and $t_u - t_d \geq -7$ ns

6. The EEXOTIC [70] and SINISTRA [71] electron finders were used instead of the ELEC5 finder.

7. The η_{max} cut was changed from $\eta_{max} \geq 1.5$ to $\eta_{max} \geq 1.35$ and $\eta_{max} \geq 1.65$

K^0 Selection Cuts

The following systematic changes were calculated for the K^0 analysis.

1. The cut on z separation between the π^+ π^- tracks at the reconstructed secondary vertex was changed from $|\Delta z| \leq 3$ cm to $|\Delta z| \leq 2.7$ cm and $|\Delta z| \leq 3.3$ cm

2. The collinearity angle cut was changed from $\cos\alpha \geq 0.99$ to $\cos\alpha \geq 0.985$ and $\cos\alpha \geq 0.995$

3. The anti-γ cut was changed from $(E_1 + E_2)\theta_{12} > 0.2$ GeV to $(E_1 + E_2)\theta_{12} > 0.18$ GeV and $(E_1 + E_2)\theta_{12} > 0.22$ GeV.

4. The impact parameter cut with which tracks were selected for input to the K^0_s reconstruction algorithm was changed from $|\epsilon| \geq 0.3$ cm to $|\epsilon| \geq 0.27$ cm and $|\epsilon| \geq 0.33$ cm.

5. The anti-Λ cut was changed from $m(p\pi) \leq 1.12$ GeV to $m(p\pi) \leq 1.117$ GeV and $m(p\pi) \leq 1.123$ GeV.

6. The signal, $0.475 - 0.525$ GeV and background regions, $0.4 - 0.45$ and $0.55 - 0.6$ GeV, used to count K^0_s candidates were changed to $0.47 - 0.53$ GeV, $0.44 - 0.47$ and $0.53 - 0.56$ GeV respectively.

Calorimeter Energy Scale

The uncertainty in the UCAL energy scale has been shown to be 5 % [62]. The systematic error associated with this uncertainty was calculated by correcting the data with Monte Carlo samples where each UCAL cell energy deposit had been changed by ± 5 %.

Proton and Photon Structure Functions

The data were corrected using correction factors calculated from the default PYTHIA Monte Carlo sample reweighted by the LAC1 photon structure function. The LAC1 photon structure function contains a large gluon contribution at low x_γ. Similarly, the systematic error associated with the parameterisation of the proton structure function was estimated by correcting events with the default PYTHIA Monte Carlo sample reweighted by the GRV proton structure function.

Track Reconstruction Algorithm

The track reconstruction algorithm used in the default analysis employed information from the VXD, CTD and RTD. The analysis was repeated using only the CTD information for track reconstruction.

6.9 K^0 Multiplicities.

The inclusive multiplicity $\frac{1}{N_{JETS}}\frac{dN(K^0)}{dp_T^2}$ was calculated as a function of p_T using the following procedure. First the reconstructed K_s^0 p_T spectrum was corrected using

$$\frac{dn_{K^0}}{dp_T^2} = \frac{n_{K_s^0}(p_T)}{2p_T \Delta p_T BR}\frac{1}{\epsilon} \tag{6.10}$$

where $n_{K_s^0}(p_T)$ was the number of K_s^0 candidates in the bin p_T to $p_T + \Delta p_T$, $BR = BR(K^0 \rightarrow K_s^0)BR(K_s^0 \rightarrow \pi^+\pi^-)$ which accounts for unseen K^0 decay modes, $\epsilon = \epsilon_{K^0}\epsilon_{trig}C$ is the correction factor.

The observed number of calorimeter jets with $E_T^{UCAL} \geq 7$ GeV and $|\eta| \leq 0.5$ was then corrected to give N_{JETS}, the number of hadron jets with $E_T^{HAD} \geq 8$ GeV

and $|\eta^{HAD}| \leq 0.5$ in events with $0.2 \leq y \leq 0.85$ using a correction procedure similar to that used for K^0_s decays. These numbers were then combined to give the corrected multiplicity, $\frac{1}{N_{JETS}}\frac{dN(K^0)}{dp_T^2}$. A similar procedure was used to calculate $\frac{1}{N_{JETS}}\frac{dN(K^0)}{d\eta}$.

The systematic changes in the K^0 multiplicities after altering a selection cut or reconstruction algorithm are plotted in figures 6.20 and 6.21. The largest systematic error is associated with the choice of track reconstruction algorithm. Using the CTD tracking alone gave a multiplicity higher than using the combined VXD, CTD and RTD tracking. The effect was approximately 12% at low p_T and decreased to 2% at high p_T. As a function of η the tracking package systematic error was 20% at backward η and decreased to 5% at forward η. The largest systematic error associated with event selection was the choice of the region in y_{JB} used to select data events. This gave rise to a 5% error at low p_T which rose to approximately 10% at $p_T = 3.25$ GeV, and an error of approximately 5%, flat in η. Other errors due to the event selection cuts were typically less than 2%. Systematic errors arising from the K^0 selection cuts were typically less than 5%, but in some cases rose to 10% at the lowest and highest η bins. The systematic errors arising from the photon and proton structure functions were found to be typically 5%. The $\pm 5\%$ uncertainty in the calorimeter energy scale gave up to a 10% uncertainty in the inclusive multiplicities.

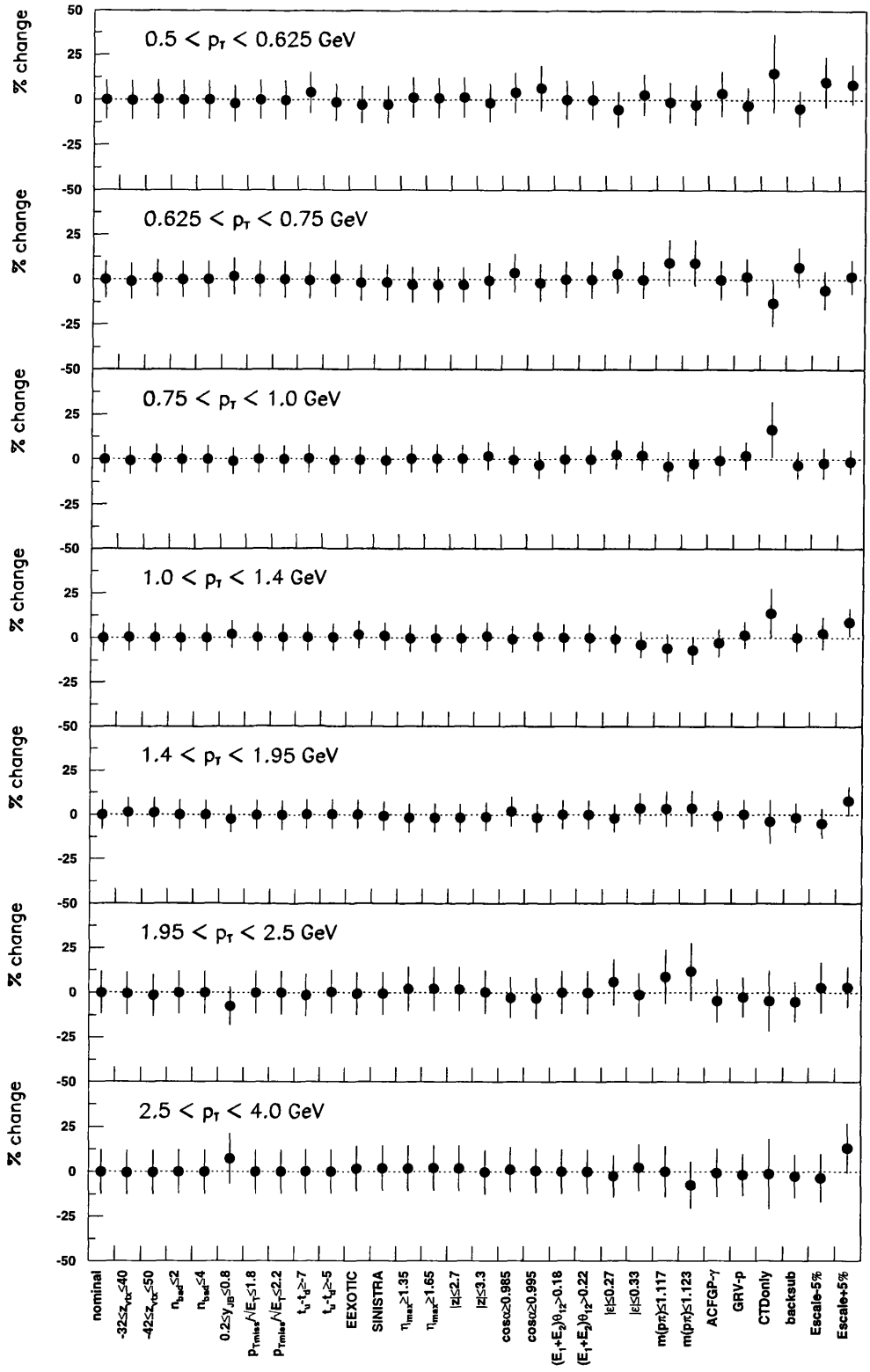

Figure 6.20: Systematic errors in $\frac{1}{N_{JETS}} \frac{dN(K^0)}{dp_T^2}$.

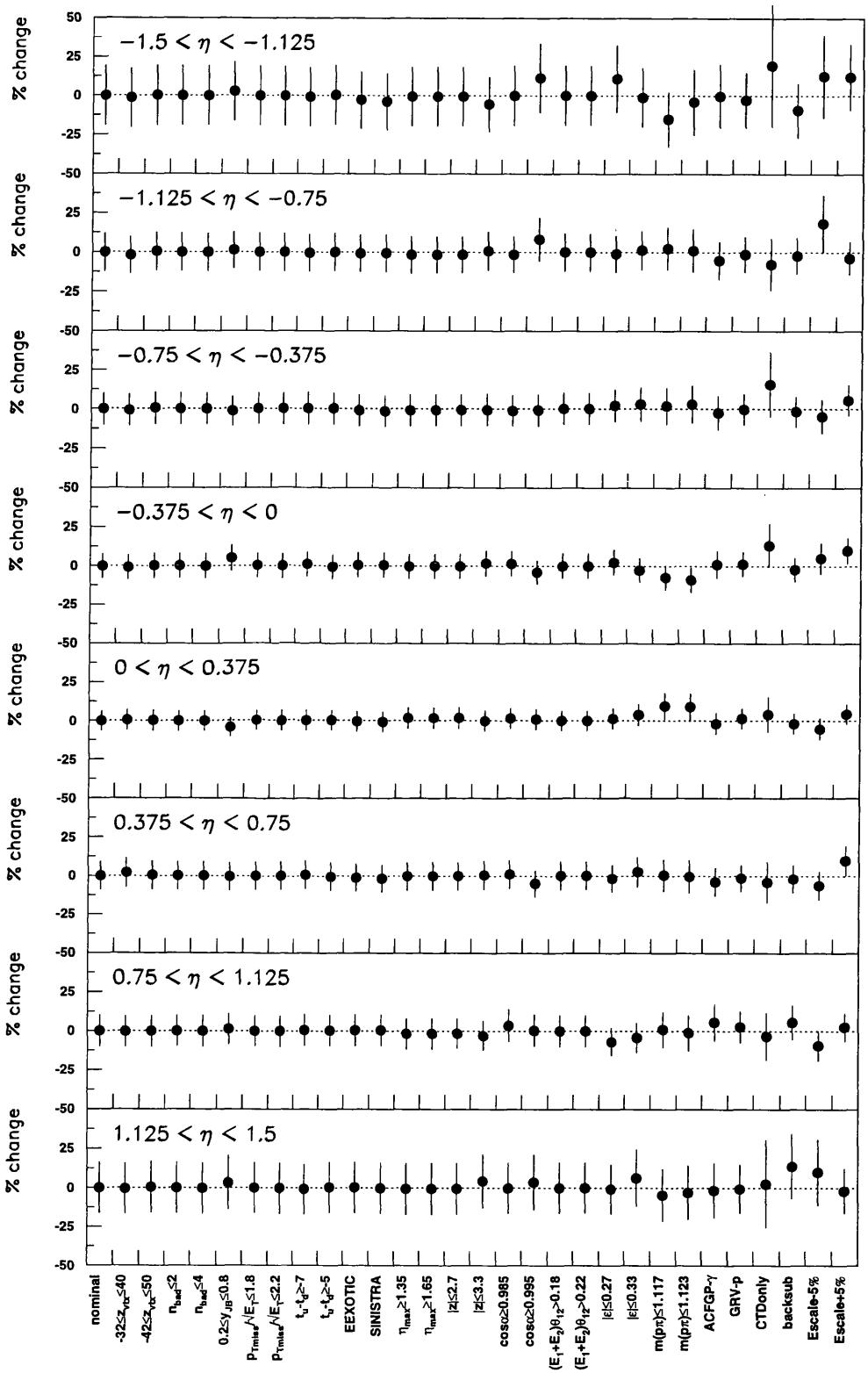

Figure 6.21: Systematic errors in $\frac{1}{N_{JETS}} \frac{dN(K^0)}{d\eta}$.

Figure 6.22 shows $\frac{1}{N_{JETS}}\frac{dN(K^0)}{dp_T^2}$ for hard photoproduction events in the defined kinematic range. The bold error bars denote the statistical error on each point arising from data and Monte Carlo. The thin error bars denote the statistical and systematic errors combined in quadrature. Also shown are the predictions of the default PYTHIA direct, resolved and resolved plus direct Monte Carlo samples, the reweighted LAC1, the $P_s/P_u = 0.20$ PYTHIA and PYTHIA with multiple interaction samples. Both resolved and direct contributions are required to describe the measured cross section. As noted with the uncorrected data, the default resolved plus direct PYTHIA sample is in good agreement with the measured inclusive multiplicity except at low p_T, however, this is probably due to integration over the region, $|\eta(K_s^0)| \leq 1.5$, in which the data contains an excess over the Monte Carlo. As observed in the uncorrected data, PYTHIA with multiple interactions overestimates the K^0 multiplicity at low p_T. The effect of multiple interactions is to increase the overall 'background' energy in an event. This leads to softer jets than in the default case passing the jet E_T threshold, and hence an increase in the multiplicity of soft particles.

Also shown in figure 6.22 is $\frac{1}{N_{JETS}}\frac{dN(K^0)}{d\eta}$ for hard photoproduction events in the defined kinematic range. The bold error bars denote the statistical error on each point arising from data and Monte Carlo. The thin error bars denote the statistical and systematic errors combined in quadrature. As noted with the uncorrected data, the default resolved plus direct PYTHIA sample tends to overestimate the data at low pseudorapidity. Except for PYTHIA with multiple interactions, all the models shown underestimate the K^0 multiplicity at high η, while PYTHIA MI overestimates the K^0 multiplicity at central pseudorapidities. It is interesting to note that at backward pseudorapidities PYTHIA with $P_s/P_u = 0.20$ best models the data.

In [21] it was found that the inclusive jet cross section in hard photoproduction events was larger at high η than all Monte Carlo predictions, except when LAC1 was used as the photon structure function. Since most of the high η kaons will have been produced in jets outside the selection region, $|\eta^{HAD}| < 0.5$, it

is plausible that the K^0 multiplicity excess and the inclusive jet cross section excess arise from a common cause.

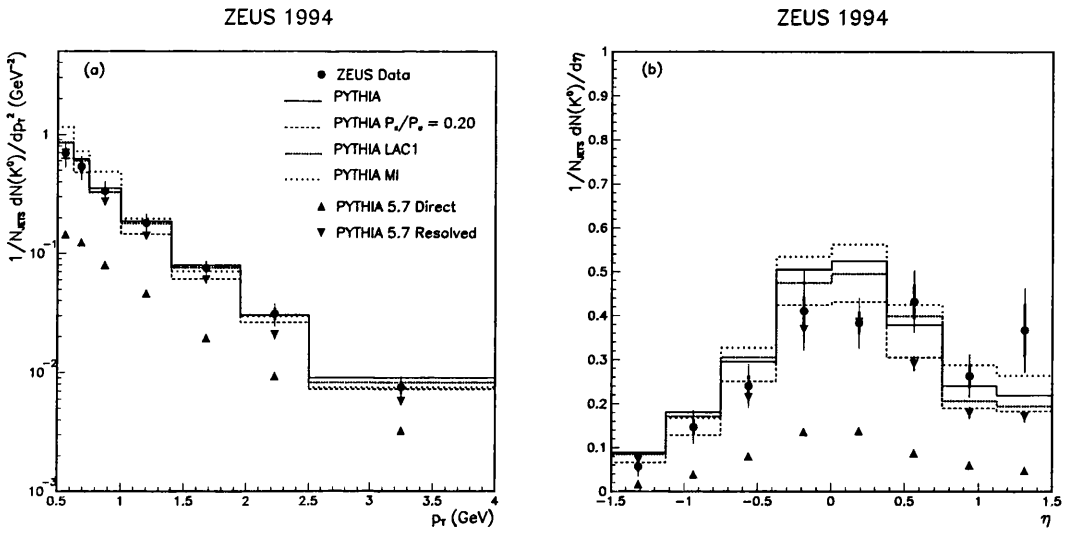

Figure 6.22: Inclusive K^0 multiplicities as a function of p_T, (a), and η, (b), in hard photoproduction events with $0.2 \leq y \leq 0.85$, containing a hadron jet with $E_T^{HAD} \geq 8$ GeV and $|\eta^{HAD}| \leq 0.5$. The data (filled circles) is compared to PYTHIA samples of direct (triangles), resolved (inverted triangles), mixed resolved plus direct (solid line), mixed $P_s/P_u = 0.20$ (dash-dotted line), mixed with the LAC1 resolved plus direct (dotted line), and with multiple interactions (sparse dotted). The bold error bars denote the statistical error on each point arising from data and Monte Carlo. The thin error bars denote the statistical and systematic errors combined in quadrature.

6.10 K^0 Production within Jets.

We have seen that the K^0 η spectrum is only approximately described by the default PYTHIA Monte Carlo, and that the discrepancy arises at forward pseudorapidity. By studying kaons produced in association with the jet(s) satisfying the event selection criteria, $E_T^{UCAL} \geq 7$ GeV in $|\eta^{UCAL}| \leq 0.5$, where the measured inclusive jet cross section is in fair agreement with predictions from PYTHIA [21], jet fragmentation was studied more closely than with the inclusive multiplicity distributions. It was also hoped that problems arising from PYTHIA's inability to describe the K^0 spectrum at forward pseudorapidity would

be avoided. In this section the criteria for associating K_s^0 with jets is established. This is used to calculate the mean K^0 multiplicity per jet, and the fragmentation function into K^0 averaged over all parton flavours.

6.10.1 K^0 - Jet Profiles.

The uncorrected distributions in ϕ and η of K_s^0 relative to jets with $E_T^{UCAL} \geq$ 7 GeV and $|\eta^{UCAL}| \leq 0.5$ are shown in figures 6.23(a) and (b). The K_s^0 were required to satisfy the same kinematic criteria as in the multiplicity measurement, $p_T > 0.5$ GeV, $|\eta| \leq 1.5$. K_s^0 candidates with $\pi^+ \pi^-$ mass in the windows used to perform background subtraction for the inclusive multiplicity measurements have been subtracted from the distributions shown in figures 6.23(a)-(c). The most significant systematic errors in the inclusive K^0 multiplicity spectra were found to be due to the calorimeter energy scale uncertainty and the choice of tracking algorithm. Their effects have been calculated from the data sample. Their systematic errors have been added in quadrature and are shown as the grey bands in figures 6.23(a)-(c).

Peaks at $\Delta\phi \approx 0$ and $\Delta\phi \approx \pm\pi$ in figure 6.23(a) suggest that K_s^0 are being produced in association with jets, since momentum conservation means the two jets produced in typical photoproduction events occur at opposite ϕ. PYTHIA predicts a narrower distribution of K_s^0 within jets, and a slightly lower multiplicity in the wings of the profile than is observed in the data. For K_s^0 jet pairs with $\Delta\phi < \frac{\pi}{2}$, the corresponding profile in η is shown in figure 6.23(b). As with the azimuthal profile, the data and PYTHIA agree well in the wings of the jet, but PYTHIA predicts a narrower distribution than is observed within the jet at $\Delta\eta \approx 0$. The K_s^0 - jet profile prediction from PYTHIA with multiple interactions is broader than the default PYTHIA prediction, but it also overestimates the data. As noted earlier, this is due to the increased 'background' energy in multiple interaction events, leading to softer jets passing the E_T threshold, and manifests itself as a higher pedestal in the K_s^0 - jet profiles.

The distance in $\eta - \phi$ space between a K_s^0 and a jet, $R = \sqrt{\Delta\eta^2 + \Delta\phi^2}$, is

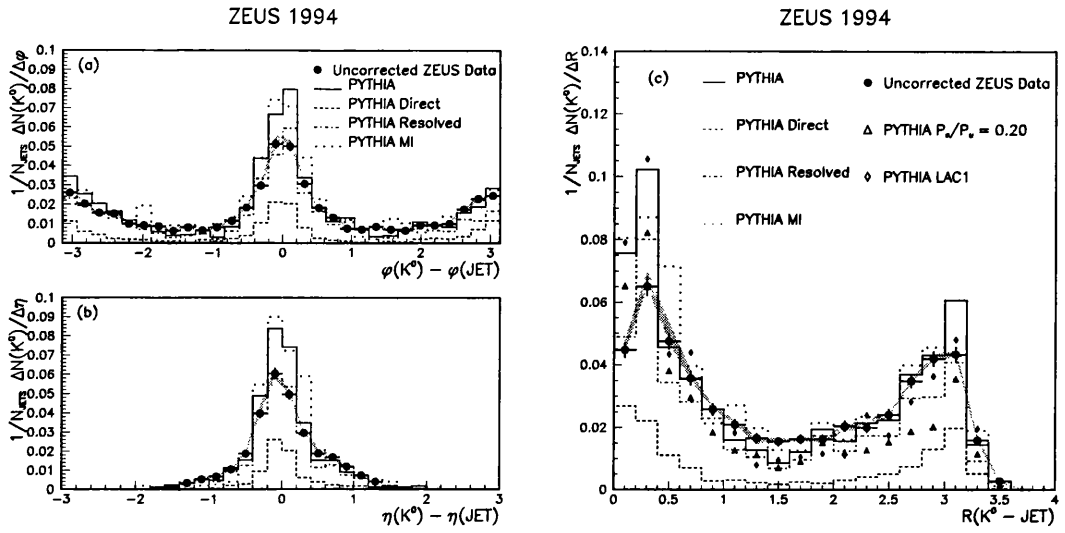

Figure 6.23: Uncorrected distributions of K^0_s with respect to calorimeter jets of $E_T^{UCAL} \geq$ 7 GeV and $|\eta^{UCAL}| \leq 0.5$ in ϕ (a), η (b) and R (c). The data (filled circles) is compared to PYTHIA distributions of direct (dashed-line), resolved (dash-dotted line) and resolved plus direct (solid line) mixed according to the Monte Carlo cross section, in all plots. The direct and resolved Monte Carlo distributions have been normalised to show the fraction of the K^0 multiplicity arising from the direct and resolved processes respectively. In (c) the data is also compared with the mixed $P_s/P_u = 0.20$ (triangles), and LAC1 resolved plus direct (diamonds) PYTHIA samples. The grey band represents the systematic error due to the systematic errors associated with the calorimeter energy scale uncertainty and track reconstruction method.

shown in figure 6.23(c). A pronounced peak at small values of R demonstrates that K^0_s are being produced in association with jets. For $R < 0.5$ PYTHIA predicts an excess over the data but is in good agreement with the data for $0.5 < R < 1$. In the inter-jet range, $1 < R < 2$, PYTHIA underestimates the data. This is partially associated with the high η K^0_s excess in the data observed in figure 6.15 as the description of the inter-jet region improves if the R distribution is plotted using kaons with $\eta < 0.5$. The effect of the excess is less apparent in figure 6.23(c) than in figure 6.22(b), since figure 6.23(c) is an uncorrected plot and also because of the low K^0_s reconstruction efficiency at high pseudorapidity.

To establish if the deficit of K^0_s within the jet core was due to poorly understood tracking in the jet core, the K^0_s - jet profiles were made for jets containing a varying number of charged particles (ie. contained within $R < 1$

and assigned to the primary vertex). Figure 6.24 shows that the discrepancy remained even when only one or two charged particles were contained in the jet. As will be shown in chapter 7, the average number of such charged particles contained in a jet was approximately 3. It therefore seems unlikely that the discrepancy can be explained by a track reconstruction efficiency problem in the detector simulation.

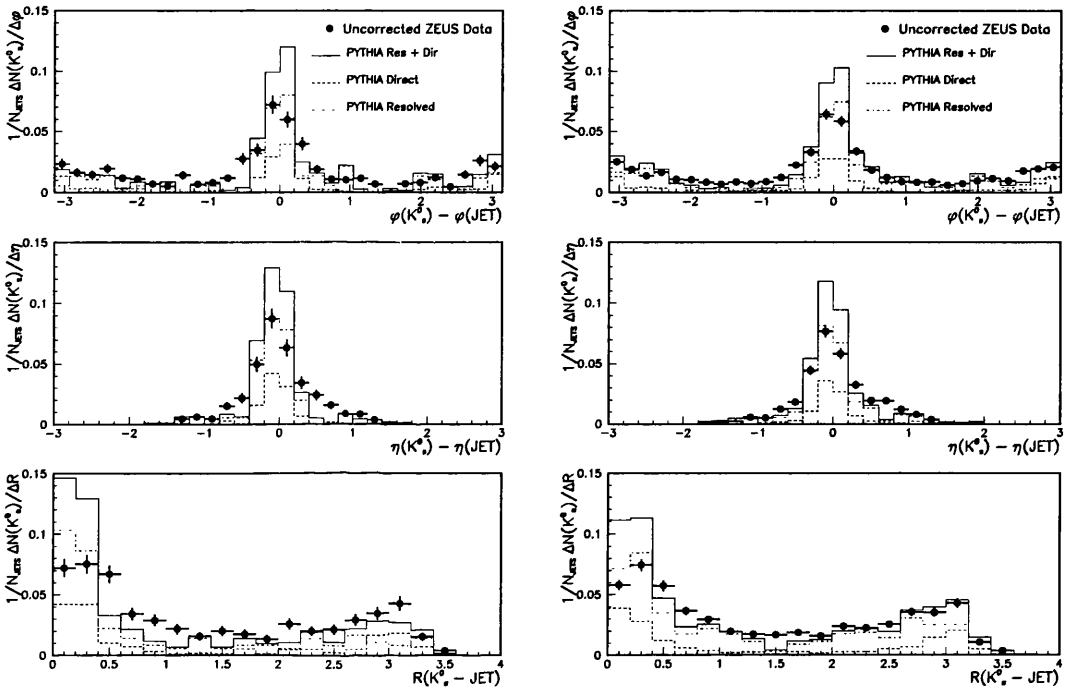

Figure 6.24: Uncorrected distributions of K^0_s with respect to calorimeter jets of $E_T^{UCAL} \geq$ 7 GeV and $|\eta^{UCAL}| \leq 0.5$ for jets with only one track (left) and at most two charged particles (right) associated with the primary vertex as functions of ϕ (top), η (middle) and R (bottom). The data (filled circles) is compared to PYTHIA distributions of direct (dashed-line), resolved (dash-dotted line) and resolved plus direct (solid line) mixed according to the Monte Carlo cross section, in all plots. The direct and resolved Monte Carlo distributions have been normalised to show the fraction of the K^0 multiplicity arising from the direct and resolved processes respectively.

Changing the photon structure functions to the ACFGP, GRV NLO and GS2 parametrisations also failed to adequately describe the data for $R < 0.5$. The discrepancy also exists in the default PYTHIA sample of direct enriched

photoproduction events shown in figure 6.25, while the $P_s/P_u = 0.20$ PYTHIA sample provides a good description of the data for $R < 1$. These were selected by requiring events to have two or more jets with $E_T^{UCAL} \geq 7$ GeV, $|\eta^{UCAL}| \leq 0.5$ and $x_\gamma^{OBS} \geq 0.75$ for the two highest E_T jets, as in [72]. The x_γ^{OBS} spectra in data and Monte Carlo events are shown in figure 6.26. The Monte Carlo has been mixed to provide the best fit of the x_γ^{OBS} distribution in the data. In figure 6.25 the Monte Carlo direct and resolved events were mixed in proportion to the fraction of events with $x_\gamma^{OBS} \geq 0.75$. Removing events from the Monte Carlo which were initiated by charm quarks in the photon, in order to reduce the number of K_s^0 from charmed particle decays, did not alleviate the discrepancy.

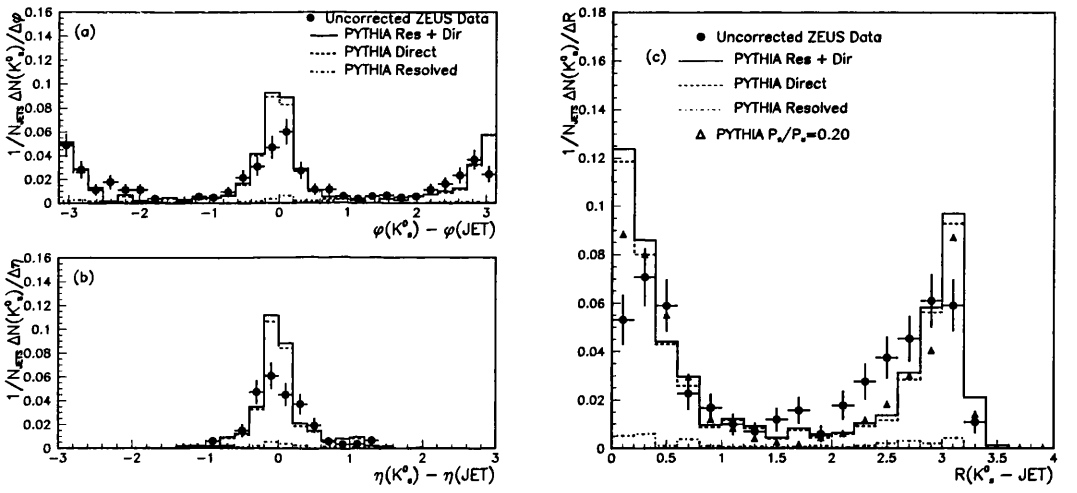

Figure 6.25: Uncorrected distributions of K_s^0 with respect to calorimeter jets of $E_T^{UCAL} \geq 7$ GeV and $|\eta^{UCAL}| \leq 0.5$ as functions of ϕ (a), η (b) and R (c) in a sample of direct enriched events selected as described in the text. The data (filled circles) is compared to PYTHIA distributions of direct (dashed-line), resolved (dash-dotted line), resolved plus direct (solid line), and $P_s/P_u = 0.2$ mixed according to the fraction of events with $x_\gamma^{OBS} \geq 0.75$. The direct and resolved Monte Carlo distributions have been normalised to show the fraction of the K^0 multiplicity arising from the direct and resolved processes respectively.

The PYTHIA sample generated with $P_s/P_u = 0.20$ shows a reduction in the numbers of K_s^0 over the measured phase space. So while agreement is improved between data and PYTHIA with $P_s/P_u = 0.2$ in the jet core ($R < 0.5$), the previous agreement at $0.5 < R < 1$ is lost and the discrepancy at $R > 1$ worsens.

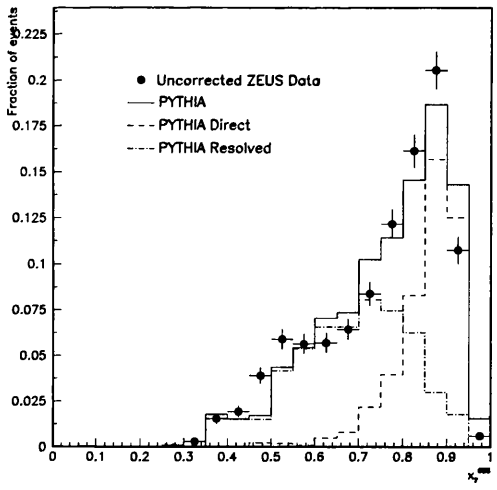

Figure 6.26: Uncorrected x_γ^{OBS} distributions of events with $0.15 \leq y_{JB} \leq 0.7$ and at least two jets jets satisfying $E_T^{UCAL} \geq 7$ GeV and $|\eta^{UCAL}| \leq 0.5$. The data (filled circles) is compared to PYTHIA distributions of direct (dashed-line), resolved (dash-dotted line) and resolved plus direct (solid line) mixed to give the best fit to the data.

6.10.2 K^0 Multiplicity per Jet

The differences between the K^0 production rates in the data and Monte Carlo models has been quantified by measuring the K^0 multiplicity per jet. To measure this we defined the criterion for associating a K_s^0 with a jet to be, $R(K_s^0 - JET) < 1$. The K^0 multiplicity per jet $< n_{K^0/JET} >$ was then calculated as

$$< n_{K^0/JET} >= \frac{n_{K_s^0}}{n_{JETS}} \frac{1}{BR} \tag{6.11}$$

where $n_{K_s^0}$ was the number of K_s^0 assigned to a calorimeter jet, n_{JETS} was the number of calorimeter jets in each η^{UCAL} bin, and BR is the total branching ratio for $K^0 \rightarrow \pi^+\pi^-$. The number of K_s^0 in each $\eta^{JET} = \eta^{UCAL}$ bin was calculated using the background subtraction technique of section 6.4. The uncorrected K^0 multiplicity per jet is shown in figure 6.27, where it is observed that the shapes of the data and PYTHIA are in good agreement.

The total correction factors for the separate direct, resolved, and resolved plus direct PYTHIA Monte Carlo samples are shown in figure 6.28. The correction

factors are flat as a function of η^{JET} with a magnitude principally determined by the efficiency of the K^0 reconstruction.

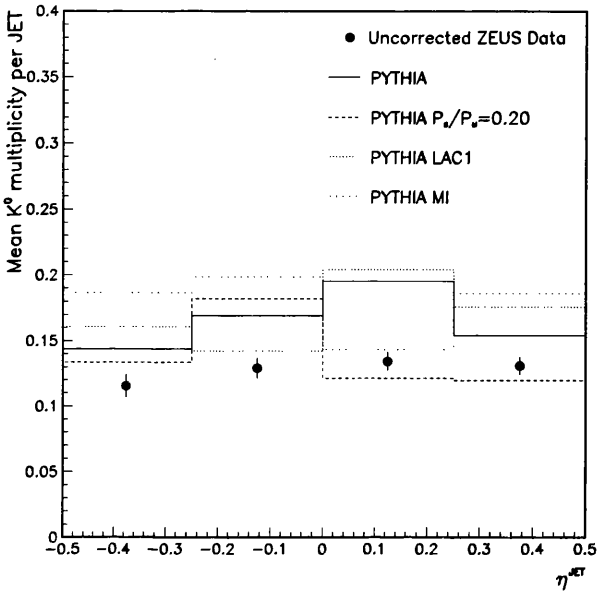

Figure 6.27: Uncorrected K^0 multiplicity per jet as a function of η^{JET}. The data (filled circles) is compared to distributions of the mixed resolved plus direct default PYTHIA sample (solid line), the $P_s/P_u = 0.20$ mixed PYTHIA sample (dashed line), the LAC1 resolved plus direct PYTHIA sample (dotted line) and the PYTHIA multiple interaction sample (scarce dotted).

As for the K^0 multiplicities the largest systematic error associated with event selection is due to the y_{JB} region from which the data is selected and is typically 5%. The systematic error from the K^0 selection cuts was 10% in the lowest and highest η^{JET} bins dominated by the background subtraction method and 5% in the central η^{JET} bins due to the Λ rejection cut. The dominant systematic error is due to the difference between the VXD, CTD plus RTD and CTD only track reconstruction algorithms. The systematic error due to CTD tracking information is less than 10% at low η and between 10 and 20% at positive η. The effect of the UCAL energy scale uncertainty on the number of K^0s and jets was expected to cancel in the K^0 multiplicity per jet, since it is a ratio. The systematic error arising from the UCAL energy scale uncertainty is typically 5% in all η^{JET} bins.

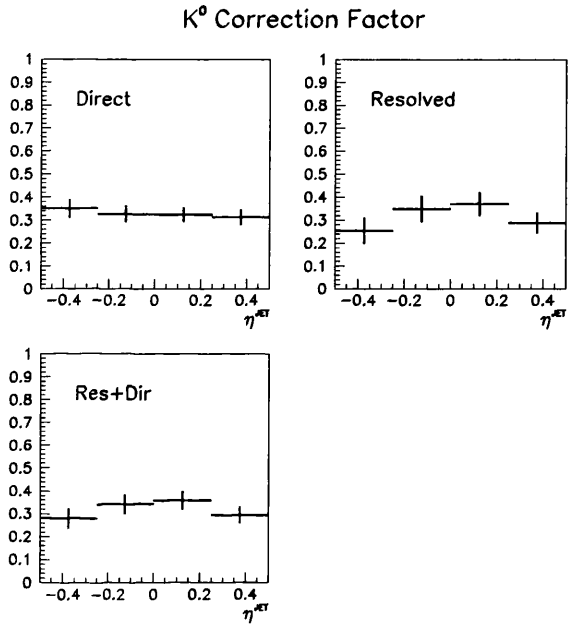

Figure 6.28: K^0 multiplicity per jet correction factor as a function of η^{JET} for direct (top left), resolved (top right) and mixed resolved plus direct (bottom left) PYTHIA Monte Carlo samples.

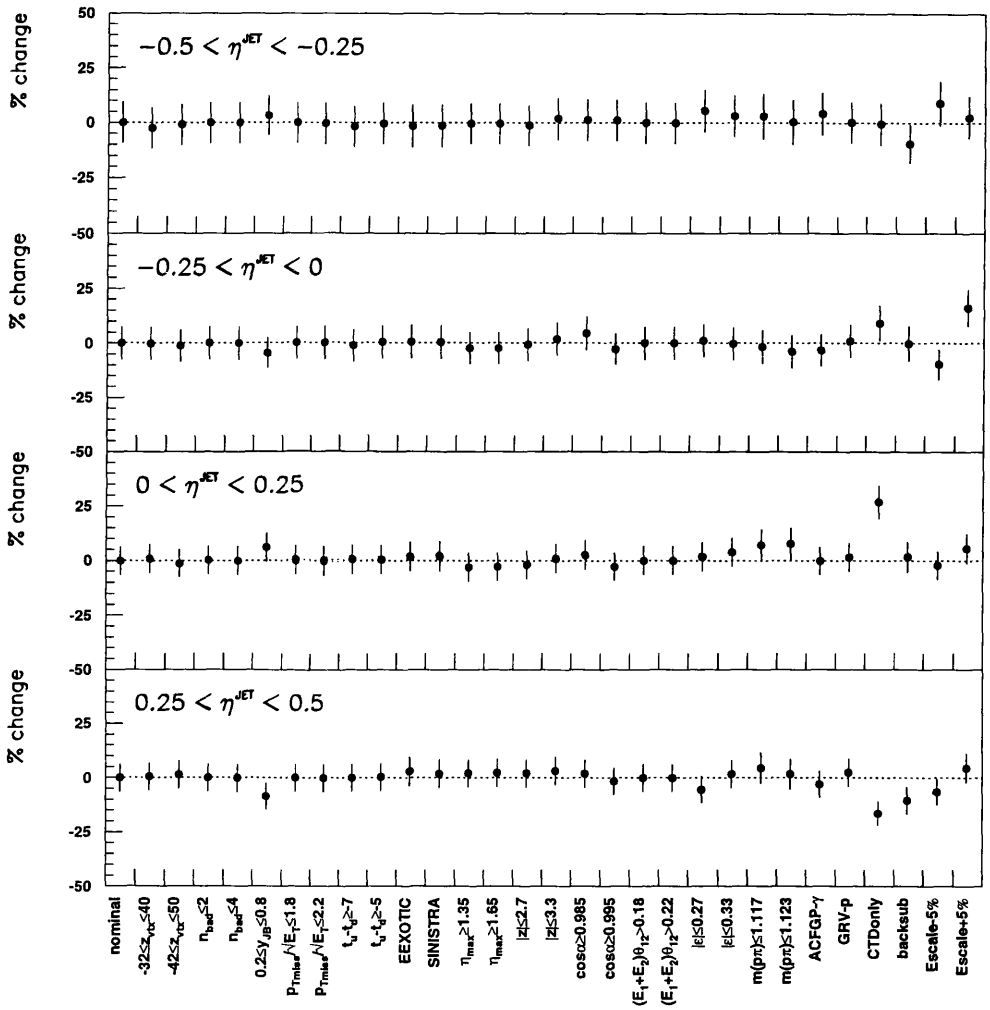

Figure 6.29: Systematic errors in $< n_{K^0/JET} >$.

The corrected K^0 multiplicity per jet, for jets with $E_T^{HAD} > 8$ GeV and $|\eta^{HAD}| < 0.5$, is shown in figure 6.30. The jet pseudorapidity was shown to be accurately reconstructed in section 5.2 so $\eta^{HAD} = \eta^{JET} = \eta^{UCAL}$. The bold error bars denote the statistical error on each point arising from data and Monte Carlo. The thin error bars denote the statistical and systematic errors combined in quadrature. Both data and Monte Carlo predictions appear to be independent of jet pseudorapidity. Integrating over the region $|\eta^{HAD}| \leq 0.5$ the mean K^0 multiplicity per jet was found to be, $< n_{K^0/JET} >= 0.40 \pm 0.01^{+0.03}_{-0.02}$ where the first error is statistical and the second error is systematic. For PYTHIA with the strangeness suppression factor $P_s/P_u = 0.3$ using the GRV LHO photon and MRSA proton structure functions, one obtains $< n_{K^0/JET} >= 0.52 \pm 0.01$, while PYTHIA with multiple interactions predicts $< n_{K^0/JET} >= 0.56 \pm 0.01$, both overestimating the measured rate. Varying the photon structure function had little effect on $< n_{K^0/JET} >$. The PYTHIA prediction with $P_s/P_u = 0.2$ is $< n_{K^0/JET} >= 0.43 \pm 0.01$ in good agreement with the measured value.

6.10.3 K^0 Fragmentation Function

For K_s^0 assigned to jets as in section 6.10.2, the longitudinal momentum fraction of the jet carried by the K^0 was calculated according to the definition,

$$z = \frac{p_{K_s^0} \cdot p_{JET}}{E_{JET}^2} \tag{6.12}$$

where $p_{K_s^0}$ was the 3-momentum of the K_s^0, and p_{JET} and E_{JET} the 3-momentum and energy of the jet to which the K_s^0 was assigned. The uncorrected K^0 fragmentation function was then calculated from

$$D^{K^0}(z) = \frac{n_{K_s^0}(z)}{N_{JETS}} \frac{1}{\Delta z BR} \tag{6.13}$$

where N_{JETS} is the total number of calorimeter jets with $E_T^{UCAL} \geq 7$ GeV and $|\eta^{UCAL}| \leq 0.5$, $n_{K_s^0}(z)$ was the number of K_s^0 candidates with $p_T \geq 0.5$ GeV, $|\eta| \leq 1.5$ and in the jet momentum fraction range z to $z + \Delta z$ calculated using the background subtraction technique of section 6.4. BR is the total branching fraction for $K^0 \rightarrow \pi^+\pi^-$.

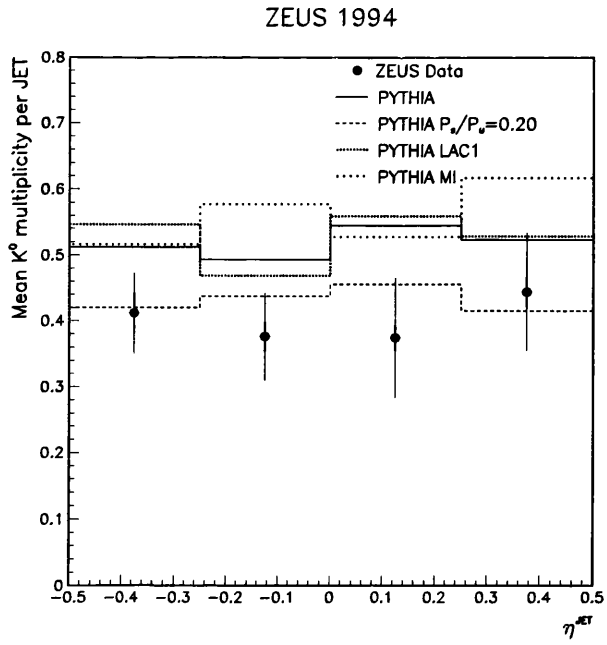

Figure 6.30: K^0 multiplicity per jet as a function of η^{JET} in hard photoproduction events with $0.2 \leq y \leq 0.85$, containing jets with $E_T^{HAD} \geq 8$ GeV and $|\eta^{HAD}| \leq 0.5$. The data (filled circles) is compared to distributions of the mixed resolved plus direct default PYTHIA sample (solid line), the $P_s/P_u = 0.20$ mixed PYTHIA sample (dashed line), the LAC1 resolved plus direct PYTHIA sample (dotted line) and the PYTHIA multiple interaction sample (scarce dotted).

The uncorrected K_s^0 fragmentation function is shown in figure 6.31. There is good general agreement between the uncorrected data and PYTHIA Monte Carlo predictions. The data and Monte Carlo points are plotted at the mean z value within each bin. The shape of the fragmentation function in the Monte Carlo and data at $z < 0.05$ is affected by the requirement that $p_T(K_s^0) \geq 0.5$ GeV.

The accuracy and resolution of the reconstructed K_s^0 jet momentum fraction is shown in figure 6.32 by calculating $z_{reco} - z_{true}$. There is a small shift of $+0.02$ in the reconstructed jet momentum fraction relative to the true jet momentum fraction. A shift in the reconstructed jet momentum fraction is expected because the jet energy measured by the UCAL is lower than the true value because of effects described in section 5.2, while the tracking provides a K_s^0 momentum measurement free of any such bias.

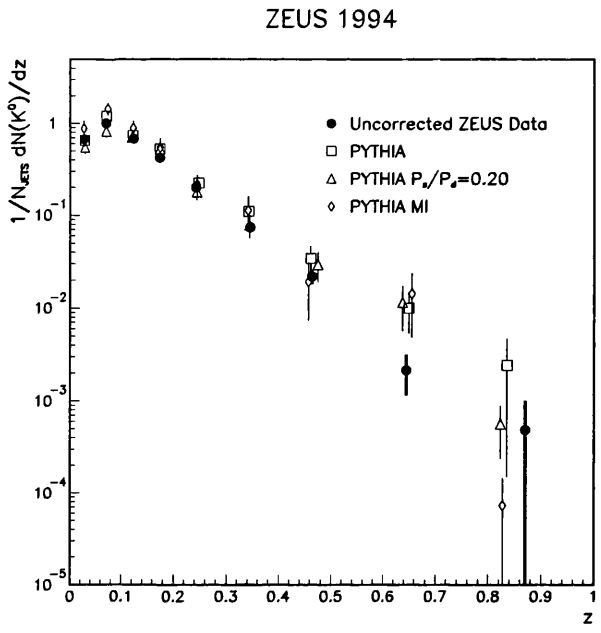

Figure 6.31: Uncorrected K^0 fragmentation function. The data (filled circles) is compared to distributions of the mixed resolved plus direct default PYTHIA sample (open squares), the $P_s/P_u = 0.20$ mixed PYTHIA sample (open triangles) and PYTHIA with multiple interactions (open diamonds).

The shift in the reconstructed jet momentum fraction was proportional to the true jet momentum fraction, as shown in figure 6.32. Applying a 10 % reduction to the reconstructed jet momentum fraction gave the momentum fraction resolution shown in figure 6.33 which shows a negligible shift. The difference in the K^0 fragmentation function calculated with and without correcting the jet momentum fraction carried by the K^0_s for the CTD-UCAL energy scale difference is included in the systematic error evaluation.

A bin-by-bin correction procedure for determining the corrected K^0 fragmentation function in events containing a hadron jet with $E_T^{HAD} \geq 8$ GeV, $|\eta^{HAD}| \leq 0.5$ as discussed in section 6.6 was applied. The total correction factors for the separate direct, resolved and resolved plus direct PYTHIA Monte Carlo samples are shown in figure 6.34.

The systematic errors due to event selection cuts were typically less than 5% in any bin except for high z where the y_{JB} systematic error reached 40%. The

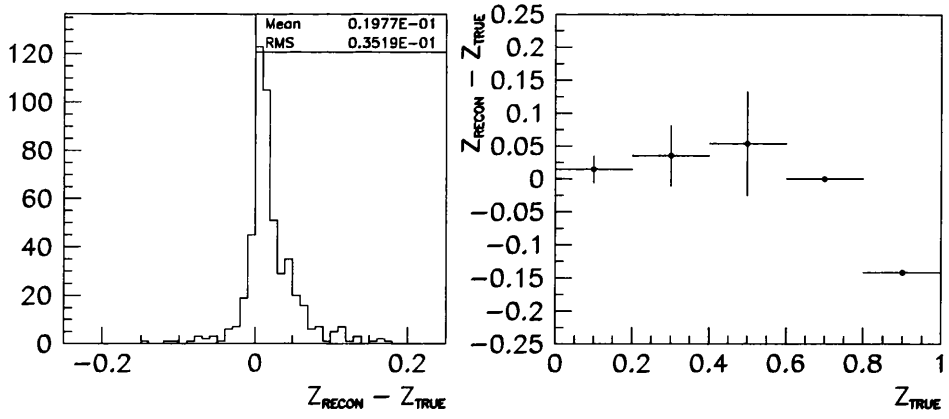

Figure 6.32: The jet momentum fraction resolution (left) and jet momentum fraction resolution as a function of true jet momentum fraction (right) without taking into account the energy scale difference between the tracking and UCAL.

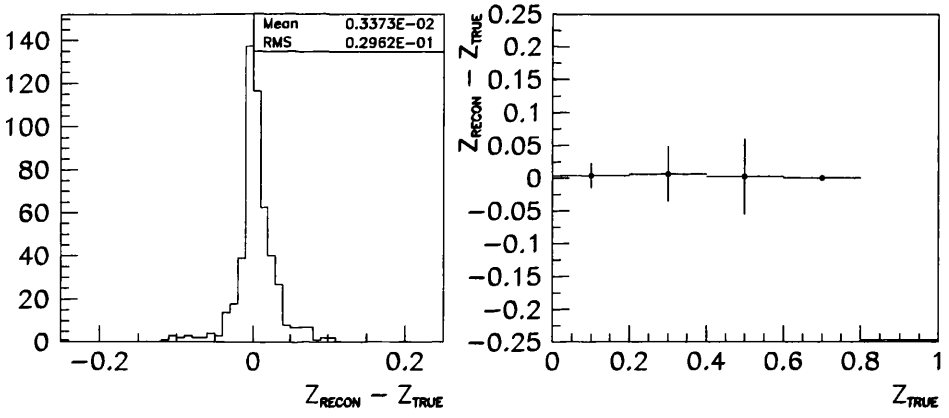

Figure 6.33: The jet momentum fraction resolution (left) and jet momentum fraction resolution as a function of true jet momentum fraction (right) taking into account the energy scale difference between the tracking and UCAL.

systematic errors due to the K^0 selection cuts were typically less than 5% up to $z < 0.3$. At high z the impact parameter cut and Λ rejection cut were the dominant systematic errors, of the order of 15-20%. The Λ rejection systematic error in the final z bin was 1000%, this was due to statistical fluctuations.

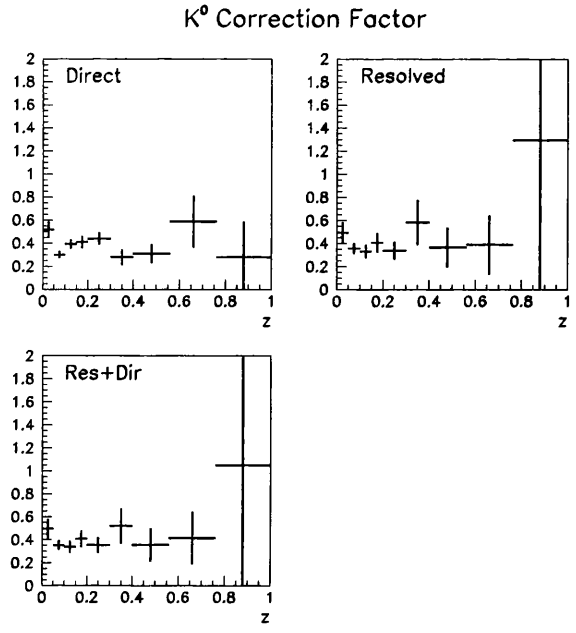

Figure 6.34: K^0 fragmentation function correction factors as a function of z for direct (top left), resolved (top right) and mixed resolved plus direct (bottom left) PYTHIA Monte Carlo samples.

The systematic error from correcting the data with different photon and proton structure functions was typically less than 5% but reached 20% at high z. The track reconstruction algorithm was found to be the dominant systematic error at low z contributing at most 75%, but typically 15 - 40%. The systematic error arising from the uncertainty in the calorimeter energy was less than 5% at low z and increased to 30% in the final z bin. Correcting the calculated jet momentum fraction for the difference in energy scale between the CTD and UCAL produced an uncertainty of typically 5% which increased to 30% at high z.

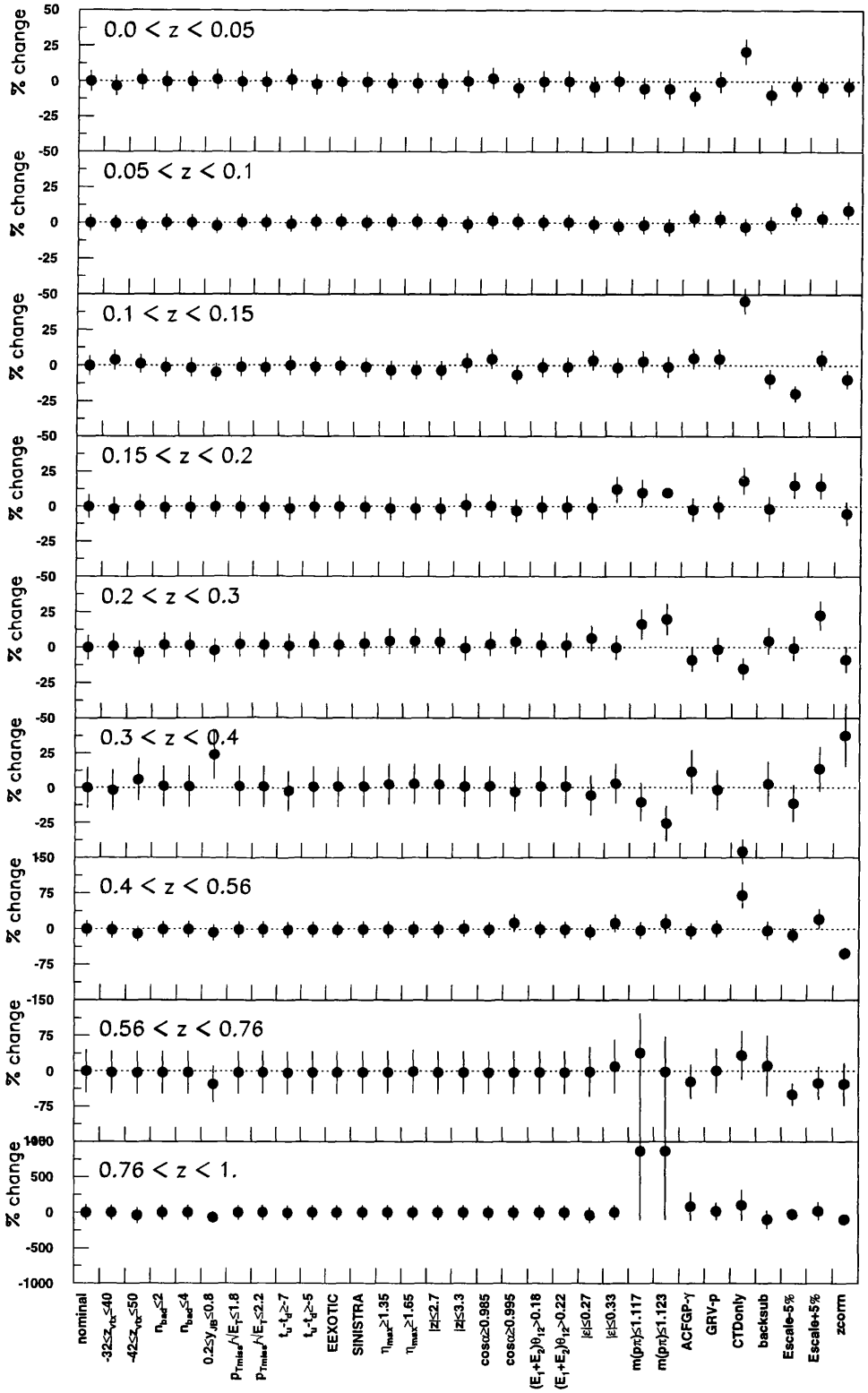

Figure 6.35: Systematic errors in $D^{K^0}(z)$.

The corrected K^0 fragmentation function is compared to the predictions of the default, $P_s/P_u = 0.20$ and multiple interaction PYTHIA Monte Carlo samples in figure 6.36. The data and Monte Carlo points are plotted at the mean z value within each bin, without taking into account any shift in z arising from the CTD-UCAL energy scale difference. The bold error bars denote the statistical error on each point arising from data and Monte Carlo. The thin error bars denote the statistical and systematic errors combined in quadrature. The results from Binnewies et al. [2] are shown as the two curves. The flavour of the scattered partons is not known and the choice of LO and NLO is not well defined in the present context. The curves represent the limits of the range of LO and NLO $D^{K^0}(z)$ values at a scale of 8 GeV. The lower curve corresponds to NLO g fragmentation for $z < 0.45$ and d quark fragmentation for $z > 0.45$. The upper curve corresponds to LO d, c and u quark fragmentation for $z < 0.15$, $0.15 < z < 0.40$ and $z > 0.40$ respectively. The data lies between PYTHIA with default fragmentation parameters and $P_s/P_u = 0.20$ at $z < 0.3$, while there is a tendency for the data to lie below both PYTHIA samples at $z > 0.3$. Similar conclusions are reached when comparing the data with the results of [2].

The definition of z used in the fragmentation function measurement was slightly different from that used by Binnewies et al. In their calculation, z had been defined by the e^+ e^- experiments which they used to calculate their fragmentation functions. The fragmentation function analysis presented in this thesis was repeated using the corresponding definition,

$$z' = \frac{E_{K^0}}{E_{JET}} \tag{6.14}$$

to investigate the effect of the z definition. The resulting fragmentation function, $D^{K^0}(z')$, is shown in figure 6.37, where it is compared to the the results of [2] and the fragmentation function, $D^{K^0}(z)$, determined using $z = \frac{p_{K^0_s} \cdot p_{JET}}{E^2_{JET}}$. The error bars on the data points represent the systematic errors added in quadrature, calculated in the same manner as before. One expects $z' > z$ since $z \sim z' \cos\theta$, where θ is the angle between a kaon and the jet to which it is assigned and therefore the maximum of $D^{K^0}(z')$ occurs at $z' = 0.12$ while the maximum of

$D^{K^0}(z)$ was at $z = 0.07$. The error on the point at $z' = 0.04$ is so large because of the $p_T(K^0_s) \geq 0.5$ GeV cut. The agreement between data and the calculations of Binnewies et al. is improved by using the momentum fraction defined according to z'.

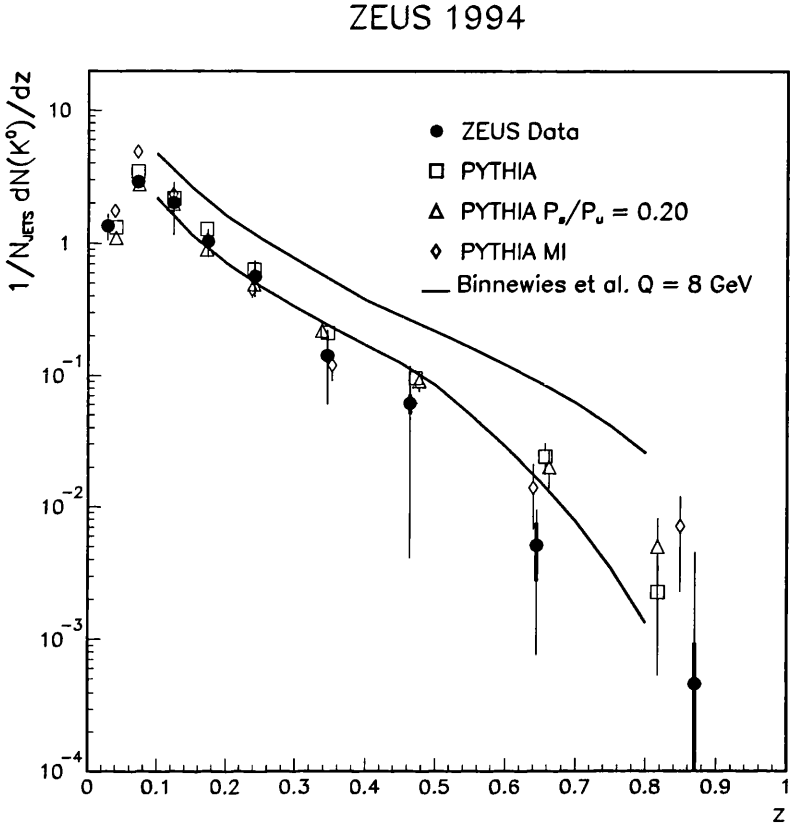

Figure 6.36: The K^0 fragmentation function in hard photoproduction events with $0.2 \leq y \leq 0.85$, containing jets with $E_T^{HAD} \geq 8$ GeV and $|\eta^{HAD}| \leq 0.5$. The data (filled circles) is compared to distributions of the mixed resolved plus direct default PYTHIA sample (open squares), the $P_s/P_u = 0.20$ mixed PYTHIA sample (open triangles) and PYTHIA with multiple interactions (open diamonds). The range covered by the prediction of [2] lies between the solid lines.

6.11 Summary Of K^0 Results

As stated in section 6.9, $\frac{1}{N_{JETS}} \frac{dN(K^0)}{dp_T^2}$ is well described by the default resolved plus direct PYTHIA sample. However, the $\frac{1}{N_{JETS}} \frac{dN(K^0)}{d\eta}$ measurement shows that

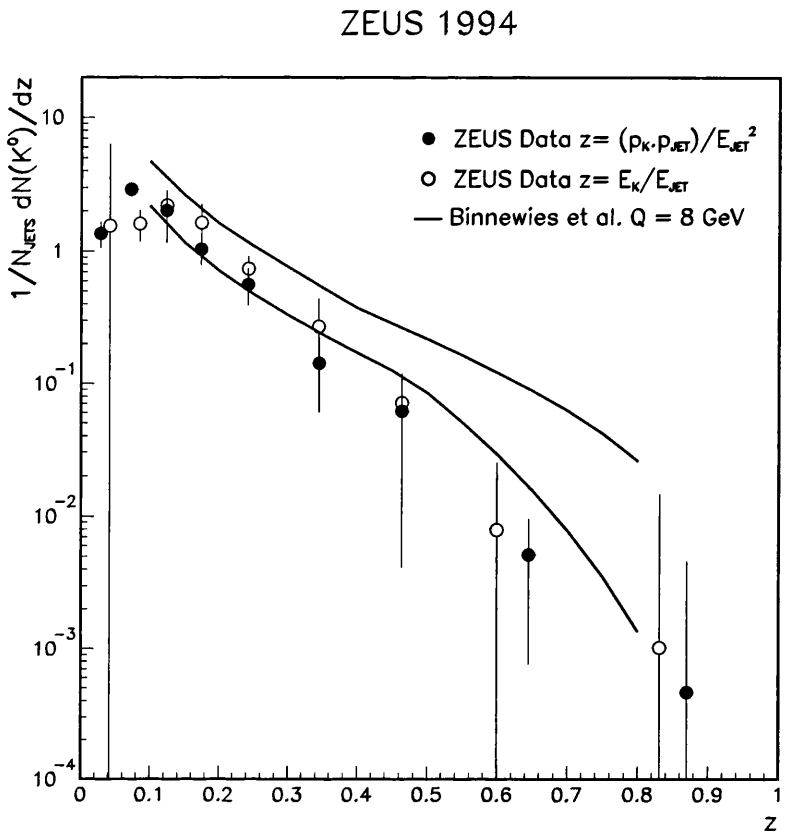

Figure 6.37: The K^0 fragmentation function in hard photoproduction events with $0.2 \leq y \leq 0.85$, containing jets with $E_T^{HAD} \geq 8$ GeV and $|\eta^{HAD}| \leq 0.5$. The result obtained using the definition $z' = \frac{E_{K^0}}{E_{JET}}$ (open circles) is compared with the range covered by the prediction of [2]. The result obtained using the definition $z = \frac{p_{K^0_s} \cdot p_{JET}}{E^2_{JET}}$ is depicted by the filled circles.

PYTHIA achieves this by overestimating the K^0 multiplicity at backward pseudo-rapidities and underestimating the K^0 multiplicity at $\eta > 0.5$. The $\frac{1}{N_{JETS}} \frac{dN(K^0)}{d\eta}$ distribution at $\eta < 0.5$ is modelled better by PYTHIA with $P_s/P_u = 0.20$, while PYTHIA with multiple interactions provides the best description of the data at $\eta > 0.75$.

The uncorrected distributions of kaons relative to jets in ϕ, η and R all show that the default PYTHIA Monte Carlo predicts narrower jets than is observed in the data. The difference in jet shape between the data and PYTHIA is not attributable to a problem with the track reconstruction efficiency in the detector simulation, and is not solved by changing the photon structure function.

Integrating over the region $|\eta^{HAD}| \leq 0.5$ the mean K^0 multiplicity per jet was found to be, $< n_{K^0/JET} >= 0.40 \pm 0.01\ ^{+0.03}_{-0.02}$. The K^0 multiplicity per jet is overestimated by the default PYTHIA and PYTHIA with multiple interactions. PYTHIA with $P_s/P_u = 0.2$ provides the best description of the K^0 multiplicity per jet.

There is good agreement between the K^0 fragmentation function measured in the data and predicted by the default and $P_s/P_u = 0.20$ PYTHIA Monte Carlo samples, while PYTHIA with multiple interactions predicts a softer fragmentation function than is observed in the data. The data and results of [2] are in good agreement.

Chapter 7

Charged Particle Analysis

The previous chapter has shown that PYTHIA predicts a larger production rate of strange mesons than in the hard photoproduction data. This stems from the poor description of the jet shape provided by JETSET with default hadronisation parameters. An analysis of charged particle production analogous to the K^0 analysis has been made in order to determine if the conclusions are peculiar to K^0 production, or are general properties of hard photoproduction events.

7.1 Charged Particle Selection

As for the K^0 analysis, charged particles with $p_T > 500$ MeV and $|\eta| < 1.5$ associated with the primary vertex were used in this analysis. The pseudorapidity of charged particles was calculated from their fit parameters at the primary vertex. The CTD acceptance and systematics are well understood in this region since such tracks leave the CTD without completing a loop of the helix and therefore do not suffer splitting effects which occur when reconstructing low p_T tracks.

The reconstructed charged particle data was corrected with, and compared to, 'true' charged particles generated by PYTHIA in the same p_T and η region as the reconstructed particles. The true charged particles were either,

- A stable charged particle generated at the primary vertex, or,

- A daughter of a particle with lifetime $\tau < 10^{-8}$ s, or,
- A $K^{\pm}$ or $\pi^{\pm}$ generated at the primary vertex, which decayed weakly (but not their daughters).

Thus, decay products of K^0 and Λ were not included in the 'true' distributions. This is in contrast with the data which was used in the derivation of fragmentation functions by Binnewies [1], where daughters of K_s^0 and Λ decay were included in the true charged particle distributions. The reconstructed charged particle distributions were corrected back to the true distributions using the same method and Monte Carlo sample as the K^0 analysis.

7.2 Uncorrected Charged Particle Inclusive Multiplicities

The uncorrected charged particle inclusive multiplicities as a function of p_T and η in hard photoproduction events with $0.15 \leq y_{JB} \leq 0.7$, containing a calorimeter jet with $E_T^{UCAL} \geq 7$ GeV and $|\eta^{UCAL}| \leq 0.5$ are shown in figures 7.1(a) and (b) respectively. The default, the $P_s/P_u = 0.20$ and the LAC1 PYTHIA resolved plus direct samples all describe the uncorrected $\frac{1}{N_{JETS}} \frac{dN(h^{\pm})}{dp_T^2}$ spectrum well. As noted in the K^0 analysis, PYTHIA with multiple interactions overestimates the charged particle multiplicity at low p_T

As in the K^0 analysis, there is some difference between the shape of the uncorrected $\frac{1}{N_{JETS}} \frac{dN(h^{\pm})}{d\eta}$ inclusive multiplicity in the data and predicted by PYTHIA. For $\eta \leq 0.75$ the shapes of the data and PYTHIA agree to within ± 10 %, but the data shows a 20 % excess at $\eta > 0.75$. Since this effect occurs at forward pseudorapidity, it is plausible that it originates from the same cause as the K^0 and inclusive jet cross section excess observed in [21]. The prediction of PYTHIA with multiple interactions is in better agreement with the data at $\eta \geq 0.75$, however it overestimates the charged particle multiplicity at central pseudorapidities.

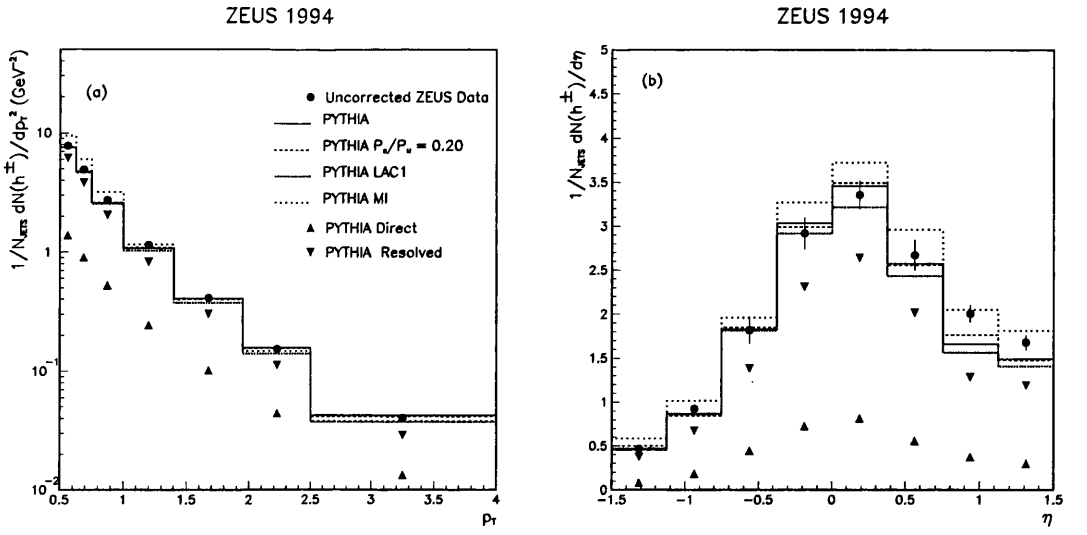

Figure 7.1: Uncorrected charged particle inclusive multiplicities as a function of p_T, (a), and η, (b) in hard photoproduction events with $0.15 \leq y_{JB} \leq 0.7$, containing a calorimeter jet with $E_T^{UCAL} \geq 7$ GeV and $|\eta^{UCAL}| \leq 0.5$. The data (filled circles) is compared to PYTHIA samples of direct (triangles), resolved (inverted triangles), mixed resolved plus direct (solid line), mixed $P_s/P_u = 0.20$ (dash-dotted line), mixed with LAC1 photon structure function(dotted line) and PYTHIA with multiple interactions (scarce dotted).

7.3 Correction Procedure

The default PYTHIA Monte Carlo sample was used to determine correction factors with which to calculate the inclusive multiplicities. A bin-by-bin correction procedure similar to that outlined in section 6.6 was applied in the multiplicity determination.

Figure 7.2 shows the reconstruction efficiency for charged particles on the primary vertex as a function of p_T and η. The efficiency is constant at 95 % as a function of p_T. The track reconstruction efficiency is 97 % for tracks at $\eta = 0$, and decreases to 92 % for tracks at large $|\eta|$. Lower track reconstruction efficiency for particles at large $|\eta|$ is expected since these particles have shorter tracks in the CTD and therefore less hits than more centrally produced particles.

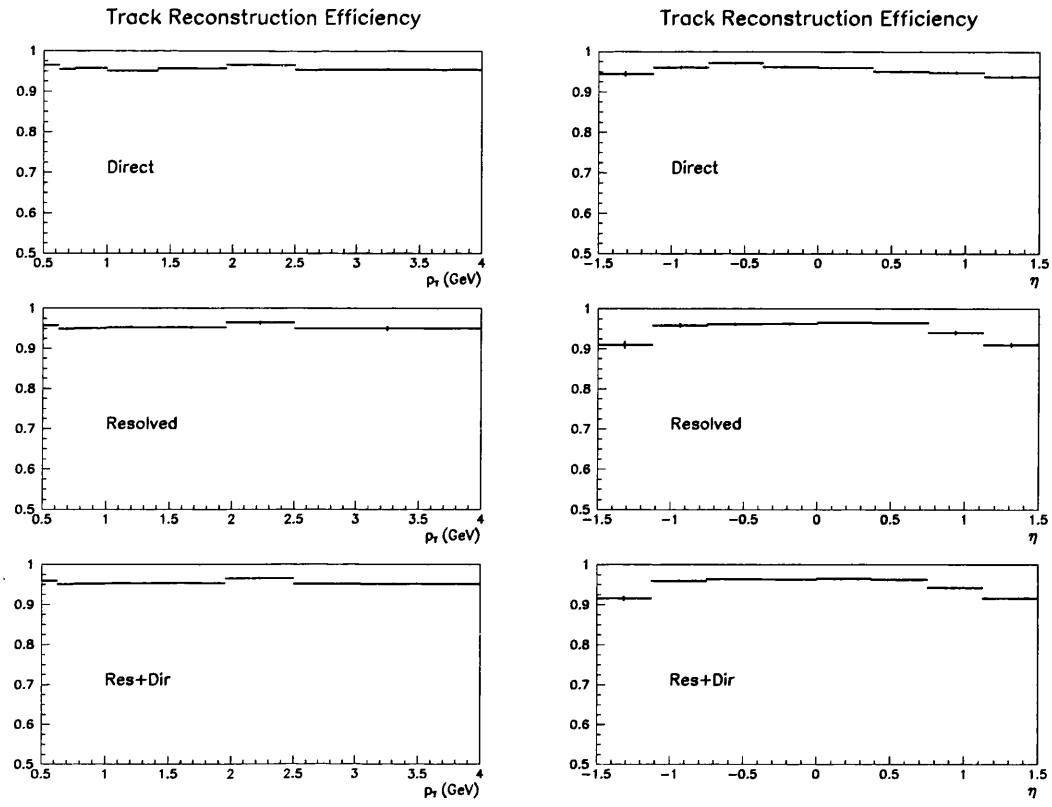

Figure 7.2: Charged track reconstruction efficiency as a function of p_T (left column) and η (right column) for direct (top row), resolved (middle row) and mixed resolved plus direct (bottom row) PYTHIA Monte Carlo samples.

7.4 Charged Particle Inclusive Multiplicities

The charged particle multiplicities as a function of p_T and η and their systematic errors were calculated analogously to the K^0 multiplicities. The difference between positive and negative charged particle distributions were considered as an additional systematic error.

The systematic changes in the charged particle multiplicities after changing a selection cut or reconstruction algorithm are plotted in figures 7.5 and 7.6. The dominant systematic errors were the choice of track reconstruction algorithm and the calorimeter energy scale. Using the CTD tracking alone gave an inclusive multiplicity higher than using the combined VXD, CTD plus RTD tracking. The effect was approximately 5% at low p_T, decreased to 2% at high p_T, and was approximately flat in η, at 4%. The effect of the $\pm 5\%$ uncertainty in the

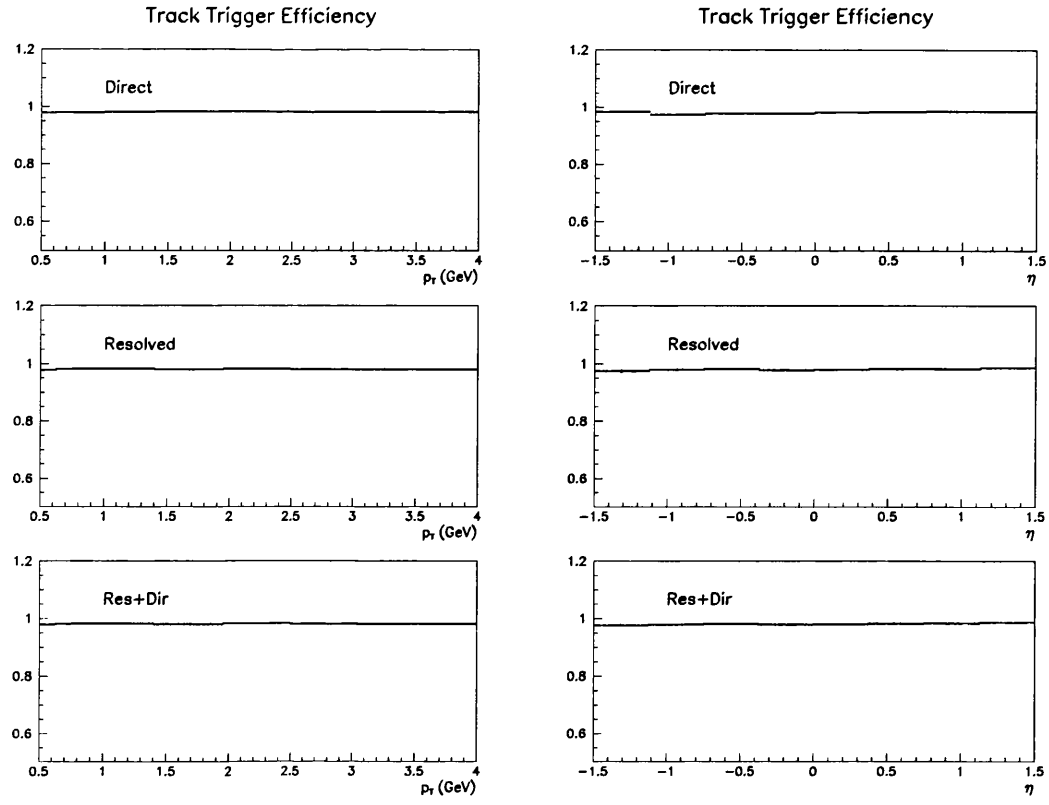

Figure 7.3: Trigger efficiency as a function of p_T (left column) and η (right column) for direct (top row), resolved (middle row) and mixed resolved plus direct (bottom row) PYTHIA Monte Carlo samples.

calorimeter energy scale was negligible at $p_T = 0.5$ GeV, but increased to $\pm 7\%$ at $p_T = 3.25$ GeV. The calorimeter energy scale uncertainty gave a systematic error of at most $\pm 3\%$ in the charged particle η spectrum. The systematic errors arising from event selection and the choice of photon and proton structure functions were found to be at most 1 %.

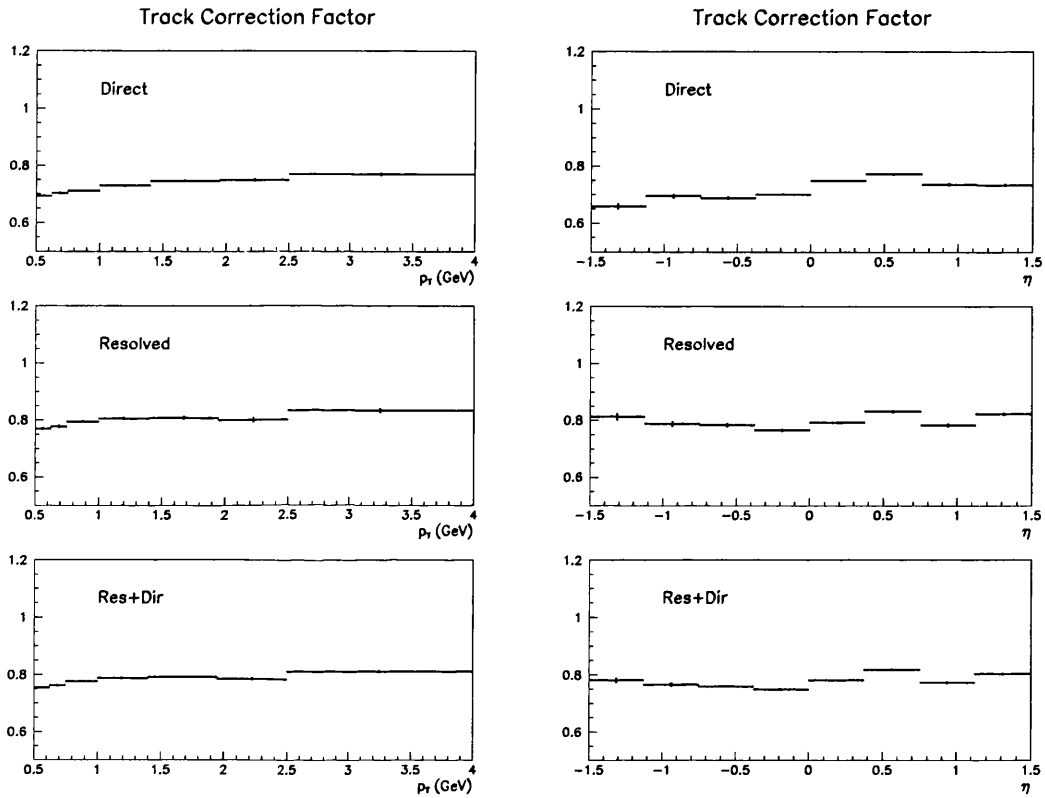

Figure 7.4: Correction factor as a function of p_T (left column) and η (right column) for direct (top row), resolved (middle row) and mixed resolved plus direct (bottom row) PYTHIA Monte Carlo samples.

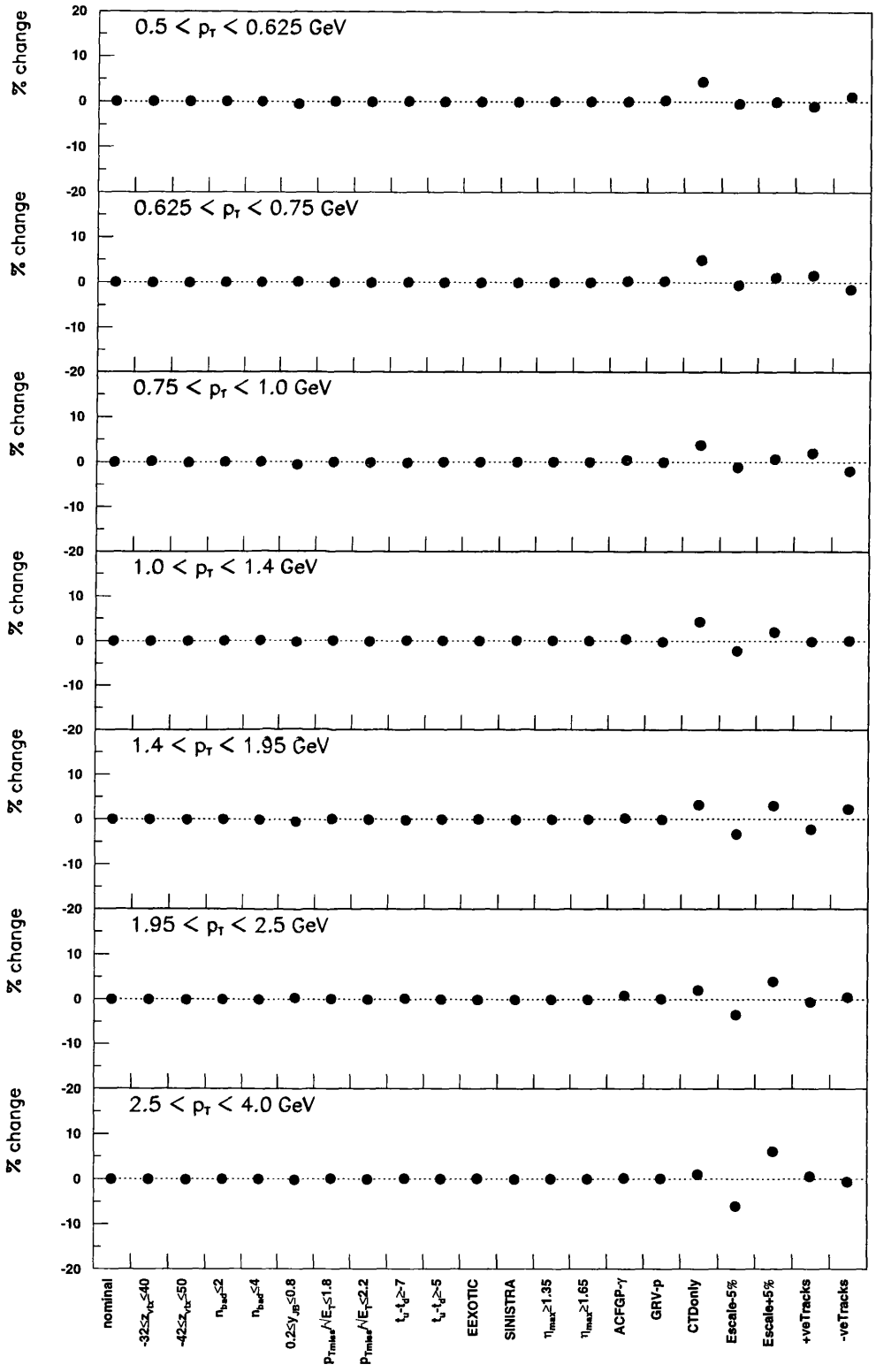

Figure 7.5: Systematic errors in $\frac{1}{N_{JETS}} \frac{dN(h^{\pm})}{dp_T^2}$.

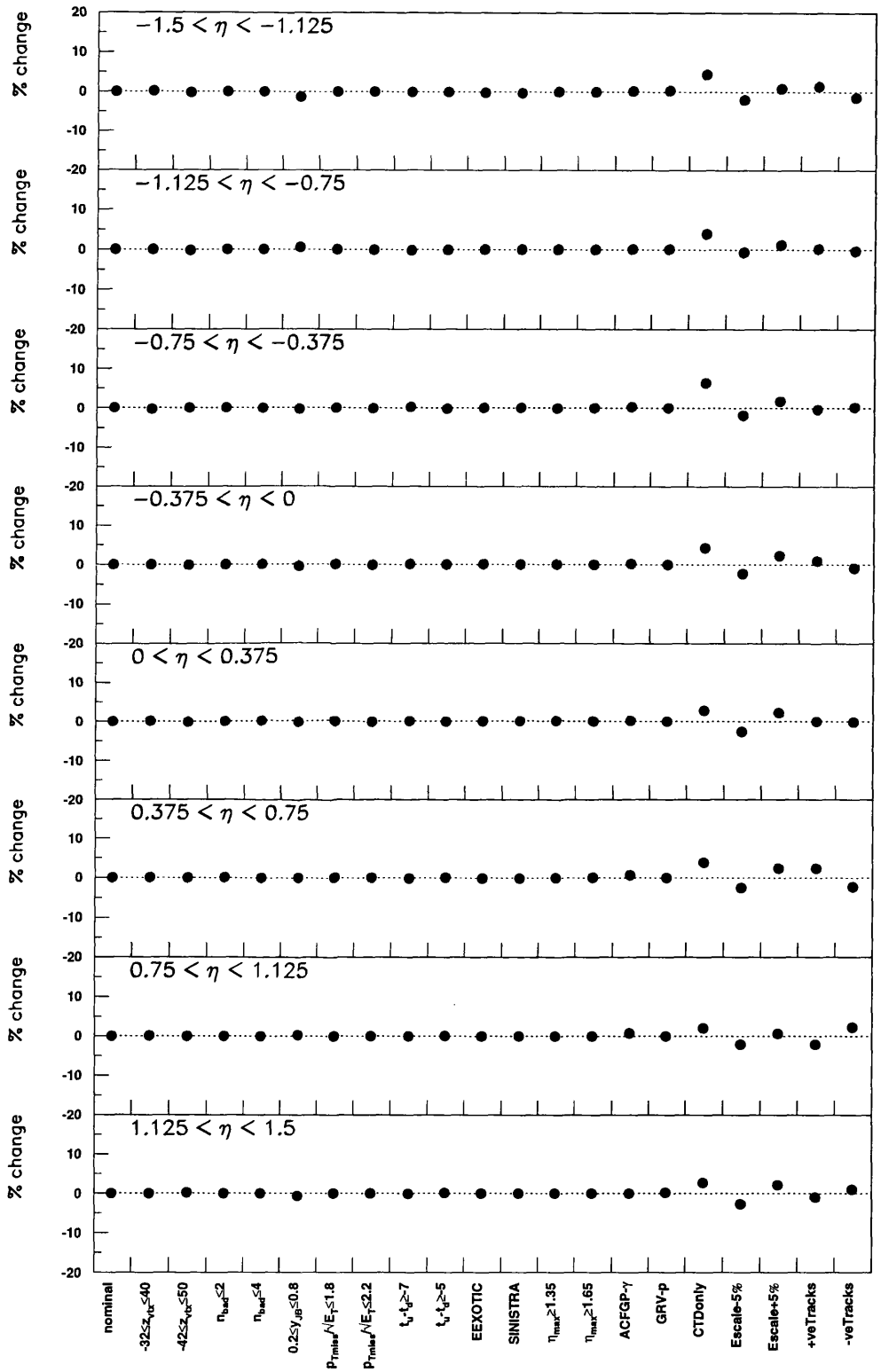

Figure 7.6: Systematic errors in $\frac{1}{N_{JETS}}\frac{dN(h^{\pm})}{d\eta}$.

Figure 7.7 shows the corrected inclusive multiplicities, $\frac{1}{N_{JETS}}\frac{dN(h^{\pm})}{dp_T^2}$, $\frac{1}{N_{JETS}}\frac{dN(h^{\pm})}{ap_T^2}$, $\frac{1}{N_{JETS}}\frac{dN(h^{\pm})}{d\eta}$ for charged particles in hard photoproduction events defined in section 5.2. The bold error bars denote the statistical error on each point arising from data and Monte Carlo. The thin error bars denote the statistical and systematic errors combined in quadrature. Also shown are the predictions of the PYTHIA resolved, direct and resolved plus direct samples generated with the default conditions and structure functions defined in section 2.4. In addition, the predictions of PYTHIA with $P_s/P_u = 0.20$, with the LAC1 photon structure function, and with multiple interactions are shown.

Since similar correction factors have been applied to the uncorrected data and Monte Carlo, similar conclusions are reached when comparing the corrected plots. In general, the charged particle p_T and η spectra are equally well described by the default, $P_s/P_u = 0.20$ and LAC1 reweighted resolved plus direct PYTHIA samples. However, at $\eta \geq 0.75$ the PYTHIA samples underestimate the data by approximately 20 %. This effect is probably related to the inclusive jet cross section excess observed by ZEUS [21]. PYTHIA with multiple interactions provides a good description of the charged particle multiplicity at $\eta \geq 0.75$, however it predicts a larger charged particle multiplicity at low p_T than is observed in the data, and generally overestimates the charged particle multiplicity at $\eta \leq 0.75$.

7.5 Charged Particle Production within Jets

7.5.1 $h^{\pm}$ - Jet Profiles

The uncorrected distributions in ϕ and η of charged particles relative to jets with $E_T^{UCAL} \geq 7$ GeV and $|\eta^{UCAL}| \leq 0.5$ are shown in figures 7.8(a) and (b). Similar features to the K^0 - jet profiles are observed; PYTHIA has an excess over the data in the jet core, and shows a small deficit with respect to the data in the region outside the jet. The jet profile as a function of the distance R between a charged particle and jet axis is shown in figure 7.8(c). The PYTHIA

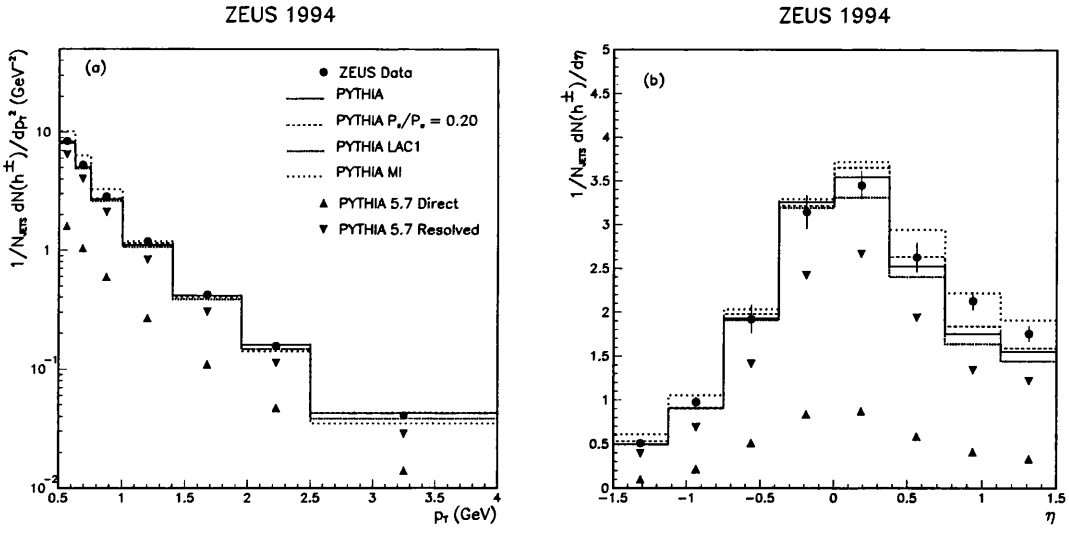

Figure 7.7: Corrected charged particle inclusive multiplicities in p_T, (a), and η, (b), in hard photoproduction events with $0.2 \leq y \leq 0.85$, containing a hadron jet with $E_T \geq 8$ GeV and $|\eta| \geq 0.5$. The data (filled circles) is compared to PYTHIA samples of direct (triangles), resolved (inverted triangles), mixed resolved plus direct (solid line), mixed $P_s/P_u = 0.20$ (dash-dotted line), LAC1 resolved plus direct (dotted line), and PYTHIA with multiple interactions (scarce dotted). The bold error bars denote the statistical error on each point arising from data and Monte Carlo. The thin error bars denote the statistical and systematic errors combined in quadrature.

Monte Carlo with default settings predicts an excess over the data in the jet core, $R < 0.4$. Compared to PYTHIA, the data shows a slight excess outside the jet core. Approximately 50 % of this excess is associated with the high pseudorapidity charged particle excess, the remainder being due to the difference in the jet shapes.

The systematic effects of the calorimeter energy scale uncertainty and the track reconstruction algorithm on the shape of the jet profile were considered as they were found to be the dominant systematic errors in the $\frac{1}{N_{JETS}}\frac{dN(h^{\pm})}{dp_T^2}$ and $\frac{1}{N_{JETS}}\frac{dN(h^{\pm})}{d\eta}$ measurements. Changing the track reconstruction algorithm increased the charged particle multiplicity by approximately 5 % over the whole jet profile. The ± 5 % calorimeter energy scale uncertainty gave rise to a ± 6 % uncertainty in the charged particle multiplicity in the jet core which became negligible in the inter-jet region. The systematic errors arising from these effects

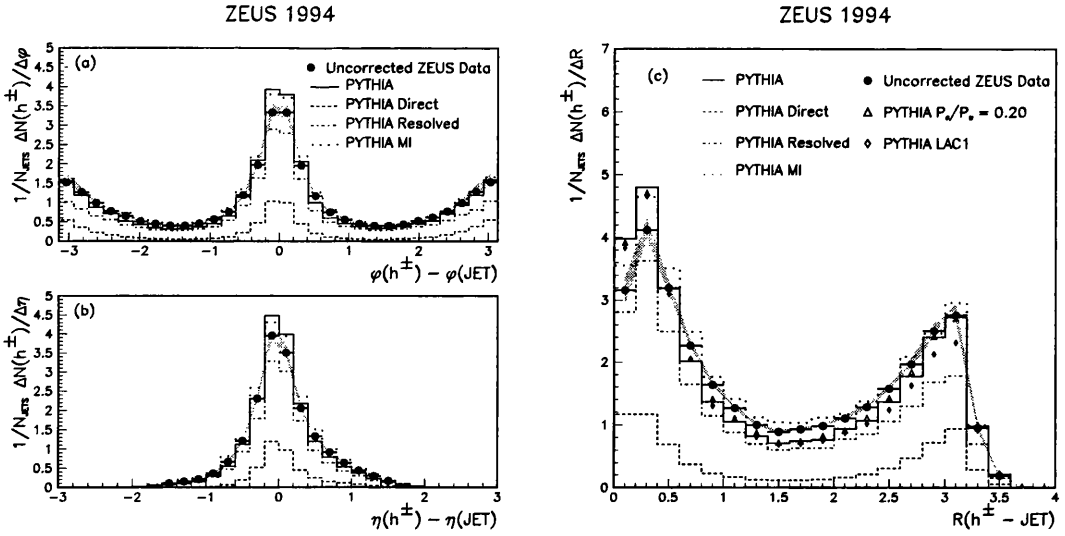

Figure 7.8: Uncorrected distribution of charged particles with respect to calorimeter jets in hard photoproduction events with $0.15 \leq y_{JB} \leq 0.7$, $E_T^{UCAL} \geq 7$ GeV and $|\eta^{UCAL}| \geq 0.5$ in ϕ (a) and η (b) and R (c). The data (filled circles) is compared to PYTHIA distributions of direct (dashed-line), resolved (dash-dotted line), resolved plus direct (solid line) and PYTHIA with multiple interactions, mixed according to the Monte Carlo cross section in all plots. The direct and resolved Monte Carlo distributions have been normalised to show the fraction of the charged particle multiplicity arising from the direct and resolved processes respectively. In (c) the data is also compared with the mixed $P_s/P_u = 0.20$ (triangles), and LAC1 resolved plus direct (diamonds) PYTHIA samples. The grey band represents the systematic error arising from the calorimeter energy scale uncertainty and tracking algorithm.

have been added together in quadrature and are depicted by the grey band in figure 7.8. Neither of these systematic effects could account for the difference between jet profiles in the data and PYTHIA Monte Carlo models tested. The discrepancy in the jet profiles between data and PYTHIA remained when the photon structure function was changed. As in the K^0 analysis, the jet profiles in the direct enriched sample of dijet events shown in figure 7.9 were in better agreement with the $P_s/P_u = 0.20$ PYTHIA sample at $R < 1$, than the default PYTHIA sample.

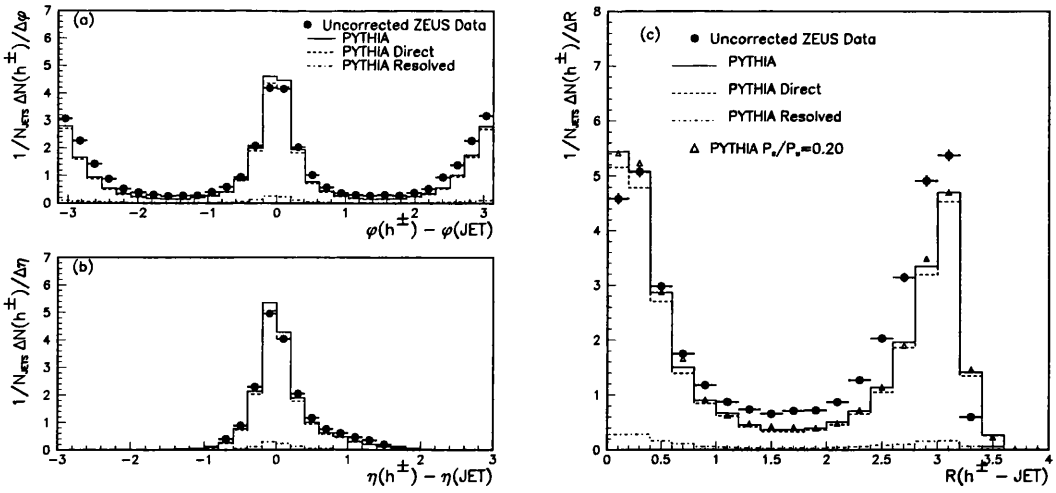

Figure 7.9: Uncorrected distributions of charged particles with respect to calorimeter jets of $E_T^{UCAL} \geq 7$ GeV and $|\eta^{UCAL}| \leq 0.5$ as functions of ϕ (a), η (b) and R (c) in a sample of direct enriched events selected as described in the text. The data (filled circles) is compared to PYTHIA distributions of direct (dashed-line), resolved (dash-dotted line), resolved plus direct (solid line) and $P_s/P_u = 0.20$, mixed according to the fractions of events with $x_\gamma^{OBS} \geq 0.75$, in all plots. The direct and resolved Monte Carlo distributions have been normalised to show the fraction of the K^0 multiplicity arising from the direct and resolved processes respectively.

7.5.2 $h^{\pm}$ Multiplicity per Jet

As in the K^0 analysis, charged particles were assigned to jets if they satisfied $R(h^{\pm} - JET) < 1$. The charged particle multiplicity per jet was calculated as

$$< n_{h^{\pm}/JET} >= \frac{n_{h^{\pm}}}{n_{JETS}} \tag{7.1}$$

where $n_{h^{\pm}}$ is the number of reconstructed charged particles which were assigned to a calorimeter jet and n_{JETS} was the number of calorimeter jets in each $\eta^{JET} = \eta^{UCAL}$ bin. The uncorrected charged particle multiplicity per jet for data and PYTHIA is shown in figure 7.10. The shapes of the data and Monte Carlo predictions are in good agreement, confirming again that the Monte Carlo can be used to correct the data using a bin-by-bin method.

The total correction factors for the separate direct, resolved and mixed resolved plus direct PYTHIA Monte Carlo samples are shown in figure 7.11. The correction factors are flat as a function of η^{JET} and are close to unity.

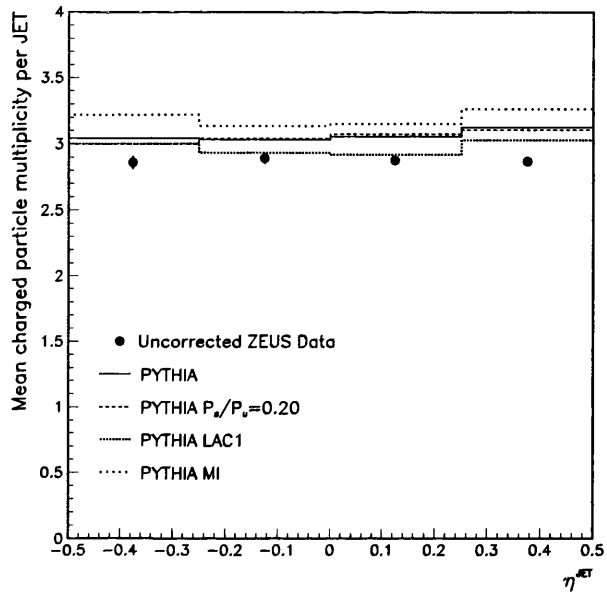

Figure 7.10: Uncorrected $h^{\pm}$ multiplicity per jet as a function of η^{JET}. The data (filled circles) is compared to distributions of the mixed resolved plus direct default PYTHIA sample (solid line), the $P_s/P_u = 0.20$ mixed PYTHIA sample (dashed line), the the LAC1 reweighted PYTHIA sample (dotted line) and PYTHIA with multiple interactions (scarce dotted).

As for the charged particle p_T and η spectra the largest systematic error associated with event selection is due to the y_{JB} region from which the data is selected. However, this effect dominates only in the highest two η^{JET} bins, contributing approximately 2% to the systematic error in these bins. The dominant systematic error is due to the tracking algorithm. Using only the CTD tracking information causes a systematic error of 2-4% which decreases with η^{JET}. The effect of the UCAL energy scale uncertainty on the number of charged particles and jets was expected largely to cancel in the charged particle multiplicity per jet, since it is a ratio. This is indeed the case; the systematic error arising from the UCAL energy scale uncertainty is less than 2% in all η^{JET} bins.

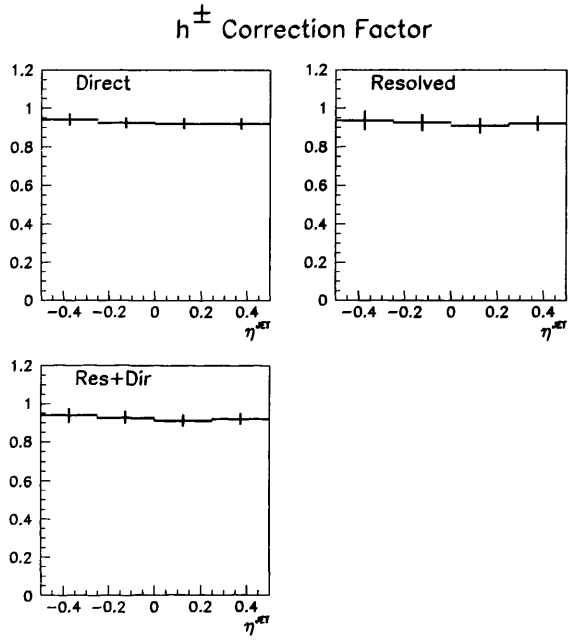

Figure 7.11: $h^{\pm}$ multiplicity correction factor as a function of η^{JET} for direct (top left), resolved (top right) and mixed resolved plus direct (bottom left) PYTHIA Monte Carlo samples.

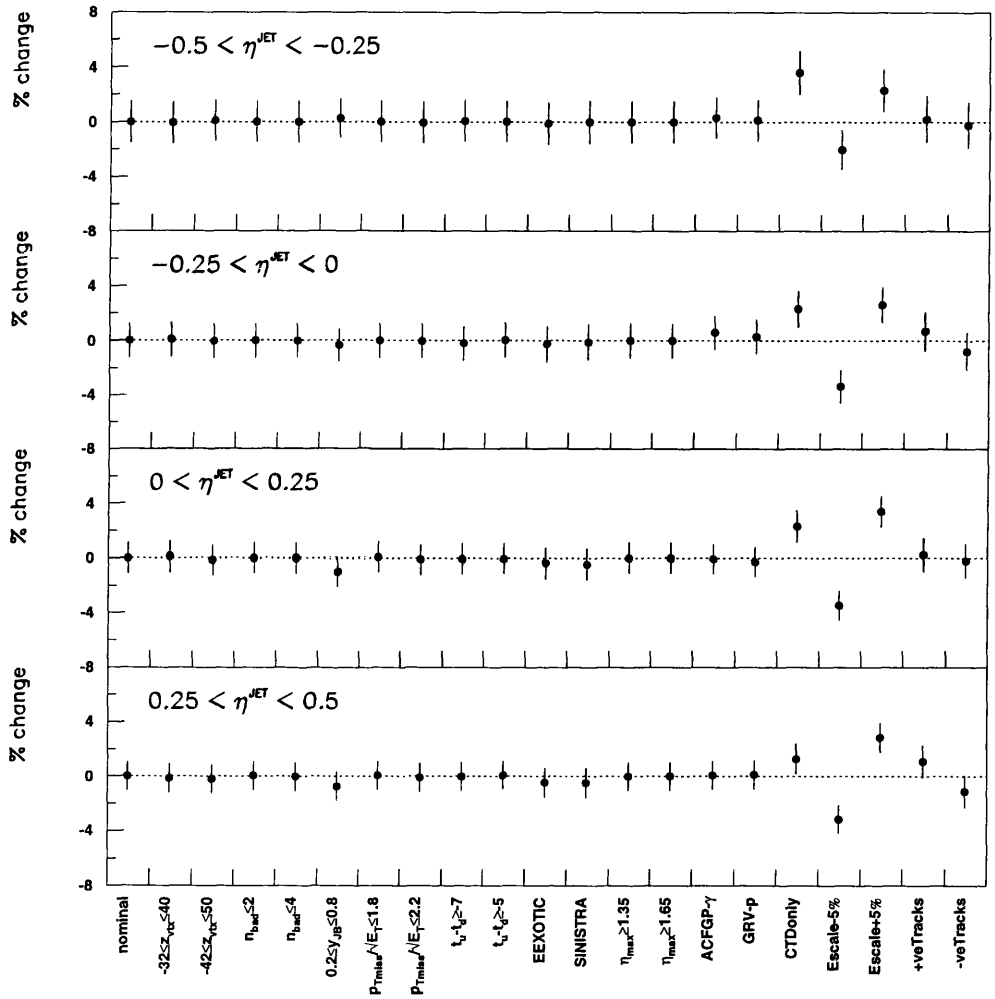

Figure 7.12: Systematic errors in $< n_{h^{\pm}/JET} >$.

The corrected charged particle multiplicity per jet in the data is compared to the default, $P_s/P_u = 0.20$, LAC1 photon structure function and multiple interaction PYTHIA predictions in figure 7.13. The jet pseudorapidity was shown to be accurately reconstructed in section 5.2 so $\eta^{HAD} = \eta^{JET} = \eta^{UCAL}$. The bold error bars denote the statistical error on each point arising from data and Monte Carlo. The thin error bars denote the statistical and systematic errors combined in quadrature. The data is essentially flat, while the Monte Carlo predictions exhibit a slow rise as η^{JET} increases. As shown in [21] the η^{JET} cross section is dominated by the resolved process at forward η^{JET}. The rise in $< n_{h^\pm/JET} >$ is possibly due to the increased proportion of gluon jets produced in the resolved interactions. Integrating over the region $|\eta^{HAD}| \leq 0.5$, the mean charged particle multiplicity per jet was found to be, $< n_{h^\pm/JET} > = 3.11 \pm 0.06^{+0.11}_{-0.10}$ where the first error is statistical and the second error is systematic. The default PYTHIA prediction was $< n_{h^\pm/JET} > = 3.32 \pm 0.04$. Changing the photon structure function from GRV to LAC1 gave a slightly lower value of $< n_{h^\pm/JET} > = 3.26 \pm 0.03$, while decreasing the strangeness suppression factor to $P_s/P_u = 0.2$ led to a value of $< n_{h^\pm/JET} > = 3.39 \pm 0.04$. PYTHIA with multiple interactions predicted $< n_{h^\pm/JET} > = 3.43 \pm 0.04$.

7.5.3 Charged Particle Fragmentation Function

The fragmentation function into charged particles has been determined using a similar method to the K^0 fragmentation function. Charged particles were assigned to jets using the criterion of section 7.5.2. The longitudinal jet momentum fraction carried by charged particles and the charged particle fragmentation function were calculated according to the definition,

$$z = \frac{p_{h^\pm} \cdot p_{JET}}{E^2_{JET}} \tag{7.2}$$

and,

$$D^{h^\pm}(z) = \frac{n_{h^\pm}(z)}{N_{JETS}} \frac{1}{\Delta z} \tag{7.3}$$

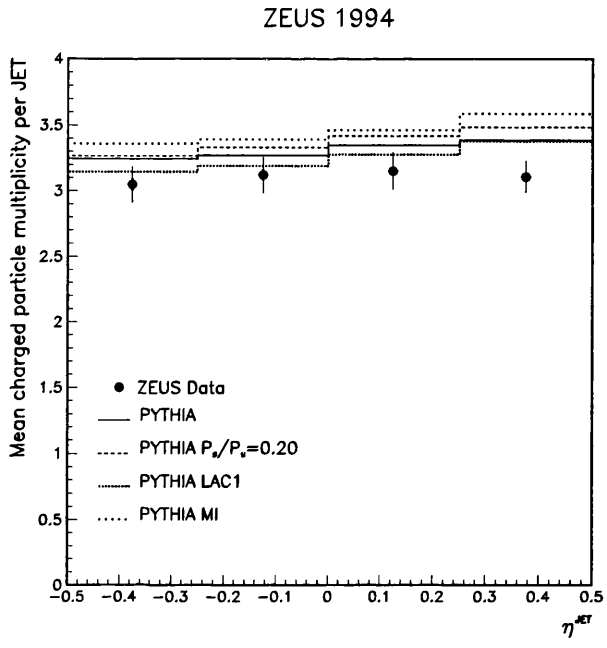

Figure 7.13: $h^{\pm}$ multiplicity per jet as a function of η^{JET} in hard photoproduction events with $0.2 < y < 0.85$, containing jets with $E_T^{HAD} > 8$ GeV and $|\eta^{HAD}| < 0.5$. The data (filled circles) is compared to distributions of the mixed resolved plus direct default PYTHIA sample (solid line), the $P_s/P_u = 0.20$ mixed PYTHIA sample (dashed line) and the LAC1 resolved plus direct PYTHIA sample (dotted line). The bold error bars denote the statistical error on each point arising from data and Monte Carlo. The thin error bars denote the statistical and systematic errors combined in quadrature.

where N_{JETS} is the total number of jets with $E_T^{JET} > 7$ GeV and $|\eta^{JET}| < 0.5$, $n_{h^{\pm}}(z)$ was the number of charged particles fitted to the primary vertex with $p_T > 0.5$ GeV, $|\eta| < 1.5$ and in the jet momentum fraction in the range z to $z + \Delta z$.

The uncorrected charged particle fragmentation function is shown in figure 7.14. The data and Monte Carlo points are plotted at the mean z value within each bin. There is good general agreement between the uncorrected data and PYTHIA Monte Carlo predictions. The shape of the fragmentation functions determined from the Monte Carlo and data are affected at $z < 0.05$ by the requirement that $p_T(h^{\pm}) > 0.5$ GeV.

The accuracy and resolution of the reconstructed charged particle jet mo-

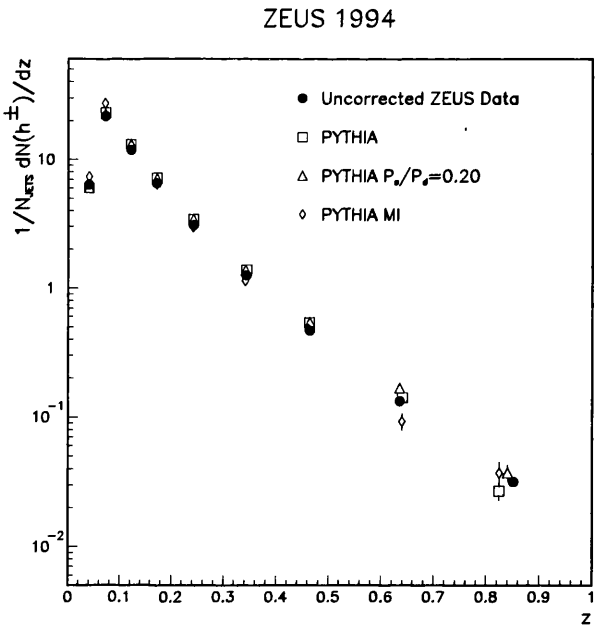

Figure 7.14: Uncorrected charged particle fragmentation function. The data (filled circles) is compared to distributions of the mixed resolved plus direct default PYTHIA sample (open squares), the $P_s/P_u = 0.20$ mixed PYTHIA sample (open triangles) and PYTHIA with multiple interactions (open diamonds).

mentum fraction is shown in figure 7.15 by calculating $z_{reco} - z_{true}$. There is a small average shift of +0.02 in the reconstructed jet momentum fraction relative to the true jet momentum fraction. This is compatible with the shift in the jet momentum fraction carried by K^0_s. A shift in the reconstructed jet momentum fraction is expected because the jet energy measured by the UCAL is lower than the true value because of effects described in section 5.2, while the CTD provides a momentum measurement free of any such bias.

The shift in the reconstructed jet momentum fraction was proportional to the true jet momentum fraction, as shown in figure 7.15. Applying a 10 % reduction to the reconstructed jet momentum fraction gave the momentum fraction resolution shown in figure 7.16. As in the K^0 analysis the difference in correcting or not correcting the fragmentation functions for the CTD-UCAL energy scale difference has been included in the systematic errors.

The resolution in jet momentum fraction, σ_z, as a function of jet momentum

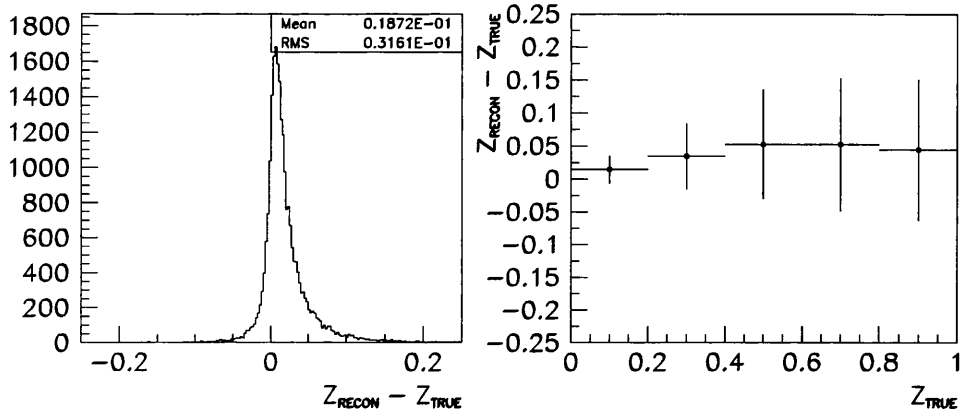

Figure 7.15: The jet momentum fraction resolution (left) and jet momentum fraction resolution as a function of true jet momentum fraction (right) without taking into account the energy scale difference between the tracking and UCAL.

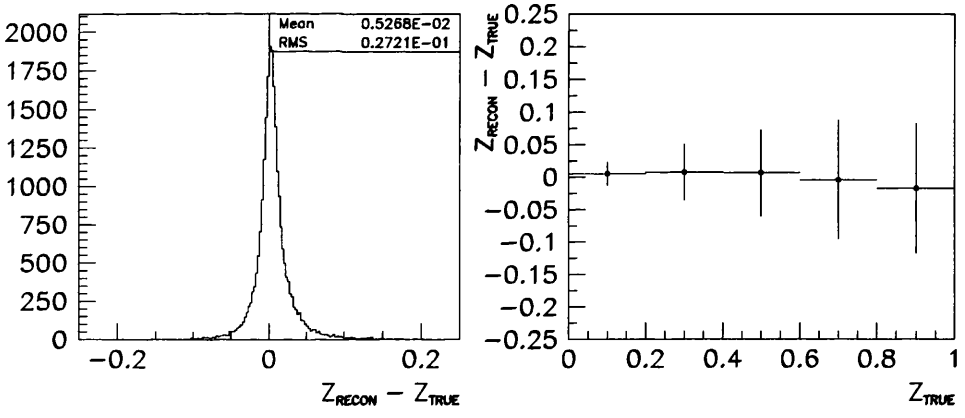

Figure 7.16: The jet momentum fraction resolution (left) and jet momentum fraction resolution as a function of true jet momentum fraction (right) taking into account the energy scale difference between the tracking and UCAL.

fraction is given in table 7.1. The charged particle fragmentation function was calculated in bins of width approximately $2\sigma_z$.

A bin-by-bin correction procedure for determining the corrected $h^{\pm}$ fragmentation function in events containing a hadron jet with $E_T^{HAD} > 8$ GeV, $|\eta^{HAD}|$

z	σ_z
$0. \leq z < 0.2$	0.02
$0.2 \leq z < 0.4$	0.05
$0.4 \leq z < 0.6$	0.08
$0.6 \leq z < 0.8$	0.1
$0.8 \leq z < 1.$	0.12

Table 7.1: Resolution in jet momentum fraction.

as discussed in section 6.6 was applied. The total correction factors for the separate direct and resolved and mixed resolved plus direct PYTHIA Monte Carlo samples are shown in figure 7.17. The z dependence of the correction factors arises from bin-to-bin migrations caused by the CTD-UCAL energy scale difference, since modifying the reconstructed z for the effect of the CTD-UCAL energy scale difference gave correction factors which were flat as a function of z. Despite this effect, the good agreement between the uncorrected data and Monte Carlo distributions gives confidence in the validity of the bin-by-bin correction procedure. Furthermore, the systematic error determination used different correction methods which ignored and accounted for the CTD-UCAL energy scale difference. These two methods gave compatible results and thus confidence in the bin-by-bin correction procedure.

The systematic errors due to event selection cuts were all found to be small; no more than 2% in any bin. Correcting the data with different photon and proton structure functions each contribute approximately 2% to the systematic error. The track reconstruction algorithm was found to be the dominant systematic error at low z contributing at most 8%, but typically 5%. The uncertainty in the calorimeter energy scale produces a 2% systematic error at low jet momentum fraction which increases to 30% in the final z bin. Correcting the calculated jet momentum fraction for the difference in energy scale between the CTD and UCAL produced an uncertainty of typically 5% which increased to 30% in the

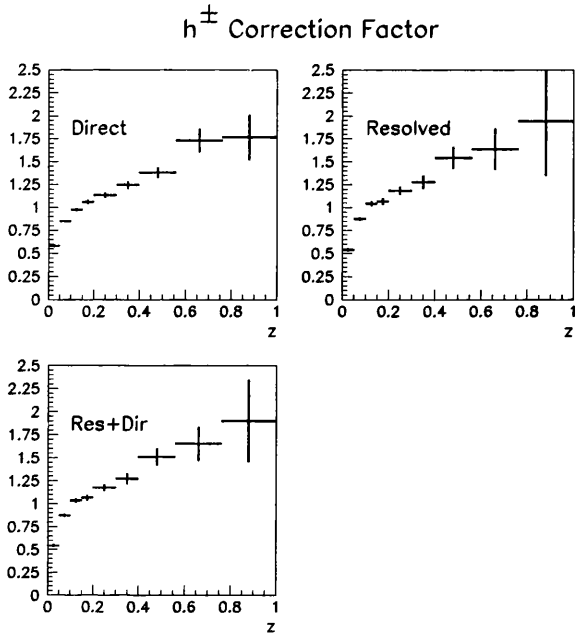

Figure 7.17: $h^{\pm}$ fragmentation function correction factors as a function of z for direct (top left), resolved (top right) and mixed resolved plus direct (bottom left) PYTHIA Monte Carlo samples.

final z bin.

The corrected charged particle fragmentation function is compared to the predictions of the default PYTHIA, $P_s/P_u = 0.20$, PYTHIA with multiple interactions and the results of [1] in figure 7.19. The data and Monte Carlo points are plotted at the mean z value within each bin, without taking into account any shift in z arising from the CTD-UCAL energy scale difference. The lower curve corresponds to NLO u quark fragmentation for $z < 0.25$ and c quark fragmentation for $z > 0.25$. The upper curve corresponds to LO s quark fragmentation for $z < 0.35$ and $u = d$ quark fragmentation for $z > 0.35$. Good agreement in the charged particle fragmentation function is observed between the data and both PYTHIA Monte Carlo samples. The data and results of [1] are in good agreement for $z < 0.3$, while the data lies slightly below the results of [1] for higher jet momentum fraction. Part of the discrepancy may be attributable to the difference in definition of final state charged particles adopted in this analysis and in [1].

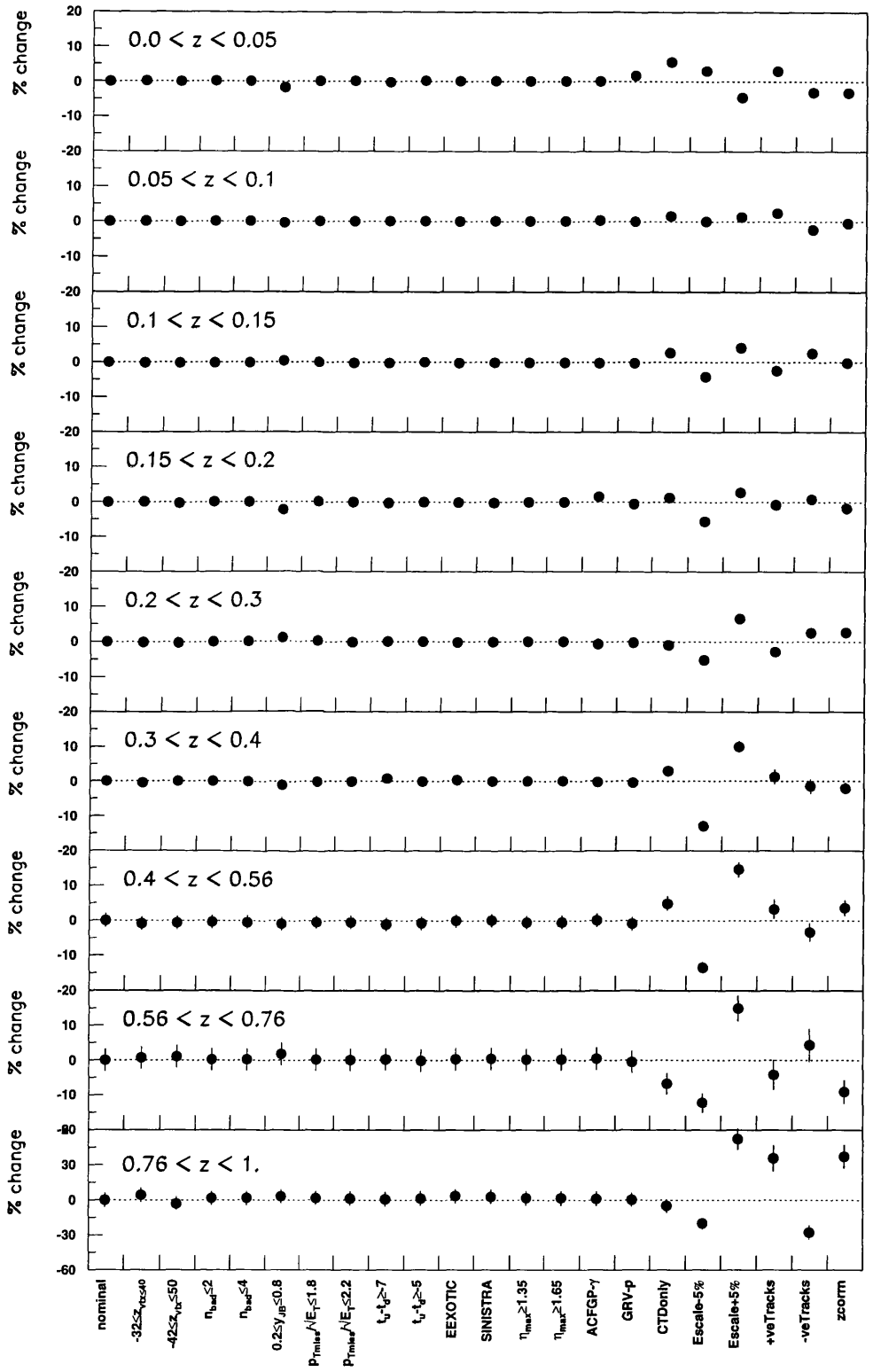

Figure 7.18: Systematic errors in $D^{h^{\pm}}(z)$.

As in the K^0 analysis the effect of the different definitions of jet momentum fraction, z, between this analysis and the calculation of Binnewies et al. has been investigated. Figure 7.20 shows fragmentation functions $D^{h^\pm}(z)$ and $D^{h^\pm}(z')$ using similar definitions of z and z' as in the K^0 analysis. Also shown in figure 7.20 is the range covered by the calculations of Binnewies et al. The measured $D^{h^\pm}(z')$ is clearly in better agreement with Binnewies et al.

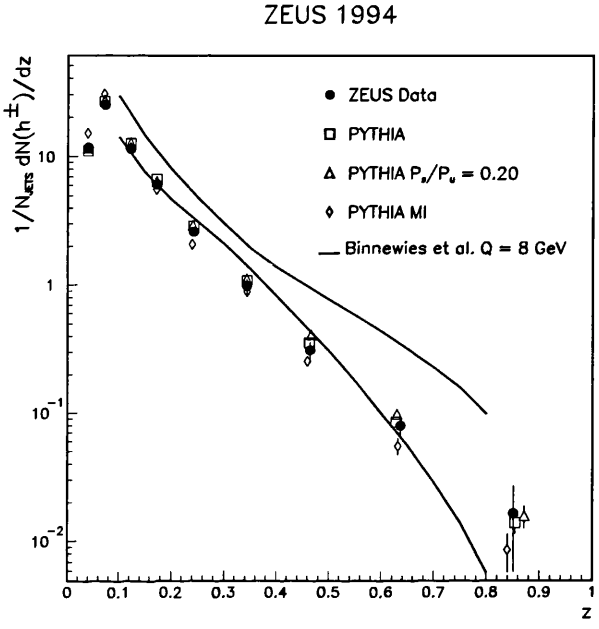

Figure 7.19: The charged particle fragmentation function in hard photoproduction events with $0.2 \leq y \leq 0.85$, containing jets with $E_T^{HAD} \geq 8$ GeV and $|\eta^{HAD}| \leq 0.5$. The data (filled circles) is compared to distributions of the mixed resolved plus direct default PYTHIA sample (open squares) and the $P_s/P_u = 0.20$ mixed PYTHIA sample (open triangles). The range covered by the prediction of [1] lies between the solid lines.

7.6 Final Charged Particle Results

As stated in section 7.4 the inclusive multiplicities $\frac{1}{N_{JETS}}\frac{dN(h^\pm)}{dp_T^2}$ and $\frac{1}{N_{JETS}}\frac{dN(h^\pm)}{d\eta}$ are equally well described by the default, $P_s/P_u = 0.20$ and LAC1 reweighted resolved plus direct PYTHIA samples. However, the $\frac{1}{N_{JETS}}\frac{dN(h^\pm)}{d\eta}$ measurement shows that these samples underestimates the charged particle cross section at

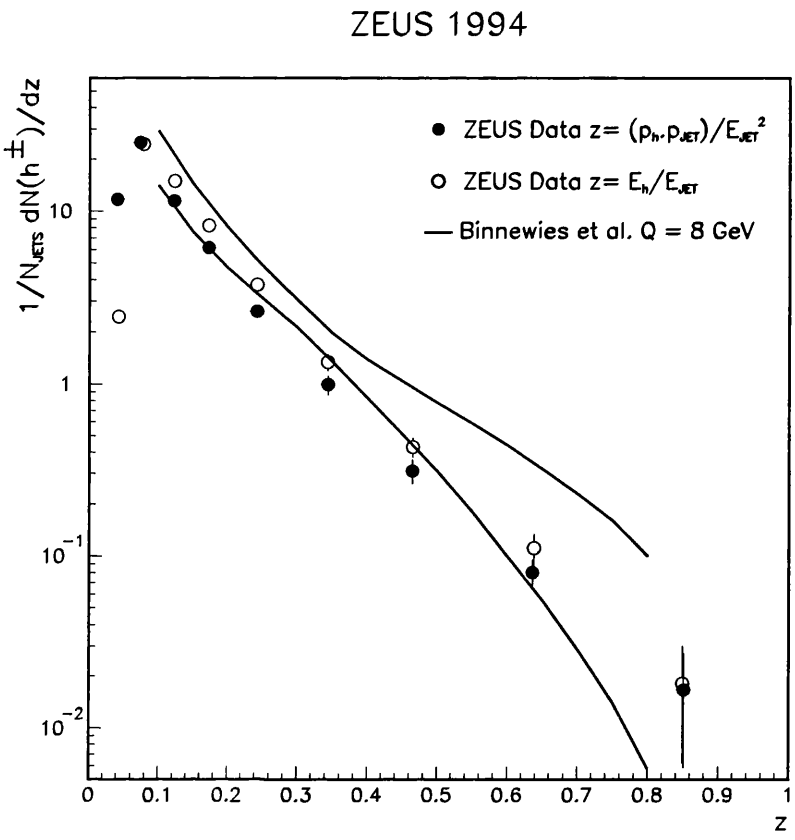

Figure 7.20: The charged particle fragmentation function in hard photoproduction events with $0.2 \leq y \leq 0.85$, containing jets with $E_T^{HAD} \geq 8$ GeV and $|\eta^{HAD}| \leq 0.5$. The result obtained using the definition $z' = \frac{E_{h^\pm}}{E_{JET}}$ (open circles) is compared with the range covered by the prediction of [35]. The result obtained using the definition $z = \frac{p_{h^\pm} \cdot p_{JET}}{E_{JET}^2}$ is depicted by the filled circles.

$\eta > 0.75$. Using the GS2 and ACFGP photon structure functions gave charged particle cross sections very similar to the default PYTHIA Monte Carlo. PYTHIA with multiple interactions provides a good description of the particle multiplicity at $\eta \geq 0.75$, but predicts a larger charged particle multiplicity at low p_T than is observed in the data, and generally overestimates the charged particle multiplicity at $\eta \leq 0.75$.

The observation of section 7.5.2, that the charged particle multiplicity per jet is lower in the data than in any of the Monte Carlo models considered is unchanged. Integrating over the region $|\eta^{HAD}| \leq 0.5$ gave a value of

$< n_{h^{\pm}/JET} > = 3.11 \pm 0.06^{+0.11}_{-0.10}$. As with the K^0 analysis, the excess multiplicity was located in the jet core.

There is good agreement between the charged particle fragmentation function measured in the data and predicted by the default and $P_s/P_u = 0.20$ PYTHIA Monte Carlo samples, while PYTHIA with multiple interactions predicts a softer fragmentation function than is observed in the data. The data and results of [1] are in good agreement.

Chapter 8

Summary and Conclusions

This thesis has presented the first analysis of charged particle and K^0 production in hard photoproduction jets at HERA. K^0 and charged particle multiplicities in the kinematic regions $-1.5 \leq \eta \leq 1.5$ and $p_T \geq 0.5$ GeV have been measured as a function of p_T and η respectively. The K^0 and charged particle mean multiplicities per jet and fragmentation functions have also been measured. The measurements have been corrected back to the kinematic range $E_T^{JET} \geq 8$ GeV, $|\eta^{JET}| \leq 0.5$, $Q^2 \leq 4$ GeV^2, $0.2 \leq y_{JB} \leq 0.85$, corresponding to a γp centre of momentum energy of $60 \leq W \leq 255$ GeV. These measurements complement results already obtained by ZEUS and H1 on K^0 and charged particle production in DIS [73, 74] and inclusive photoproduction [75, 76].

A method of calibrating the ZEUS CTD which incorporated correlations between the calibration constants was developed. Monte Carlo tests showed this procedure provided an accurate global calibration of the CTD. The single-hit resolution obtained by this method for 1994 data was typically 290 μm, comparable to that obtained by the standard calibration procedure.

An algorithm for reconstructing $K_s^0 \rightarrow \pi^+ \pi^-$ decays was developed. The reconstruction algorithm was shown to be accurate and a clear K_s^0 signal was observed. Detector effects and reconstruction efficiencies in the data were taken into account by applying a bin-by-bin correction procedure and systematic errors were evaluated. The main systematic errors arose from the choice of tracking

algorithm and uncertainty in the calorimeter energy scale.

The corrected data has been compared to PYTHIA Monte Carlo predictions with default hadronisation, with the strangeness suppression factor, $P_s/P_u = 0.2$, default hadronisation reweighted to the LAC1 photon structure function and with multiple interactions. The default PYTHIA Monte Carlo was found to describe the $\frac{1}{N_{JETS}}\frac{dN(K^0)}{dp_T^2}$ spectrum well, while the $P_s/P_u = 0.2$ PYTHIA Monte Carlo predicted a lower $\frac{1}{N_{JETS}}\frac{dN(K^0)}{dp_T^2}$ spectrum than the data. However, examining the $\frac{1}{N_{JETS}}\frac{dN(K^0)}{d\eta}$ spectrum showed that PYTHIA overestimated this at backward pseudorapidity, but underestimated it at forward pseudorapidities. The $P_s/P_u = 0.2$ PYTHIA Monte Carlo prediction for $\frac{1}{N_{JETS}}\frac{dN(K^0)}{d\eta}$ was in good agreement with the data at backward psuedorapidity but also did not describe the forward psuedorapidity region. The discrepancy in the forward direction is believed to arise from the same cause as the forward jet cross section observed in earlier ZEUS and H1 measurements, which have proved difficult to simulate with currently available Monte Carloes. Using the LAC1 photon structure function which describes fairly well the inclusive jet cross section at forward psudorapidity does not however improve the descriptions of the $\frac{1}{N_{JETS}}\frac{dN(K^0)}{dp_T^2}$, or $\frac{1}{N_{JETS}}\frac{dN(K^0)}{d\eta}$ spectra. PYTHIA with multiple interactions provided a better description of the forward psuedorapidity region but failed to describe the $\frac{1}{N_{JETS}}\frac{dN(K^0)}{dp_T^2}$ spectrum at low p_T. H1 recently measured $\frac{d\sigma(K^0)}{d\eta}$ in inclusive photoproduction [75, 76] and found good agreement with the PYTHIA Monte Carlo using $P_s/P_u = 0.20$ at $\eta < 0.5$, and observed an excess in the data over the $P_s/P_u = 0.20$ Monte Carlo at large η, even after inclusion of multiple interaction effects.

By examining the distributions in ϕ and η between K_s^0 mesons and jets, K_s^0 were shown to be produced in association with high E_T jets and the mean K^0 multiplicity per jet has been measured. The default PYTHIA Monte Carlo predicted a mean K^0 multiplicity per jet 20 % greater than measured in the data. This discrepancy was present in both direct and resolved photoproduction events, could not be attributed to tracking efficiency problems between the data and Monte Carlo and could not be accounted for by changing the photon structure

function. The uncorrected K^0_s - jet profiles showed that the jets in the data were broader than those predicted by the PYTHIA Monte Carloes considered. An excess over the data in the mean K^0 multiplicity per jet was observed in the jet core ($R < 0.4$) while a deficit was observed in the wings of the jet ($0.4 < R < 1$). The mean K^0 multiplicity per jet predicted by the $P_s/P_u = 0.2$ Monte Carlo was in good agreement with the data, however the effect of lowering P_s/P_u was to renormalise the K^0 - jet profile such that better agreement was obtained in the jet core at the expense of the wings of the jet, and the region outside the jet affected by the high pseudorapidity K^0 excess. Simply lowering the strangeness suppression factor does not therefore provide a complete solution to the difference in the mean K^0 multiplicity per jet between PYTHIA and the data.

Corresponding distributions for charged particles have been studied. The charged particle p_T, η spectra were in reasonable agreement with the default PYTHIA prediction. However, an excess was observed in the charged particle η spectrum as in case of the K^0 η spectrum. Except for the high η region, the data was also in reasonable agreement with the p_T and η spectra predicted by the $P_s/P_u = 0.2$ and LAC1 reweighted PYTHIA samples. As with the K^0 p_T and η spectra, PYTHIA with multiple interactions provided a better description of the forward psuedorapidity region but failed to describe the charged particle multiplicity at low p_T. As with the K^0_s - jet profiles, the distributions of charged particles relative to the jet axes were found to be narrower in the PYTHIA Monte Carlo models considered than in the data. The difference in jet shape led to a 10 % difference in the charged particle multiplicity.

The K^0 and charged particle fragmentation functions were in reasonable agreement with both the default and $P_s/P_u = 0.2$ PYTHIA predictions, and also with the spread of values corresponding to a QCD calculation of LO and NLO fragmentation functions of different flavours of final state partons [2, 1]. PYTHIA with multiple interactions predicted fragmentation functions which were softer than those observed in the data. Since the JETSET hadronisation model and QCD fragmentation functions are primarily based on measurements made at e^+

e^- experiments this thesis provides evidence for the universality of quark and gluon fragmentation.

The PYTHIA Monte Carlo with its default hadronisation parameters has been found to describe charged particle production more accurately than K^0 production. An investigation of the effects of different hadronisation parameters, or of multiple interactions on the predictions of PYTHIA should improve the description of the data.

Appendix A

Secondary Vertex Reconstruction

A.1 Tracking Parametrisation

The K_s^0 reconstruction algorithm used tracks reconstructed by the VCTRAK package. VCTRAK provided tracks parametrised in terms of the following variables.

1. ϕ_H, the azimuthal angle of the tangent to the track at its point of closest approach to the line $x = y = 0$.
2. Q/R, where Q was the charge and R the local radius.
3. ϵ, the distance of closest approach of the track to the line $x = y = 0$.
4. Z_H, the z-coordinate of the track at its closest approach to the line $x = y = 0$.
5. $\cot\theta_H$, where θ_H was the polar angle of the track.

The track parameters are depicted in figure A.1

A.2 Secondary Vertex Coordinate

The centre of curvature of each charged track was calculated according to

$$X_C = (\epsilon - R)\cos\phi_0 \tag{A.1}$$

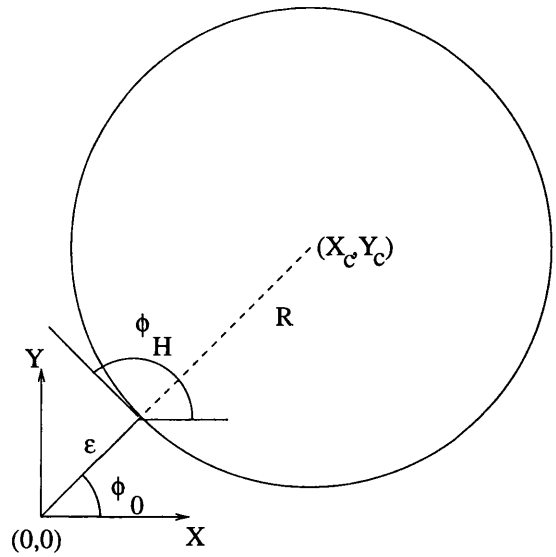

Figure A.1: VCTRAK track reconstruction parameters.

$$Y_C = (\epsilon - R)\sin\phi_0 \tag{A.2}$$

From these coordinates the length, D, and the direction of the line joining the centres of curvature of a charged track pair was calculated. Non-intersecting track pairs were rejected by testing if any of the following conditions were true,

$$D > |R_1| + |R_2| \tag{A.3}$$

$$|R_1| > D + |R_2| \tag{A.4}$$

$$|R_2| > D + |R_1| \tag{A.5}$$

The angle subtended by half of the chord joining the two candidate secondary vertices at each track's centre was calculated using

$$\sin\alpha_1 = \frac{f(R_1,R_2,D)}{(2DR_1)^2} \quad \sin\alpha_2 = \frac{f(R_1,R_2,D)}{(2DR_2)^2} \tag{A.6}$$

$$\begin{aligned} f(R_1,R_2,D) = {} & (|R_1| - |R_2| + D)(|R_1| + |R_2| - D) \\ & (|R_2| + D - |R_1|)(|R_1| + |R_2| + D) \end{aligned} \tag{A.7}$$

The quadrants of α_1 and α_2 were determined using the cosine rule. The candidate secondary vertex coordinates in the xy-plane were calculated for each track from

$$X_{V_i} = X_{C_i} + |R_i|\cos(\beta_i \pm \alpha_i) \tag{A.8}$$

$$Y_{V_i} = Y_{C_i} + |R_i|\sin(\beta_i \pm \alpha_i) \tag{A.9}$$

It was checked that the candidate secondary vertex coordinates evaluated using both tracks were in agreement. The azimuthal angles of the tangents to each track at the candidate vertices were given by

$$\phi_{1i} = \beta_1 \pm \alpha_i - \frac{3\pi}{2} \tag{A.10}$$

$$\phi_{2i} = \beta_2 \pm \alpha_i - \frac{\pi}{2} \tag{A.11}$$

where the first(second) index denotes the track(candidate vertex). Assuming uniform motion in the z-direction, tracks follow straight lines in the zs-plane where s denotes the path length along a track. s was calculated from

$$s_i = R_j(\phi_{ji} - \phi_{H_j}) \tag{A.12}$$

where ϕ_{H_j} denotes the azimuthal angle of the tangent to track j at its point of closest approach to the z axis. Then the z coordinate of track j at secondary vertex i is given by,

$$Z_{V_{ji}} = Z_{H_j} + \frac{s_i}{\tan\theta_j} \tag{A.13}$$

A.3 K_s^0 Momentum Reconstruction.

Since the momentum components of each track at the track starting point were known, and the tracks were assumed to undergo uniform circular motion in the xy-plane and uniform motion along the z-direction, the momentum components of each track at each secondary vertex were given by,

$$p_{x1i} = p_{T1}^{start}\cos\phi_{1i}, \quad p_{y1i} = p_{T1}^{start}\sin\phi_{1i}, \quad p_{z1i} = p_{z1}^{start} \tag{A.14}$$

The K_s^0 momentum was given by the sum of the track pairs momentum components.

Appendix B

Second Analysis

A second independent analysis was performed [77]. The main differences between the analysis presented in this thesis (Analysis 1) and the second analysis were:

1. Positron finder. Analysis 1 used the ELEC5 e^+ finder. Analysis 2 used SINISTRA, and corrected the e^+ energy for the effects of dead material in front of the calorimeter.

2. The effects of noisy UCAL cells were suppressed in Analysis 2 by application of the NOISE94 subroutine.

3. Analysis 2 used the V0FIND subroutine to reconstruct K_s^0 and Λ decays, and a different window range for background subtraction from the K_s^0 signal.

The results of the analysis presented in this thesis and the second analysis are compared in figures B.1 and B.2. Good agreement between the analyses is observed.

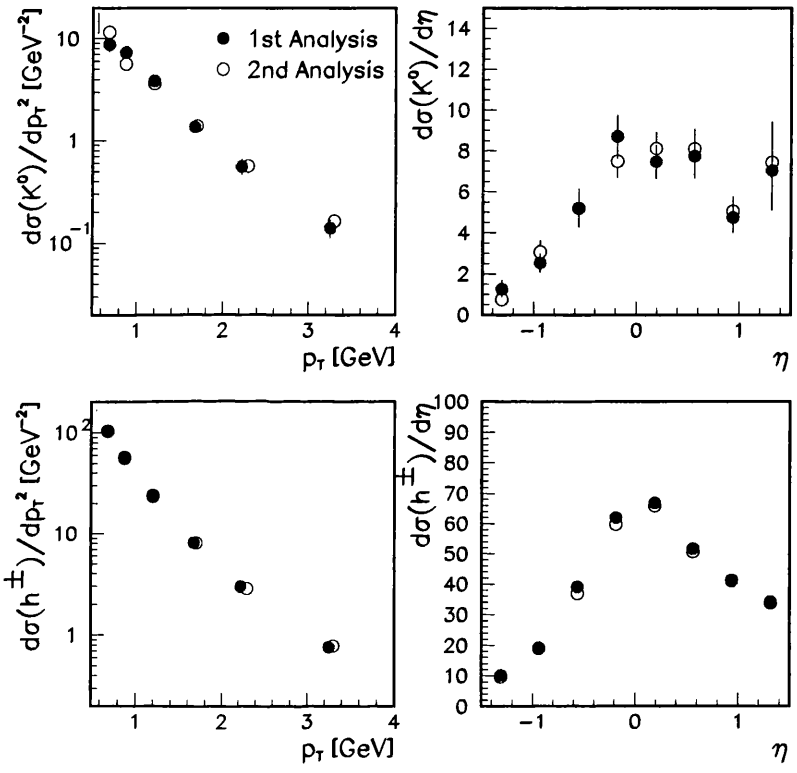

Figure B.1: Comparison of results from two independent analyses. The results presented in this thesis are shown as the '1st Analysis'. The results of [77] are shown as the '2nd Analysis'.

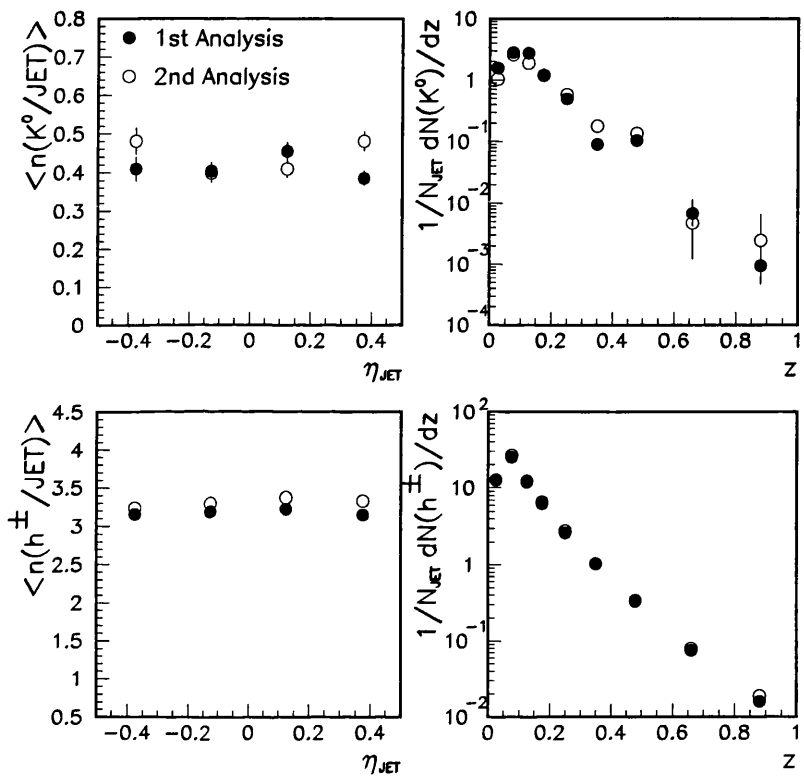

Figure B.2: Comparison of results from two independent analyses. The results presented in this thesis are shown as the '1st Analysis'. The results of [77] are shown as the '2nd Analysis'.

Bibliography

[1] B.A. Kniehl J. Binnewies and G. Kramer *Phys. Rev.*, (D 52):4947, 1995.

[2] B.A. Kniehl J. Binnewies and G. Kramer *Phys. Rev.*, (D 53):3573, 1996.

[3] Donald H. Perkins *Introduction to High energy Physics.* Addison Wesley, 1986.

[4] F. Jacquet and A. Blondel In *Proceedings of the Study of an ep facility for Europe*, page 391, 1979.

[5] A. Bodek et al. *Phys. Rev.*, (D 20):1471, 1979.

[6] J.I. Friedmann and W.H. Kendall *Ann. Rev. Nucl. and Part. Sci.*, (22):227, 1972.

[7] R.E Taylor In *Proceedings of the International Symposium on Lepton and Photon Interactions at High Energies*, page 679, 1975.

[8] G. Altarelli and G. Parisi *Nucl. Phys.*, (B 126):298, 1977.

[9] A. D. Martin et al. *Phys. Lett.*, (B 306):145, 1993.

[10] ZEUS Collaboration, M. Derrick et al. *Z. Phys.*, (C 65):379, 1995.

[11] A. Baldit et al. *Phys. Lett.*, (B 332):244, 1994.

[12] F. Abe et al. In *Proceedings of the International Workshop on Deep Inelastic Scattering, Eilat, Israel*, 1994.

[13] A.D. Martin et al. *Phys. Rev.*, (D 50):6734, 1994.

[14] E. Witten *Nucl. Phys.*, (B 120):189, 1977.

[15] C. F. von Weizsacker *Z. Phys.*, (88):612, 1934.

[16] J. J. Sakurai *Ann. Phys.*, (11):1, 1960.

[17] M. Gluck et al. *Phys. Rev.*, (D 46):1973, 1992.

[18] P Aurenche et al. *Z. Phys.*, (C 64):621, 1994.

[19] H. Abramowicz et al. *Phys. Lett.*, (B 269):458, 1991.

[20] ZEUS Collaboration, M. Derrick et al. *Phys. Lett.*, (B 293):404, 1992.

[21] ZEUS Collaboration, M. Derrick et al. *Phys. Lett.*, (B 342):417, 1995.

[22] L.E. Gordon and J.K. Storrow *Z. Phys.*, (C 56):307, 1992.

[23] UA1 Collaboration, G. Arnison et al. *Phys. Lett.*, (B 132):223, 1983.

[24] UA1 Collaboration, G. Arnison et al. *Nucl. Phys.*, (B 276):253, 1986.

[25] CDF Collaboration, F.Abe et al. *Phys. Rev. Lett.*, (65):968, 1990.

[26] DELPHI Collaboration, P. Abreu et al. *Z. Phys.*, (C 70):179, 1996.

[27] ALEPH Collaboration, D. Buskulic et al. *Phys. Lett.*, (B 384):353, 1996.

[28] OPAL Collaboration, P.D. Acton et al. *Z. Phys.*, (C 58):387, 1993.

[29] DELPHI Collaboration, P. Abreu et al. *CERN Preprint*, CERN-PPE/96-193.

[30] TPC Collaboration, H. Aihara et al. *Phys. Rev. Lett.*, (61):1263, 1988.

[31] ALEPH Collaboration, D. Buskulic et al. *Z. Phys.*, (C 66):355, 1995.

[32] G. D. Cowan In *Proceedings of the XXVII International Conference on High Energy Physics, Glasgow, Scotland, UK*, editors P. Bussey and I. Knowles, page 883, 1994.

[33] MARKII Collaboration, H. Schellman et al. *Phys. Rev.*, (D 31), 1985.

[34] ALEPH Collaboration, D. Buskulic et al. *Z. Phys.*, (C 64):361, 1994.

[35] B.A. Kniehl J. Binnewies and G. Kramer *Z. Phys.*, (C 65):471, 1995.

[36] T. Sjostrand and M. Bengtsson *Comp. Phys. Comm.*, (43):367, 1987.

[37] T. Sjostrand *Comp. Phys. Comm.*, (82):74, 1994.

[38] H.-U. Bengtsson and T. Sjostrand *Comp. Phys. Comm.*, (46):43, 1987.

[39] H1 Collaboration, T. Ahmed et al. *Phys. Lett.*, (B 299):374, 1993.

[40] Yu. L. Dokshitzer et al. *Basics of Perturbative QCD.* Editions Frontieres, 1991.

[41] ZEUS Collaboration, M. Derrick et al. *Z. Phys.*, (C 67):93, 1995 (and references therein).

[42] OPAL Collaboration, G. Alexander et al. *Z. Phys.*, (C 72):1, 1996.

[43] OPAL Collaboration, G. Alexander et al. *CERN Preprint*, CERN-PPE/97-015.

[44] G. Gustaffson B. Andersson and C. Peterson *Z. Phys.*, (C 1):105, 1979.

[45] OPAL Collaboration, R. Akers et al. *Z. Phys.*, (C 67):389, 1995.

[46] ZEUS Collaboration *The ZEUS Detector Status Report 1993*, February 1993.

[47] E. Paul Talk given at the ZEUS collaboration meeting, November 1995.

[48] K. Piotrzkowski and M. Zachara Determination of the ZEUS luminosity in 1994. ZEUS Internal Note 95-138.

[49] H.Bethe and W.Heitler *Proc. Roy. Soc.*, (A 146):83, 1934.

[50] Application Software Group GEANT - detector description and simulation tool. Long Writeup W5013, CERN, June 1993.

[51] G. F. Hartner et al. VCTRAK (3.06/11): Offline output information. ZEUS Internal Note 95-003.

[52] P. Billoir and S. Qian *Nucl. Inst. and Meth.*, (B 311):139, 1992.

[53] K. Kleinknecht *Detectors for Particle Radiation.* C.U.P., 1986.

[54] K. Long Private communication.

[55] K. Long et al. Calibration of the CTD using the Autumn 1992 data. ZEUS Internal Note 92-122.

[56] J. Lane Private communication.

[57] S. Mengel et al. The magnetic field in the ZEUS central tracking region. ZEUS Internal Note 92-098.

[58] J. Bromley Second Year Report.

[59] P. Bussey EUCELL. PHANTOM Library.

[60] J.Huth et al. In *Proc. of the 1990 DRPF Summer Study on High Energy Physics*, editor, E.L.Berger, page 132, 1992.

[61] J.Terron ZEUS Internal Note 92-118.

[62] C.Glasman, K.Desch and J.Terron ZEUS Internal Note 94-086.

[63] L. Feld, J. Butterworth, R. Field and L. Sinclair ZEUS Internal Note 95-010.

[64] T. Doeker et al. ZEUS Internal Note 92-123.

[65] ZEUS Collaboration, M. Derrick et al. *Phys. Lett.*, (B 315):481, 1993.

[66] ZEUS Collaboration, M. Derrick et al. *Phys. Lett.*, (B 356):129, 1995.

[67] S. George et al. Study of neutral strange particle production in deep inelastic scattering. ZEUS Internal Note 94-155.

[68] Review of particle properties *Phys. Rev.*, (D 54):412, 1996.

[69] TASSO Collaboration, W. Braunschweig et al. *Z. Phys.*, (C 44):1, 1989.

[70] H. Abramowicz et al. ZEUS Internal Note 93-078.

[71] R. Sinkus et al. ZEUS Internal Note 93-117.

[72] ZEUS Collaboration, M. Derrick et al. *Phys. Lett.*, (B 348):665, 1995.

[73] ZEUS Collaboration, M. Derrick et al. *Z. Phys.*, (C 68):29, 1995.

[74] H1 Collaboration, S. Aid et al. DESY preprint 96-122.

[75] K. Johanssen Talk given at DIS96, Rome, April 1996.

[76] H1 Collaboration, C. Adloff et al. *DESY preprint 97-095*, 1997.

[77] J. P. Fernandez Neutral kaons and charged particles in photoproduced jets. ZEUS Internal Note in preparation.